Title

Invention and Development of Liquefied Gas Electrolytes for Lithium Ion Batteries and Beyond

Permalink

https://escholarship.org/uc/item/3m08d1dr

Author

Yang, Yangyuchen

Publication Date

2020

Peer reviewed|Thesis/dissertation

UNIVERSITY OF CALIFORNIA SAN DIEGO

Invention and Development of Liquefied Gas Electrolytes for Lithium Ion
Batteries and Beyond

A dissertation submitted in partial satisfaction of the

requirements for the degree Doctor of Philosophy

in

Materials Science and Engineering

by

Yangyuchen Yang

Committee in charge:
    Professor Ying Shirley Meng, Chair
    Professor Zheng Chen
    Professor Ping Liu
    Professor Jian Luo
    Professor Yu Qiao

2020

The Dissertation of Yangyuchen Yang is approved, and it is acceptable in quality and form for publication on microfilm and electronically:

_____

_____

_____

_____

_____

Chair

University of California San Diego

2020

iii

DEDICATION

To my parents: Guiying Yuan and Libo Yang

TABLE OF CONTENTS

LIST OF FIGURES

LIST OF TABLES

in TCP and best sunset of Pacific ocean on surfing board at Scripps pier. You are the one fully changed my life.

I also would like to thank everyone else in the liquefied gas electrolyte subgroup: Dr. Cyrus S. Rustomji, Daniel M. Davies, Yijie Yin, Matthew Mayer, Ekaterina S. Sablina have helped and inspired me in many ways. The possibilities and personalities they showed made LGE subgroup an enjoyable place to dedicate with. It is honored to collaborate with many talented minds. I also would like to acknowledge and thank my collaborators and co-authors at UC San Diego: Dr. Minghao Zhang, Dr. Chengcheng Fang, Dr. Xuefeng Wang, Dr. Judith Alvarado, Dr. Shen Wang, Dr. Jean-Marie Doux, Dr. Abhik Banerjee, Dr. Marco Olguin, Dr. Han Nguyen, Darren H.S. Tan, Diyi Cheng, Yihui Zhang. All the members in the Laboratory for Energy Storage and Conversion group (past and present) have motivated, inspired me on both research and personal life. Additionally, to my external collaborators and co-authors, I would like to express my gratitude to Dr. Oleg Borodin from U.S. Army Research Laboratory for expanding the understanding boundary of the liquefied gas electrolytes through simulation. I would like to thank Dr. Jungwoo Z. Lee from South 8 Technologies for all the guidance and discussion on cryo-FIB, XPS, and research directions. I truly appreciate all of their dedication and help.

Chapter 4, in full, is a reprint of the material "Liquefied gas electrolytes for electrochemical energy storage devices" as it appears in Science, Rustomji, C. S.; Yang, Y.; Kim, T. K.; Mac, J.; Kim, Y. J.; Caldwell, E.; Chung, H.; Meng, Y. S., 2017, 356(6345). The dissertation author was the co-primary investigator and second author of this paper. The author involved in all the tests and performed all the batteries tests and XPS characterization.

Chapter 5, in full, is a reprint of the material "High-Efficiency Lithium-Metal Anode Enabled by Liquefied Gas Electrolytes" as it appears in Joule, Yang, Y.; Davies, M. D.; Yin, Y.; Borodin, Oleg.; Lee, J. Z.; Fang, C.; Olguin, M.; Zhang, Y.; Sablina, E. S.; Wang, X.; Rustomji, C. S.; Meng, Y. S., 2019, 3(8), 1986. The dissertation author was the primary investigator and first author of the paper. All of the tests were performed and analyzed by the author except for the molecular dynamics simulation.

Chapter 6, in full, is a reprint of the material "Liquefied Gas Electrolytes for Wide-Temperature Lithium Metal Batteries" as it appears in *Energy & Environmental Science*, Yang, Y.; Yin, Y.; Davies, M. D.; Zhang, M.; Mayer, M.; Zhang, Y.; Sablina, E. S.; Wang, S.; Lee, J. Z.; Borodin, Oleg.; Rustomji, C. S.; Meng, Y. S., 2020, DOI: 10.1039/D0EE01446J. The dissertation author was the primary investigator and first author of the paper. All of the experiments parts and characterizations were performed and analyzed by the author except for the molecular dynamics simulation and cryo-TEM.

Chapter 7, in full, is currently being prepared for submission for publication "Fire-extinguishing recyclable liquefied gas electrolytes for lithium metal batteries", Yin, Y.; Yang, Y.; Mayer, M.; Chen, Z.; Meng, Y. S. The dissertation author was the co-primary investigator and co-

first author of the paper. The author formulated the electrolyte with Yin, Y., conceived the recycling process with Mayer and involved in all the experiment and characterization.

VITA

2015   Bachelor of Engineering, Peking University

2016   Master of Science in Materials Science and Engineering

     University of California San Diego

2020   Doctor of Philosophy in Materials Science and Engineering

     University of California San Diego

PUBLICATIONS

(* authors contributed equally to the work)

1. Rustomji, C.S., **Yang, Y.**, Kim, T.K., Mac, J., Kim, Y.J., Caldwell, E., Chung, H. and Meng, Y.S., Liquefied Gas Electrolytes for Electrochemical Energy Storage Devices. *Science*, 2017, 356(6345), 4263

2. Shobukawa, H., Alvarado, J., **Yang, Y.** and Meng, Y.S., Electrochemical Performance and Interfacial Investigation on Si Composite Anode for Lithium Ion Batteries in Full Cell. *Journal of Power Sources*, 2017, 359, 173

3. **Yang, Y.**, Davies, D.M., Yin, Y., Borodin, O., Lee, J.Z., Fang, C., Olguin, M., Zhang, Y., Sablina, E.S., Wang, X., Rustomji, C.S., and Meng, Y.S., High-efficiency lithium-metal anode enabled by liquefied gas electrolytes. *Joule*, 2019, 3(8), 1986

4. Fang, C., Li, J., Zhang, M., Zhang, Y., Yang, F., Lee, J.Z., Lee, M.H., Alvarado, J., Schroeder, M.A., **Yang, Y.**, Lu, B., Williams, N., Ceja, M., Yang, L., Cai M., Gu J., Xu, K., Wang, X., and Meng, Y.S., Quantifying Inactive Lithium in Lithium Metal Batteries. *Nature*, 2019, 572(7770), 511

5. Doux, J.M., **Yang, Y.**, Tan, D.H., Nguyen, H., Wu, E.A., Wang, X., Banerjee, A. and Meng, Y.S., Pressure Effects on Sulfide Electrolytes for All Solid-state Batteries. *Journal of Materials Chemistry A*, 2020, 8(10), 5049

6. Rustomji, C.S., **Yang, Y.**, Davies, D., Lee, J. and Meng, Y.S., South 8 Technologies Inc, Chemical Formulations for Electrochemical Device. 2020, U.S. Patent Application 16/666,131

7. Davies, D., Rustomji, C.S., **Yang, Y.**, Lee, J. and Meng, Y.S., Electrochemical Cell Cap. 2020, U.S. Patent Application 16/666,155

8. Wang, S., Cabreros, A., **Yang, Y.**, Hall., A.S., Fenning, D.P., Meng, Y.S., Hole Transport Layer Spin-Coating-Induced 3D Morphological and Compositional Changes in Perovskite Solar Cells, *Cell Reports Physical Science*, 2020, accepted.

9. **Yang, Y.**, Yin, Y., Davies, D.M., Zhang, M., Zhang, Y., Mayer, M., Sablina, E.S., Lee, J.Z., Rustomji, C.S., Borodin, O., and Meng, Y.S., Liquefied Gas Electrolytes for Wide-temperature Li-Metal Batteries, *Energy & Environmental Science*, 2020, DOI: 10.1039/D0EE01446J.

10. Davies, D.M., **Yang, Y.**, Sablina, E.S., Rustomji, C.S., and Meng, Y.S., Safe, All-Temperature Electrolyte Based on Liquefied Gas Solvent, 2020, in preparation.

11. Yin, Y. *, **Yang, Y. ***, Mayer, M., and Meng, Y.S., Fire-Extinguishing Recyclable Liquefied Gas Electrolytes for Lithium Metal Batteries, 2020, in preparation.

12. Wang, X., **Yang, Y.**, Lai, C., Li, C., Xu, H., Tan, H.S.D., Zhang, K., Fjeldberg, O., Lin, M., Tang, M., Tang, W., Meng, Y.S., and Loh, K.P., Dense stacking porous conjugated polymer as reactive-type host for high performance lithium sulfur batteries, 2020, under review.

ABSTRACT OF THE DISSERTATION

Invention and Development of Liquefied Gas Electrolytes for Lithium Ion
Batteries and Beyond

by

Yangyuchen Yang

Doctor of Philosophy in Materials Science and Engineering

University of California San Diego, 2020

Professor Ying Shirley Meng, Chair

Lithium (Li) ion batteries have been successfully commercialized under decades of development and made a great impact as energy storage devices for electronics industries. The demand keeps increasing and expands to larger areas like grid storage and electric vehicles, which calls for higher energy density, longer cycle life, and wider operation conditions. However, there have been little changes in electrolyte compositions since its commercialization and the balanced-

properties of the conventional electrolytes can't meet the requirements for next-generation electrodes, such as Li-metal anode, high-voltage cathodes.

Herein, we design and develop a novel electrolyte system from a unique direction. The use of molecules that are gases under standard conditions is liquefied under moderate pressure to form liquefied gas electrolyte for the first time. Combing the superior physical and chemical properties, the liquefied gas electrolytes show a wide potential window of stability and impressive performance in extended temperature ranges. Electrolytes using difluoromethane (DFM) and fluoromethane (FM) demonstrate excellent performance in a wide temperature range for electrochemical capacitor and 4-volt lithium-ion battery, respectively.

Comprehensive approaches are applied to have a deeper understanding of liquefied gas electrolytes and further improve the overall performance. Tetrahydrofuran is first introduced as a cosolvent to improve the salt solubility and conductivity. The unique solvation structure and stable solid electrolyte interface enable improved Li-metal coulombic efficiency and rate capability in a wide temperature range down to -60°C. Besides, there are demands to further expand the upper-end boundary of both voltage and temperature window of liquefied gas electrolytes. Therefore, in a separate study, we formulate liquefied gas electrolytes using acetonitrile as a cosolvent and a higher salt concentration of 1.2 M for 4.5 V Li-metal batteries in a wider temperature range (-78~+75°C). Possibilities of using other liquefied gas solvents for Li-ion batteries are also been explored. A mixture of liquefied solvents is selected to improve safety. The electrolyte shows unique properties on fire extinguishing and one step recycling with excellent electrochemical performance.

Chapter 1. Motivation and Outline

As the development of modern society, the increased energy consumption (150 TWh, 2018)[1] for human activities heavily rely on the burning of fossil fuels (coal, oil, natural gas, etc.). It has raised global concerns including environmental pollution, CO_2 emission (33 Gt)[2], and climate change. To change this gear, one way is to capture, storage, and adopt more green and renewable energy into the energy supply, another way is to surge the efficiency of utilizing traditional energy through electrification. Both approaches are calling for energy conversion and storage devices with high energy density, long cycle life, low capital, wide temperature range, and safety.

Since commercialized by Sony in 1990, lithium-ion batteries (LIBs) have had great success in these three decades as a solution for energy conversion and storage. Recently, the 2019 Nobel Prize in Chemistry has awarded to John Goodenough, M. Stanley Whittingham and Akira Yoshino for "the development of lithium-ion batteries" and the significance of this field. The new installed capacity has raised to 294 GWh in 2018, which is more than ten times increase from 2010. Their applications are expanding from portable electronic devices (cell phones, personal computers) to larger-scale devices, like electrical vehicles (EV) and grid storage. Threatened by Tesla's revolutionary EV product of Model 3 using Panasonic's LIBs, all major vehicle companies (Toyota, GM, BMW, etc.) in the world are putting essential efforts on the R&D of electric vehicles. The present LIB platform using a metal oxide cathode coupled with graphite anode achieves good cycle life (in the thousands), high specific energy (~150 Wh·kg^{-1}) and moderate cost (<250 US\$·kg^{-1}) on pack level.[3] However, this intercalation mechanism is fundamentally reaching its upper limit on energy content and cost, which is not expected to reach EV market's long-term

demand on specific energy (500 Wh·kg^{-1}) and cost (<100 US\$·kg^{-1}).[3] Therefore, the research on

the next-generation LIB with novel mechanisms is urgent. Governments and researchers are

investing in different batteries systems that potential to reach higher energy density. The various

proposed directions are derived from the redesign of the three main parts of LIBs: the anode

(negative electrode), the cathode (positive electrode), and the electrolyte between the electrodes.

The combinations of a graphite anode, layer oxide cathode, and carbonate electrolytes in

current LIBs are under rational design with a perfect balance. The carbonate-based electrolytes are

compatible with graphite anode by forming a stable passivation layer known as solid electrolyte

interphase (SEI). The electrolyte also has a relatively large oxidation potential to be stable with 4

V cathodes under the assist of the cathode electrolyte interphase (CEI). The ionically conductive

and electronically insulating nature of SEI/CEI enables a long cycle life of LIBs. Therefore, when

researchers moving forward to next-generation batteries, the change of each composition may

influence the balance and whole combination selection.

On the anode side, the relatively low theoretical capacity of graphite (372 mAh·g^{-1}) has

motivated researchers to explore alternatives with a higher capacity to increase energy density.

Lithium (Li) metal anode is a promising candidate due to its high theoretical capacity (3860

mAh·g^{-1}) and the lowest electrochemical potential (-3.04 V vs. SHE). However, the conventional

carbonate electrolytes are not able to form a stable SEI with this new anode. Problems such as

low coulombic efficiency (CE), dendrite formation, and large volume change might be addressed

by stable SEI construction and new electrolytes design.[4] A similar logic is also applied to the

cathode side. This field is moving towards higher operating voltage and low Cobalt ratio for the

consideration of the energy density and cost. The developed high-voltage Ni-rich Li-Ni-Mn-Co

oxides (NMC, ~4.5 V), Co-free $LiNi_{0.5}Mn_{1.5}O_4$ (LNMO, ~5 V) spinel, and other high-voltage

cathodes will cause the continuous decomposition of conventional electrolytes. It is critical to developing electrolytes with improved high voltage stability and CEI formation.

Additionally, a new electrolyte design is also imperative from the temperature and safety considerations. The narrow battery operation temperature window (-20°C ~ 50°C) of current LIBs is due to the properties of the carbonate electrolytes, such as a high melting point, chemical instability at high temperatures. Furthermore, the carbonate electrolytes are highly flammable and have caused serious safety concerns such as fires and explosions. Electrolytes have been a key between advanced anodes and cathodes to promote next-generation LIBs. Therefore, my Ph.D. research mainly focuses on the investigation of interphases and the development of new electrolytes to enable high-voltage Li-metal batteries in a wide temperature range with improved safety.

My Ph.D. thesis consists of eight chapters, including this motivation (**Chapter 1**). **Chapter 2** provides a general introduction to all components of LIBs. **Chapter 3** briefly introduces the advanced characterization tools that I applied in my research including XPS and cryo-FIB. In **Chapter 4**, we demonstrate the invention of a new electrolyte concept, liquefied gas electrolyte, and its superior performance as energy storage devices. **Chapter 5** improves the solubility limitation of liquefied gas electrolytes by introducing cosolvent and further investigates the mechanism of their excellent Li-metal performance. **Chapter 6** presents the approaches for higher voltage and higher temperature operations to enable a wide-temperature high-voltage Li-metal batteries. In **Chapter 7**, we explore other possibilities in liquefied gas solvents selection and formulate a non-flammable liquefied gas electrolyte with extra safety benefits and practical recycling prcess. **Chapter 8** summarizes the overall work and discuss the ideas for future research.

Chapter 2. Introduction to Lithium Ion Batteries

2.1 Working Mechanism of Lithium-ion Batteries (LIBs)

As an electrochemical energy storage device, a LIB storage the energy by the energy difference of the anode (negative electrode) and the cathode (positive electrode) through the electrolyte. Everything in LIBs is established based on this relative electron energies diagram (Figure 2.1A) summarized by Goodenough.[5]

The anode and cathode have the potential of μ_A and μ_c, respectively. The open-circuit voltage V_{oc} is generated by the potential difference (e $V_{oc} = \mu_A - \mu_c$) and is the driving force during discharge, where electrons leave the anode via the external circuit and enter the cathode after doing useful work. To retain charge neutrality, cations (Li^+ for LIBs) travel from the anode to cathode through electrolyte medium. As a medium, the electrolyte has to be stable with both anode and cathode: the energy separation window of the electrolyte (E_g), defined by the lowest unoccupied molecular orbital (LUMO) and the highest occupied molecular orbital (HOMO), has to be wide enough to include both μ_A and μ_c. The electrolyte will be reduced if an anode with a μ_A above the LUMO and will be oxidized if a cathode with a μ_C below the HOMO unless a passivating solid/electrolyte interface (SEI) is formed on the anode or the cathode to create an energy barrier. Because of the SEI at electrode/electrolyte boundary, a larger V_{oc} could be achieved for larger energy storage.

The charge process is the reversed process of the discharge, as shown in the device diagram[6] (Figure 2.1B). The external energy pushes the electron/Li^+ pairs from low energy end (cathode) to high energy end (anode) and is stored in the LIB during the charging process. In the device diagram, other necessary inactive components are also included: An inert polymer separator

is used for embedding electrolyte and prevent shorting between the anode and the cathode. Current collectors (copper for anodes and aluminum for cathodes) will load the anode and the cathode materials and transfer electrons to or from the external circuit.
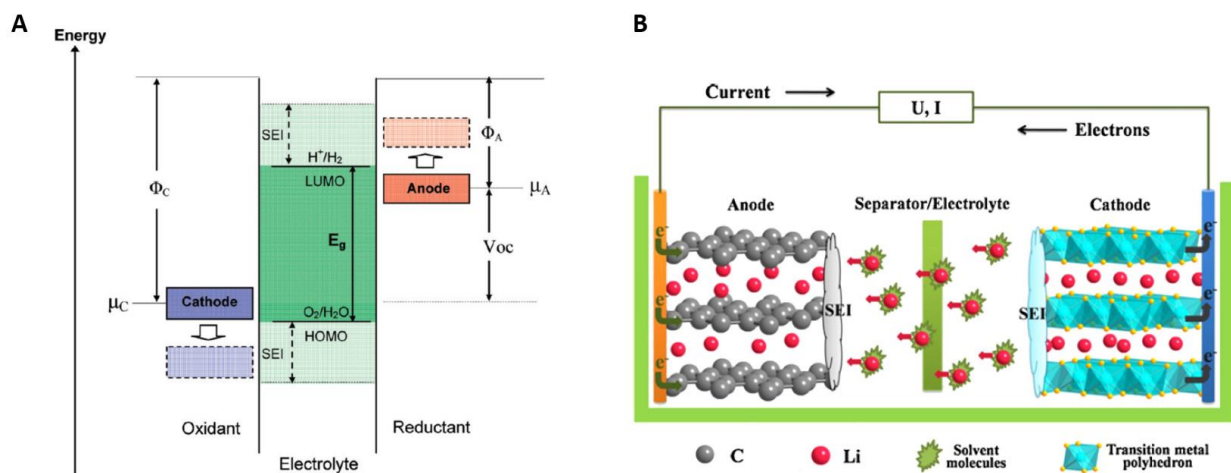
Figure 2.1. Schematic of the working mechanism of a LIB in electron energy diagram[5] (A) and device diagram[6] (B).

2.2 Anode Materials

The development and the selection of different anodes play a critical role in terms of the direction of LIBs. Researchers started with Li-metal anode in the early days but suffered from the problems of safety and low efficiency.[7] The breakthrough of using a graphite anode and ethylene carbonate (EC)-based electrolytes promoted the commercialization of LIBs in 1990 by Sony[8,9] and has been dominating until now. To further improve the energy density, researchers are seeking alternative anodes (Sn, Si/C, Si, Li) with higher capacity (Figure 2.2) and revisiting Li-metal anode, especially.
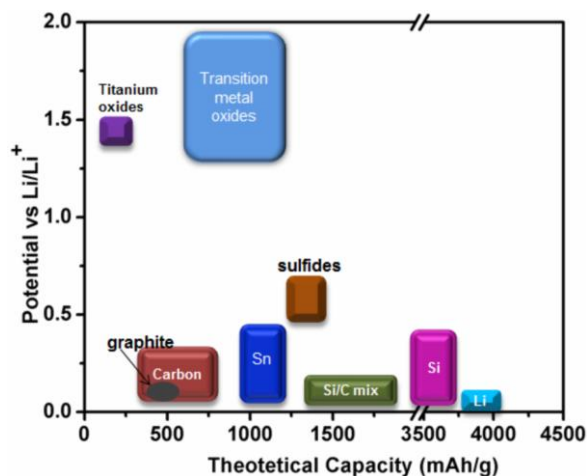
Figure 2.2. Theoretical capacity of different anode materials for LIBs.

2.2.1 Graphite

Graphite anode is overwhelming the market because of its structural stability, safety, low cost, and high conductivity. As a layered intercalation host anode, during the discharge and charge, lithium ions are able to reversibly intercalated and deintercalated through the graphite sheets in the following way: $C_6 + Li^+ + e^- \longleftrightarrow LiC_6$.

The 2D structure supports a fast Li ion diffusion and relatively low volume change (~10%) during cycling yields a volumetric capacity of 756 mAh·cm^{-3} and a gravimetric capacity of 372 mAh·g^{-1}. The abundant carbon sources allow a low cost of this material. As lithium exists in the graphite structure in ionic state, which eliminates the issues of dendrite formation from the metallic state. Also, the high lithium-ion activity of this ionic state enables a potential close to Li metal and maximum the operation voltage. However, this potential is above the LUMO of all the electrolytes and will cause reducing of electrolytes. Only specific categories of electrolytes are able to form a stable passivation layer (SEI) during the first cycle, which is firstly demonstrated and analyzed by Sony and Dahn separately at a similar time in 1990.[10] Without a proper protective layer, the desired

Li-ion intercalation competes with the undesired Li+-solvent co-insertion, leading to the graphite exfoliation and cell failures.[10] The formation of this SEI directly contributes to the success of current commercial LIBs and a deep understanding will give guidance to the development of other anodes.

While the detailed mechanism and the mode of this SEI are still under debate due to the difficulties in the characterizations. Recently studies have pointed out that the solvation structure of the electrolytes is an overlooked factor and plays an equally important role over SEI for graphite stability.[11] It is demonstrated that the Li^+-solvent co-intercalation can be avoided by weakening the Li^+-solvent interaction through approaches such as increasing salt concentrations and introducing other anions. It highlights the importance of the solvation structure of the electrolyte and provides guidance for the construction of next-generation anodes with higher theoretical capacity for higher energy density.

2.2.2 Li-metal anode

Lithium metal has long been considered as the ultimate choice as the anode for Li-based battery chemistries because of its highest specific capacity (3860 mAh·g^{-1}) and the lowest electrochemical potential (-3.04 V versus SHE). Combining with advanced cathodes, the new systems such as Li-high voltage cathode, Li-S, and Li-O₂ potentially support a significantly higher energy density (> 500 Wh·kg^{-1}) (Figure 2.3). However, its practical application has been hindered by several unsolved challenges over several decades, including dendrite formation, low coulombic efficiency (CE), and large volume change.[12–16] With the development of other fields in LIB, such as electrolytes, coating, and characterizations, researchers are revisiting this old concept and getting close to overcoming it.[4,16–18]
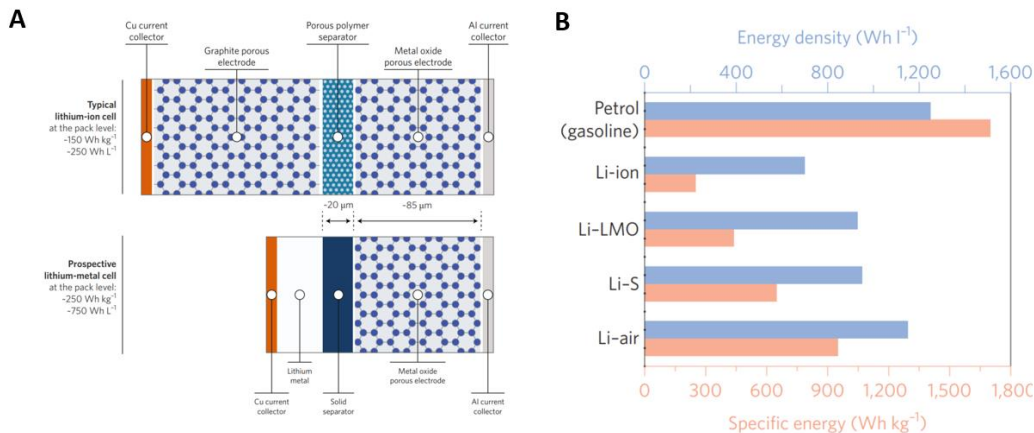
Figure 2.3. Schematic of prospective next-generation Li-metal cell[3] (A); Comparison diagram of energy density and specific energy for different chemistries[4].

As a hostless anode, the working principle is very sample: $Li^+ + e^- \leftrightarrow Li$. During the plating, the Li will deposit on the substrate (Cu, Li, stainless steel, etc.) at the potential of close to 0 V (versus Li). It would be ideal to get a dense film and grows uniformly. However, it turns out to be extremely hard due to the nature of Li metal. 1) Initial nucleation-growth pattern. Instead of directly form a film, the Li ions are firstly nucleated at heterogeneous sites and then grow along the existing Li nuclei sites due to the lower energy barrier, which creates the initial non-uniform factor, fundamentally. 2) SEI formation. SEI forms simultaneously with the nucleation by electrolyte decomposition and causes extra diffusion/growth barriers and uncertainties.[12] 3) Growth behavior. Due to the low surface energy and high migration energy of Li/SEI, the Li deposits are more preferable to grow in a low-dimensional pattern (like 1D dendritic whiskers), called point effect in physical fields, rather than the high-dimensional pattern (2D and 3D). 4) Electrolyte issues. A concentration gradient in electrolytes formed under the electric field will cause the lack of lithium-ion source at the Li surface, which will increase the energy barrier and promote the non-uniform deposition. 5) Stripping and cycling. During the stripping of the low-

dimensional whisker-like Li, a lot of unreacted metallic Li will be isolated by the SEI from the electronic conductive pathway and form inactive Li (also called "dead Li"). It has been proven to be the major source of Li capacity loss over break/formation of the SEI during cycling, which will decrease the CE and cause thicker inactive layer as a diffusion barrier. Combining the fundamental features in these steps, Li-metal anode has issues with dendrite formation, low CE, and large volume change, which would cause safety threats (like fire and explore) and performance limitation (like quick fading). Although some of the summarized processes and models are still under debate, it is clear that the efforts on fundamental understandings are critical and indispensable for the development of different strategies to solve the problems.

According to the summarized dendrite growth mechanism, there have been various approaches to improve the performance. As they have been reviewed extensively,[16,19–21] the author only summarizes the major directions and highlights the progresses. As shown in the diagram (Figure 2.4), it is straight forward to mainly work on the three aspects: the electrolyte, the interface, and the substrate.
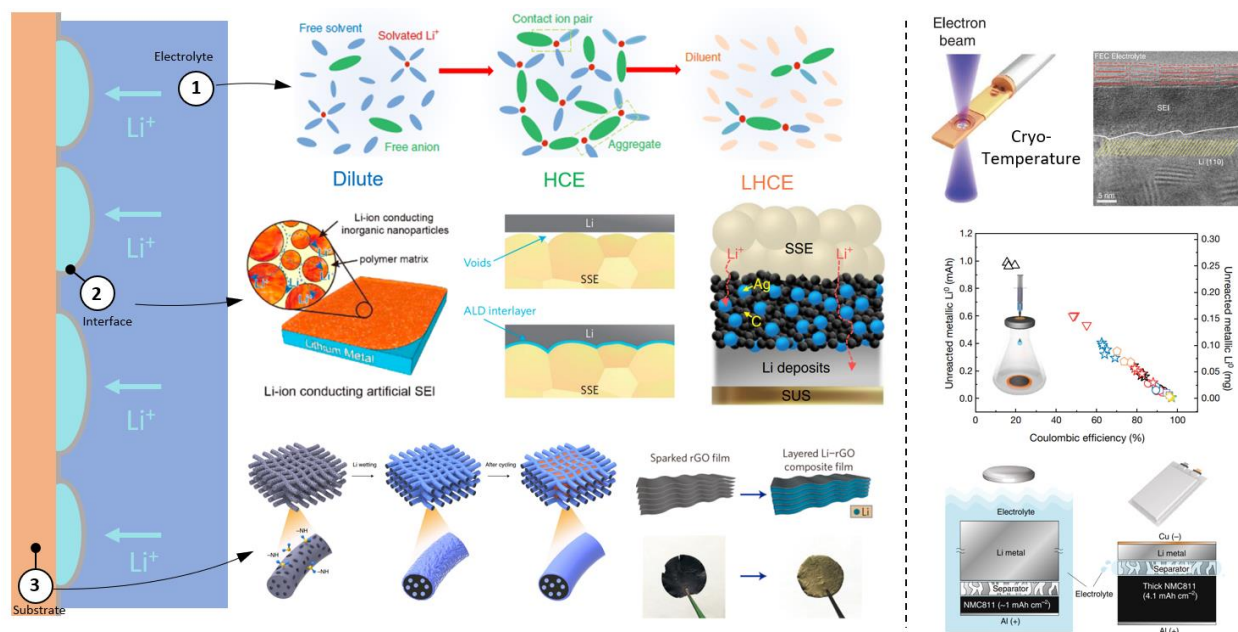
Figure 2.4. Strategies for overcoming Li-metal challenges (Redraw from publications[17,22–29])

1) Electrolyte influence the Li deposition on nucleation, SEI formation, and Li-ion diffusion. To form a proper SEI and achieve high Li+ transference number, efforts are made on salts[30], solvents[31], additives[32,33], and its ratios[26]. As a major breakthrough, high concentration electrolytes (HCE) enable favorable inorganic-rich SEI by salt-dominated decomposition and high Li^+ transference number (>0.7) by structural diffusion mechanism.[34,35] They are further upgraded to localized high concentration electrolytes (LHCE) recently.[36,37] Positive impacts on the performance from the fluorinating interphases promotes the development of the fluorinated electrolytes. Solid-state electrolytes (SSE) show advantages of safety and good SEI stability after formation. These will be further introduced in the later sections. Liquefied gas electrolytes developed in our lab have also shown superior properties for Li-metal anode.[38,39]

2) Interface engineering. Instead of forming SEI by electrolyte decomposition, the artificial SEIs are proposed and achieved by polymer coatings[29], atomic layer deposition (ALD)[24], etc. There are also coating apply on the separator or directly modifying the separators. Besides, an extra electron-conducting layer[25] (like Ag-C) is realized to effectively regulate Li deposition in SSE, providing insights on the interface design.

3) Various 3D substrates are proposed[23], replacing regular 2D Cu, as a host to mitigate the large volume change and reduce local current densities, although the cost and large-scale production are the challenges.

Besides, the effects of different external factors, including stack pressure[27,40,41], temperature[42,43], on Li-metal anode are investigated. The gap between material properties and large-format cell-level performance has been narrowed by the standardization of some key parameters, such as E/C, N/P ratios.[17,44] Some advanced characterization tools are applied to Li-metal field recently. Adopted cryo-technique from biological fields, the detailed features of SEI and bulk Li-metal structure are uncovered by cryo-TEM[22,45,46] and cryo-FIB[38,47], respectively. A titration gas chromatography (TGC) method is developed to quantify inactive Li in Li-metal batteries.[28]

2.3 Cathode Materials

The design of a cathode involves tailoring of the μ_c of a cathode to the HOMO of the electrolyte. Generally, the ideal cathode materials for LIBs should have the following features: 1) high standard electrode potential for a high open-circuit voltage; 2) large reversible capacity; 3) high chemical/electrochemical stability with electrolytes; 4) high electronic conductivity and high

11

Li-ion diffusion; 5) low cost and environmental friendly. To date, all practical cathodes have host structures where guest Li-ion can be inserted and extracted reversibly.

In the past five decades, several generations of cathode materials have been developed with steadily improved energy density (Figure 2.5). In the 1970s, Whittingham firstly demonstrated fast, reversible Li intercalation into layer TiS_2 to form Li_xTiS_2 ($0 < x < 1$) as a cathode for a lithium rechargeable battery, although the voltage (vs Li) was only about 2.2 V and the further application was failed due to Li-metal issues.[48] In 1980, Goodenough and Mizushima developed a layered transition-metal oxide (LMO_2) of $LiCoO_2$ as the cathode material with good structural stability and 4 V open-circuit voltage.[49] This material and its derivatives were then successfully used in commercial LIBs in 1991. However, the Co is too expensive and toxic for large-scale applications and only half of the lithium could be reversibly extracted from $LiCoO_2$ without a major phase transition.[50–52] Many alternatives of cathodes were then explored, including LiM_2O_4 ($LiMn_2O_4$), $LiMPO_4$ ($LiFePO_4$), and, $LiMO_2$ ($LiMnO_2$, $LiNiO_2$, $LiNi_{0.8}Co_{0.15}Al_{0.05}O_2$, $LiMn_{0.5}Ni_{0.5}O_2$, $LiMn_{1/3}Co_{1/3}Ni_{1/3}O_2$, etc.). The $LiMn_{1/3}Co_{1/3}Ni_{1/3}O_2$ synthesized in 2001 is a major breakthrough, delivering 20% more energy density over $LiCoO_2$ with much less Co used.[53,54] The key concept it that Ni^{2+} is stable with the presence of Mn^{4+} or other elements (like Al for $LiNi_{0.8}Co_{0.15}Al_{0.05}O_2$). This emphasizes the recent trend toward multicomponent transition metal layered oxides with higher Ni ratio and operating higher voltage.
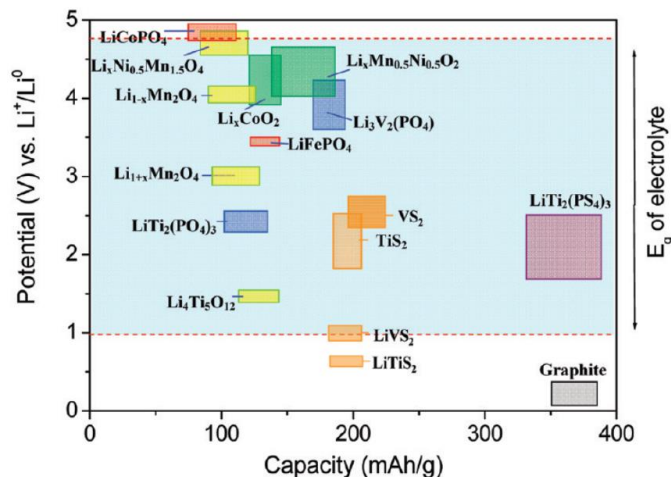
Figure 2.5. Voltage versus capacity of several electrode materials relative to the window of the carbonate electrolyte[5].

2.4 Electrolyte

Over the half century, the research in batteries field has been focused on design and development of the chemistry and the structure of different electrode materials and the main composition of the electrolyte has little change since its commercialization. However, the electrolyte, which conducts ions but insulates the electrons, has been realized as an overlooked key component for supporting new chemistries and materials. For different batteries system, there are similar general guidelines for the electrolyte: 1) wide electrochemical potential window; 2) good interface; (SEI) formation with required electrodes; 3) high ionic conductivity and low electronic conductivity; 4) high Li^+ transference number; 5) safe material, low toxic, and low cost.

Commercialized carbonate electrolytes maintain a moderate balance of these requirements but new electrolyte systems and concepts are urgent for further improve the performance. Therefore, the fundamental theories and new concepts in electrolyte are introduced in this section.

2.4.1 History of Commercialized Electrolytes

As most active electrode materials used today are in the solid state, in order to have a better wetting for fast charge transport, it is straight forward to use liquid state materials as the transport medium, termed as electrolyte. Lithium electrolytes are formed by dissolving one or more lithium salts in one or more solvents, according to the individual properties.

Although aqueous solvents with active protons have excellent power in solvating salts, they are been ruled out as a candidate as their voltage window (E_g ~1.3 V) too narrow for most applications (from ~0 V to ~4.5 V). To pursue a higher V_{oc}, it is inevitable to use nonaqueous solvents. The nonaqueous compounds, to be able to dissolve sufficient amounts of lithium salt, should have certain polar groups such as carbonyl (C=O), ether-linkage (-O-), nitrile (C≡N), sulfonyl (S=O), and phosphate (check this word, P=O). Therefore, several categories of liquid electrolytes are developed based on various functional groups in the solvent. Overall, a suitable solvent should have the features of high dielectric constant (ε_r), low viscosity, high chemical/electrochemical stability, wide liquid temperature range, and non-toxic. With a better balance of dielectric constant and viscosity (η), a lot of electrolytes are in a mixture of cyclic compound (high ε_r, low η) and linear compound (low ε_r, high η). It is generally accepted that, in the diluent system (~ 1 M lithium salt), ethylene carbonate (EC)-based electrolytes have moderate oxidation stability (~4.3 V vs. Li) and could passivate graphite anode but have issues with Li metal anode and low melting point.[55,56] Ether-based electrolytes have better compatibility with Li-metal anode but low oxidation stability (< 4 V vs. Li) and not stable with 4 V class cathodes.[13,15] Nitrile solvents have high anodic stability beyond 4.5 V but have poor cathodic stability over the anode. Sulfonyl-based solvents' advantage in oxidation stability is impaired by their high viscosity and high melting point. Most of phosphate-based electrolytes are fire-retardant but inferior in other

properties. The approaches to designing electrolytes that maximum the advantages of the solvents and overcome the limitations is the key in the electrolyte research.

The selection of solute (lithium salt) is equally important as solvents for electrolytes. The solute should meet the minimal requirements: 1) completed (at least partially) dissolve and dissociate in the nonaqueous media; 2) both cation and anion remain stable to all the cell components. It turns out that the available choice of lithium salt is much less compared to the possibilities in solvents. Most of lithium salts (such as halides, LiX; oxides like Li_2O) are ruled out due to requirement 1) and the small ionic radius of lithium-ion. To meet the minimum solubility, a simple anion core is complexed by a moderate Lewis acid agent, in which the formal negative charge is well distributed by a strongly electron-withdrawing group. For instance: $LiPF_6 = Li^+ + F^- + PF_5$. According to this guidance, lithium salts of $LiPF_6$, $LiBF_4$, $LiAsF_6$, $LiClO_4$, Li imide ($LiC_2F_6NO_4S_2$ (LiTFSI), $LiF_2NO_4S_2$ (LiFSI)) are developed. The features of each salt are summarized in Table 2.1. The current winner of $LiPF_6$ is based on its well-balanced properties, although it is not the best one in any single property.[7] $LiClO_4$ and $LiAsF_6$ are eliminated due to the fatal flaws in safety and toxicity, respectively. Researchers are revisiting $LiBF_4$ due to its balanced feature and surprisingly good performance at low temperatures. Li imide (LiFSI, LiTFSI) is the current research focus essentially because their high dissociation constant shows superior advantages on the formation of electrode interphases.[57,58] Progress is also achieved on Al corrosion and cost control of Li imide.[59,60]

Table 2.1. Properties of various lithium salts.

	Ionic conductivity	Solubility/ Dissociation	Thermal Stability	SEI	Al passivation	Safety	Toxicity
LiClO$_4$	√	√	√	√	√	✗	√
LiAsF$_6$	√	√	√/✗	√	√	√	✗
LiPF$_6$	√	√	√/✗	√	√	√/✗	√
LiBF$_4$	√/✗	√/✗	√	√	√	√	√
Li Imide	√/✗	√	√	√	✗	√	√

Based on the summarized properties of nonaqueous solvent and lithium salt, the efforts to develop new electrolytes are those to enable better-balanced electrolytes properties towards individual electrodes by rational design.

2.4.2 New Concepts in Electrolytes

Carbonate solvents are flammable and volatile and LiPF$_6$ is chemically unstable to moisture and temperature changes, which causes safety concerns and limits the further upgrades of the LIBs. Several new concepts are developed showing potential for commercialization.

1). High Concentration Electrolyte (HCE).

For a long period, the optimized salt concentration is around 1 M with the consideration of maxing the lithium-ion conductivity. In recent years, researchers have realized that simply increasing the salt concentration will enhance the ion-solvent interaction and decrease the amount of free-solvent molecules.[34,35,61]

The new solvation structure makes both the lowest LUMO and highest HOMO shift from the solvent towards the salt, leading to salt-dominated reduction on SEI formation and oxidation on CEI formation.[61,62] Combining with interphase formation advantages in Li imide, the

improvement on both reduction and oxidation stability enables a larger electrochemical potential window and creates a lot of possibilities in different electrolyte systems. For instance, ether-based HCEs (like 4 M LiFSI /DME[63]; 4.6 M LiFSI-2.3 M LiTFSI/DME[64]) show increased anodic stability up to 4.4 V to be compatible with high-voltage cathodes. Carbonate-based, nitrile-based, and sulfonyl-based HCEs demonstrate improved compatibility with Li-metal anode and graphite. The potential window of aqueous electrolytes is also extended to >3 V from 1.3 V.[35,65] The corrosion of Al from LiTFSI/LiFSI could also be mitigated at high concentrations.[59,60]

The new solvation structure also transfers the diffusion mechanism from the vehicular model to the structural model.[66–69] The most of cations remain in the solvating state, which means most of the ion transport is contributed by lithium-ion. The high Li^+ transference number will relieve the concentration gradient in electrolytes and mitigate the dendrites formation in Li-metal anode.

With the formation of a new solvation structure, the changes in the decomposition mechanism and diffusion mechanism lead to the unique properties of HCE. However, the large amount of salt result in the issues of high viscosity and high cost. The high viscosity (~100 times to dilute electrolytes) makes the wetting process challenging, especially for high loading electrodes. The high cost from salt (LiTFSI > $LiPF_6$ >> carbonate solvent \$/g) represents an essential barrier for the commercialization of HCEs.

2). Localized High Concentration Electrolytes (LHCE).

To overcome the problems seen in HCEs, an inter non-solvating solvent is introduced to HCE as a dilute. This chemically stable dilute enable lower viscosity and cost, without changing

the local coordination environment.[36,70–72] The lower viscosity will also improve the wetting, conductivity, and low-temperature performance.

Different kinds of hydrofluoroethers were selected due to the appropriate low permittivity and chemical stability. Bis(2,2,2- trifluoroethyl) ether (BTFE), as a flammable dilute with lower viscosity, was introduced to the nonflammable phosphate-based electrolyte to form a fire-retardant electrolyte[73] and also used as dilute in other ether[72], carbonate electrolytes[37]. 1,1,2,2-Tetrafluoroethyl-2,2,3,3-tetrafluoropropyl ether (HFE or TTE), as fire-retardant dilutes with higher viscosity, were also widely used in TMS[71], FEC/FEMC[70,74,75], etc. A proper permittivity and coordination properties of the dilutes and the optimized ratio of the combinations are important to form a good mixture without phase separation.[71,76] The hydrofluoroethers have many derivatives[77], providing space for further tailoring the properties on flammability, volatility, viscosity, etc. Therefore, this dilution approach could conquer the issues in HCE while maintaining the advantages, providing a promising pathway for future commercialization.
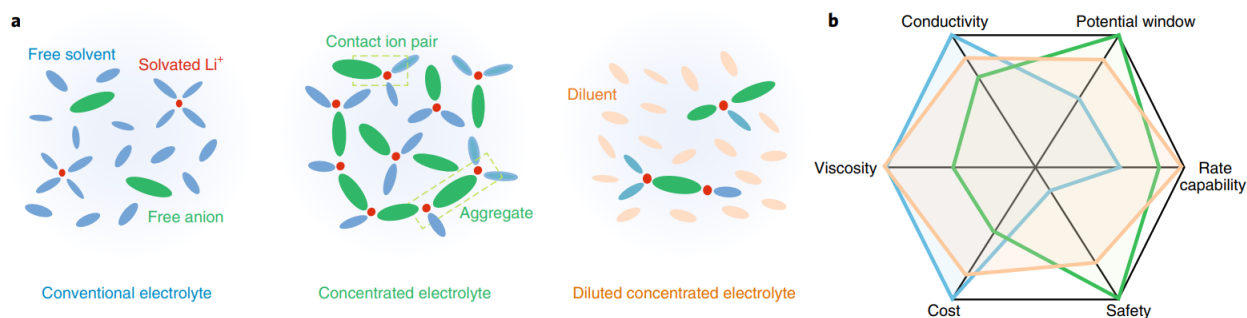
Figure 2.6. Schematics of solution structures of the three electrolytes (dilute, HCE, LHCE) and their properties comparison[26].

3). Highly Fluorinated Electrolyte & Low Solvating Power Electrolyte.

Synchronously with the development of HCE and LHCE, researchers found that the presence of fluorine in the interphases, inorganic fluorides or organofluoro-moieties, provided positive impacts on the electrochemical performance.[78] Although the compound distribution and functional mechanism are still under debate, there is a clear trend to fluorinate the electrolyte for the improved interphase stability. For instance, the use of fluorinated non-polar diluents (HFE) in concentrated fluorinated electrolytes (FEC/FEMC), shifting from EC/EMC, forms an all-fluorinated LHCE, demonstrating stable interfaces with high voltage Li-metal batteries and impressive low-temperature performance down to -85°C.[70] A fluorinated cyclic phosphate-based electrolyte (TFEP) are designed and synthesized and the formulated electrolyte (0.95 m LiFSI in TFEP/FEMC) showed good high voltage stability with extra safety benefits.[79]

For a better salt dissociation, the electrolyte field used to prefer a solvent with high solvating ability and a salt with low dissociation constant.[7] However, a strong Li_+-electrolyte solvating (low solvation energy) would result in high desolvation energy. This extra energy barrier in the desolvation process impacts negatively on interphase formation, high rate kinetics, and low-temperature performance. A quantitative measurement of Li^+-solvent was established and termed as solvating power by Amine et al, indicating the ratio between the coordination percentage of a studied solvent.[31] More and more advanced electrolytes start using low solvating solvent for more balanced properties. For this reason, researchers are switching from EC and EMC to FEC and FEMC, respectively.[70,74]

$$\chi = \frac{\alpha_{ES}}{\alpha_{EMC}}$$

GBL	1.95
HFEEC	1.82
PC	1.46
EC	1.41
EA	1.17
DMC	1.02
EMC	1
TFPC	0.83
FEC	0.63
FEMC	0.44
DFEC	0.10

Figure 2.7. Schematic illustration of the effect of the fluorinated electrolyte[74] (A) and solvating power of series of electrolytes[31] (B).

4). Solid-state Electrolyte

Besides commonly used liquid state electrolyte, solid-state electrolytes (SSEs) are regarded as one potential solution, all-solid-state batteries (ASSB), owning to their non-flammable feature and the simplicity of their interfaces with electrodes. Coupled Li metal anode with high voltage cathode or sulfur, ASSBs can potentially deliver an energy density of > 500 kWh·kg^{-1} at the pack level with improvement on safety.

Despite their mentioned benefits, SSEs still poses several challenges. Although several SSEs have been developed, including oxide-based, sulfide-based, and polymer-based SSE, no single SSE can meet all requirements for commercialization, that is high ionic conductivity, wide electrochemical stability, stable interface formation, ease of processability. Dendrite formation was also detected in SSE, which used to be thought to be impossible in SSEs. The buried and heterogenous interfaces cause extra barriers for characterization and understanding. Air-sensitive with poor mechanical properties of the SSEs will also face issues for scalable ASSB fabrication.[80]

Figure 2.8. Summary of major scientific challenges in the development of solid-state batteries[80].

Alone these issues, the relatively high electronic conductivity of some SSEs (LLZO, Li_3PS_4) was proved to be the root of the dendrite formation.[81] A thin Ag-C electronic-conducting layer was developed to reduce Li-metal nucleation energy for the uniform deposition, enabling a long-cycling anode-free Li-metal batteries.[25] Polymer-composite-based SSEs demonstrated a combination of the benefits of both SSEs systems.[82–85] Other progress in SSEs has also been reviewed extensively[86,87] and will not be covered here.

5). Liquefied Gas Electrolyte

Besides using materials that are liquid or solid at ambient conditions, researchers in Shirley Meng's group design and develop a novel electrolyte, based on liquefied gas.[39] The researchers selected hydrofluorocarbons (like fluoromethane (FM), difluoromethane (DFM)) as the solvent, which is in the gaseous state under room temperature at atmosphere pressure. Under moderate pressure, these low polar solvents will be liquefied at dissolve a certain amount of salt to form the liquefied gas electrolyte. The solvents have the features of low viscosity, low melting point, high

fluorine ratio, and high chemical stability, leading to stable cycling of 4 V Li-metal batteries in a wide temperature window down to -60°C.

Based on the superior physical and chemical properties of the solvents, upgrades were made by introducing different cosolvent, increasing salt concentration, and exploring new liquefied solvents, which leads to improved performance on both Li-metal and high-voltage cathode with wider temperature operation ranges.[38] Liquefied gas electrolytes are highly fluorinated using low solvating solvents with unique solvation structurer, which combines the advantages mentioned in section 3). The series of work will be further introduced in the following chapters (Chapter 4 – Chapter 7) as the author's work.
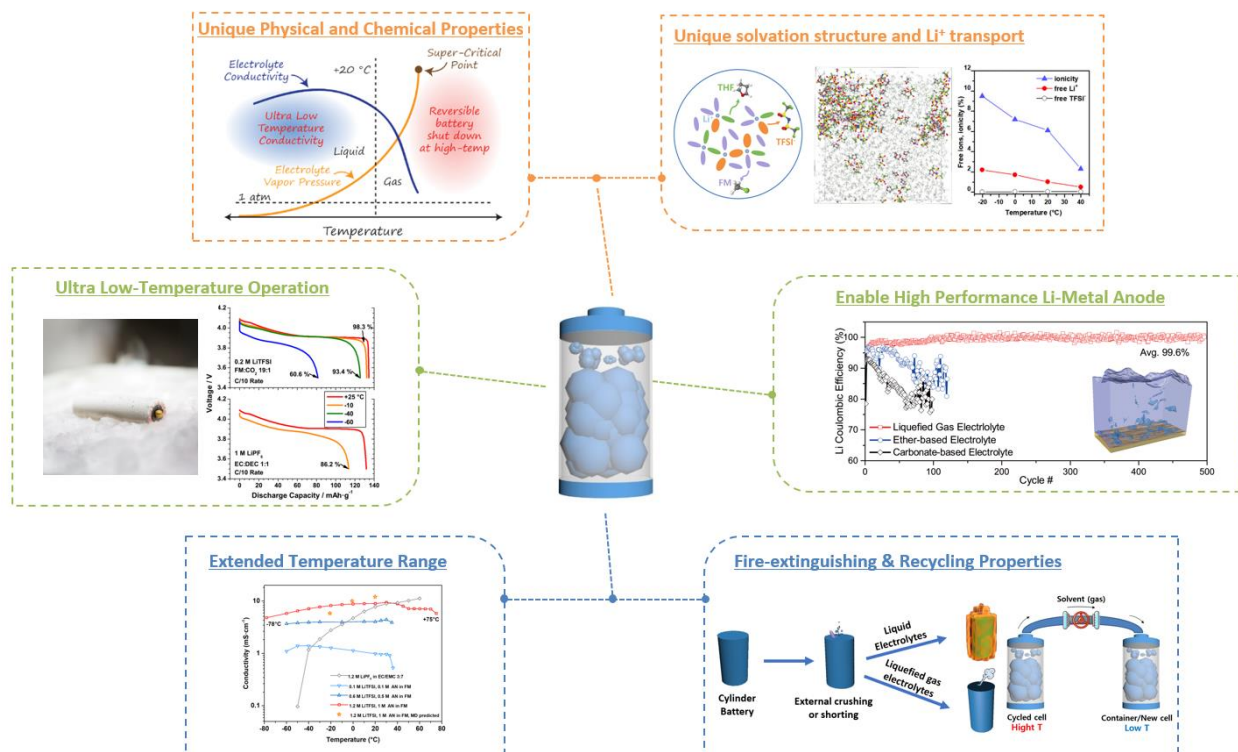
Figure 2.9. Exploration of liquefied gas electrolytes, redraw from publications[38,39,88].

Chapter 3. Advanced Characterization Tools

To understand the properties of the materials in different scales, from bulk to nano, appropriate characterization tools need to be applied (Figure 3.1). In general, most of characterization methods are functional in the same workflow: apply a certain stimulation signal (X-ray, e-beam, spectra, etc.) and then capture the corresponding feedbacks. The feedbacks can be classified to two different modes: 1) Spectroscopy is a measurement of a quantity as a function of energy such as Raman, XPS, AES, EELS, etc.. 2) Imaging and scattering is a map of some contrast mechanism in real space ((FIB)-SEM, TEM) or reciprocal space (XRD, electron diffraction), respectively. During my Ph.D. study, the author mainly applies the spectroscopy tool of XPS and the imaging approach of FIB-SEM to investigate the interface composition and the bulk structure of electrodes and will introduce them as follows.
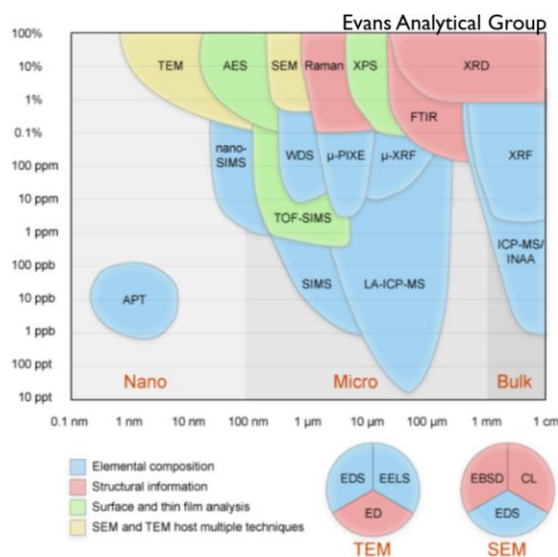
Figure 3.1. Diagram of features of various nanoscale characterization techniques.

3.1 X-ray Photoelectron Spectroscopy (XPS)

XPS is a surface characterization technique, which is able to obtain the elemental composition and chemical environment of the interested materials qualitatively and quantitatively. The working principle is shown in Figure 3.2A. The core-level electrons are firstly excited via photons with specific energy and then ejected into the vacuum as photoelectrons. The kinetic energy (K.E) of the ejected electrons is related to the binding energy (B.E) of the electron and the work function of the instrument as the equation 3.1. The photoelectrons travel along equipotential lines and pass through a hemispherical spectral analyzer without any energy change and arrive electron detector.

The binding energy can be calculated by measuring the kinetic energy and the data is then presented in a spectrum with intensity versus binding energy spectrum (Figure 3.2B). The obtained spectrum contains unique chemical information of the bonding environment of each element in the corresponding region.
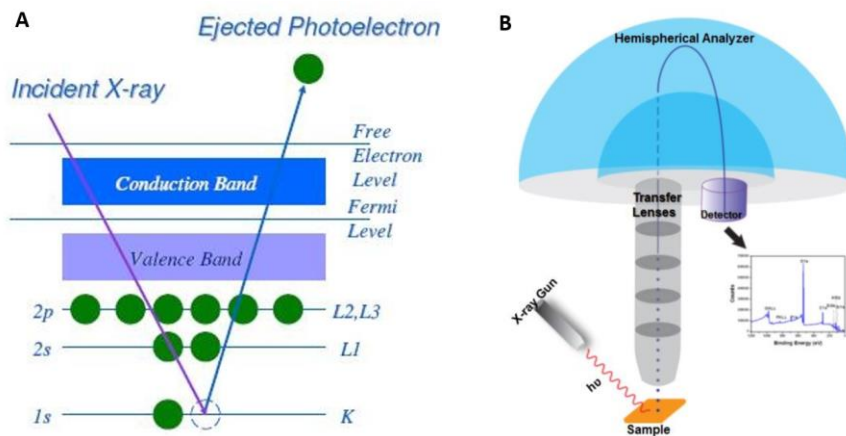
Figure 3.2. A) Schematic illustration of the working principle of XPS. B) Schematic of XPS set up

$$K.E= h\upsilon \text{-} B.E \text{-} \phi_{sp} \qquad\qquad (eq. 3.1.)$$

In order to minimum the photoelectron energy loss and sample contamination, all the processes must be completed in an ultrahigh vacuum (10^{-8}-10^{-10} Torr), realized by a molecular pump. Standard XPS uses X-ray sources of Mg (Kα:1253.6 eV) or Al (Kα:1486.6 eV). The relatively low energy of the X-ray source leads to a narrow detective depth, inelastic mean free path ($<$ 10 nm). At the same time, XPS can get average information at a relatively large detect area such as 300 um $*$ 500 um. As a surface sensitive characterization tool, XPS is reliable on the chemical analysis on the interphases like SEI.

Additionally, the depth-profile experiment can be applied by using an ion beam (Ar$^+$) to etch layers of the sample surface and reaching the subsurface. Combining XPS with steps of ionic etching provides the chemical information as a function of the depth of the surface (Figure 3.3.). It is useful in revealing the composition distribution of the interphase. However, what needs to be noticed is that certain chemistry (such as LiTFSI) could be damaged and decomposed by the milling process. Therefore, the long-time etching under high milling voltage should be avoided.
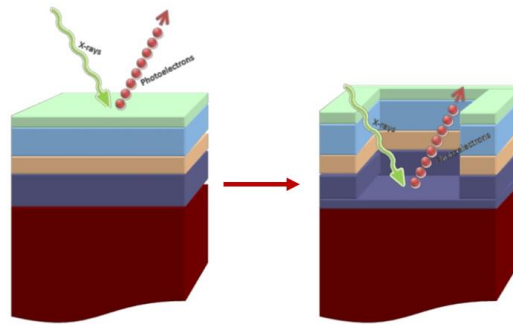
Figure 3.3. Schematic illustration of depth-profile XPS.

The surface sensitivity and ability of depth-profile analysis make XPS an appropriate technique for interphases (SEI, CEI) studies. As the SEI and CEI are extremely sensitive to air and humidity, all of author's samples were transferred to XPS main chamber through an argon filled glovebox.

3.2 Cryo-genic Focused Ion Beam Scanning Electron Microscopic (Cryo-FIB-SEM)

Focused ion beam (FIB) is a mature technique for milling and imaging in the fields like semiconductor industry, material science. FIB system operates in a similar way to the scanning electron microscope (SEM). Instead of playing with a beam of electron, FIB systems utilize a focused beam of ions (mostly gallium). FIB can be operated at low current for imaging, using the same principle with SEM, or at higher beam current for milling on a selected area. In most FIB systems, ion beam and electron beam are coupled in the same chamber in a specific angle (52°) to combine both benefits. The sample will first be milled by FIB and then using SEM to image the cross section for higher resolution and less damage, which makes it an important tool to investigate different bulk structures.

However, the milling processes of FIB also raises concerns about the surface damage and redeposition, especially for some sensitive material, such as Li metal. Because Li has low melting temperature, density, thermal conductivity, and shear modulus, Li metal is extremely sensitive to ion beams and could be damaged easily even at reduced current. Cryo-FIB is developed for the protection of biological samples and transferred to the battery fields (like Li-metal anode) recently. The key components of the cryo-FIB system are shown in Figure 3.4: the samples are in thermal contact with the stage cooled with a chilled nitrogen gas source. There is no direct contact between samples and nitrogen gas and the sample's temperature would stable at around -170°C. Also, the

vacuum is maintained as room-temperature operation ($\sim 10^{-6}$ mbar). Under this cryo-condition, the detailed feature of the studied sample can be preserved while maintaining the milling speed and other functionality of FIB.
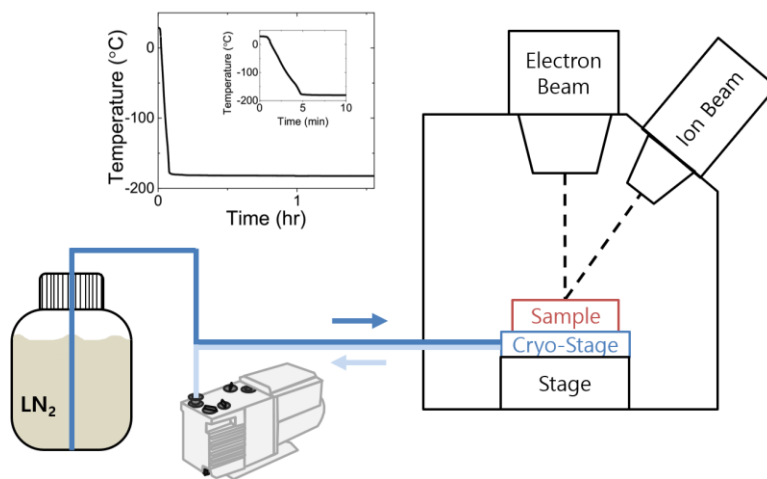
Figure 3.4. Schematic of cryo-FIB configuration and cooling profile[47].

With the help of the cryo-FIB, researchers can have a qualitatively understanding of the studied samples on morphology, packing density, voids distributions. However, these are highly localized observations and the result may be varied at different locations. To enable better quantitative analysis, a 3D-FIB with a reconstruction method is developed (Figure 3.5). Cross-sectional images are sequentially collected while continuously milling through a large selected sample area. These images are then segmented to generate a 3D reconstruction model using Amira-Avizo software. For instance, 50 slices are milling sequentially with a slice distance of 100 nm in the author's Li-metal deposition study. The visualized model with a $10*5*5$ (um^3) dimension can provide accurate statistics on porosity, roughness, surface area, which is critical on the overall evaluation of the material.
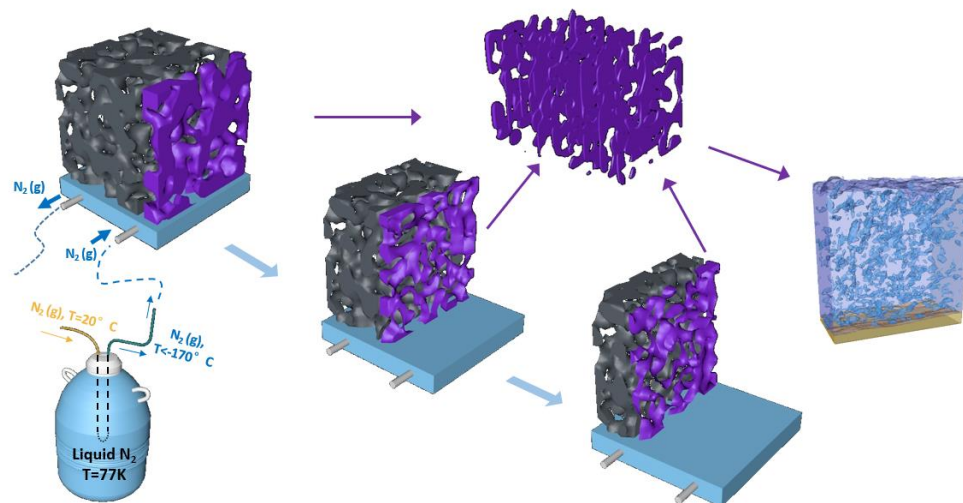
Figure 3.5. Schematic illustration of 3D-FIB and its reconstruction under cryo-condition[38].

Chapter 4. Liquefied Gas Electrolytes for Electrochemical Energy Storage Devices

4.1 Introduction

Electrochemical energy storage devices, such as electrochemical capacitors and batteries, are crucial components in everything from communications to transportation. Aqueous based electrolytes have been used for well over a century, but a substantial increase in the energy density was achieved through the development and use of electrolytes based on organic solvents which allowed for operation at higher voltages. The modern Li-ion battery was only realized with a serendipitous discovery that the use ethylene carbonate, a solid at room temperature, as an electrolyte solvent could stabilize the graphite anode via formation of a suitable solid electrolyte interphase (SEI) and allow for reversible lithiation and delithiation of the electrode.[10] While the majority of electrolyte work remains with liquid solvents and solid electrolyte systems, there has been very little work using electrolyte solvents that are typically gaseous under standard conditions. While not used as an electrolyte, sulfur dioxide (T_b = -10 °C)[89] and sulfuryl chloride fluoride (T_b = +7.1 °C)[90] have been used as catholytes in non-rechargeable primary lithium batteries, however, both use additional co-solvents in the electrolyte which are liquid at room temperature. There have also been a number of studies using ammonia (T_b = -33.3 °C) as a liquid anode due to its ability to solvate alkali metals.[91–93]

It is often assumed that materials which are gaseous at room temperature are typically non-polar and have low intermolecular attraction, which prevents them from condensing at room temperature or even solubilizing salts in a cooled, or pressurized, liquid state. While this may be true in general, there are a number of reasonably polar molecules which show low London

29

dispersion forces due to their small molecular size and are gaseous at room temperature. For instance, the dielectric constant of dichloromethane ($\varepsilon_{DCM,20°C} = 8.9$, $T_b = +40$ °C) is substantially lower than that of structurally similar difluoromethane ($\varepsilon_{DFM,20 °C} = 14.2$, $T_b = -52$ °C), although at room temperature the former is a liquid while the latter is a gas. At low temperatures or with moderate pressures, these types of polar gasses may be liquefied and have been shown to be capable of solubilizing salts to form liquefied gas electrolytes, in which ion transport, redox phenomena and other fundamental studies have been conducted.[94–100]

The use of liquefied gas electrolyte systems exclusively composed of solvents which are gaseous at room temperature and atmospheric pressure in rechargeable energy storage systems is explored. Although a number of potential liquefied gas solvents were evaluated, efforts were focused on hydrofluorocarbons, which have moderate dielectric constants that allows for the solubility of salts to form conductive electrolytes. These electrolytes show ultra low-temperature operation, increased energy density in electrochemical capacitors and high lithium plating and stripping efficiency for potential use of the high capacity lithium metal anode in batteries. It should be cautioned that while the hydrofluorocarbon solvents themselves are generally non-toxic, they do range from non-flammable to highly flammable and combustion products may be toxic to humans. Further, these solvents do exhibit a low to high global warming potential. As such, these materials should be handled properly with additional information provided in supplementary text.

4.2 Materials and Methods

4.2.1 Materials

Fluoromethane (99.99%) and difluoromethane (99.99%) were obtained from Matheson Gas, fluoroethane (97%), 1,1-difluoroethane (99%), 1,1,1,2-tetrafluoroethane (99%) and 2-

fluoropropane (98%) were obtained from Synquest Labs and carbon dioxide (99.9%) was obtained from Airgas. All gases were stored in high pressure refrigerant recovery tanks after use to minimize their release to atmosphere. The salts tetraethylammonium hexafluorophosphate (99.9%) and lithium bis(trifluoromethane)sulfonimide (99.9%) were purchased from BASF while all other salts (electrochemical grade) and acetonitrile (99.8%, anhydrous) were purchased from Sigma-Aldrich. For comparative studies, a liquid electrolyte composed of 1 M $LiPF_6$ in EC:DEC 1:1 by wt% was used (LP40, BASF). Dimethyl carbonate (≥99%, anhydrous) and Nujol Oil for FTIR measurements was purchased from Sigma-Aldrich. Acetonitrile and dimethyl carbonate were dried over molecular sieves prior to use while all other materials were used as received.

For lithium battery electrodes, lithium cobalt oxide, carbon black, and lithium metal were purchased from Sigma-Aldrich, Timcal, and FMC, respectively. In lithium battery and lithium platting and stripping experiments, electrodes were electrically separated by a single porous 20 µm polypropylene separator (Celgard 2075). Commercial electrochemical capacitor jelly rolls (350 F rated) were donated from Maxwell Technologies which had no prior contact with any electrolyte solution.

4.2.2 Electrolytic Conductivity Measurements

Electrolytic conductivity measurements were performed as detailed previously (*47*). Briefly, four electrode electrolytic conductivity measurements were performed with a custom fabricated thin-film platinum sputtered electrode on borosilicate glass. The cell constant was calibrated from 0.1 to 100 mS·cm^{-1} with a measurement accuracy of ± 6%. The thin film electrode ensured there would be no geometric change, and hence cell-constant change, under the increased pressures resulting from the studied electrolytes.

4.2.3 Electrochemical Capacitors

For electrochemical capacitor testing, jelly rolls were dried overnight under vacuum at +180 °C. Custom cells were designed to make a four wire measurements to the jelly roll in order to obtain accurate resistance measurements. All metal contacts were made of aluminum to avoid corrosion issues during cell test. Cell assembly was all done under argon atmosphere.

Resistance (DCR) measurements were calculated from the instantaneous iR drop (captured on a high resolution potentiostat) resulting from a 0.5 Amp discharge current after holding at 3 V for 1 hour. Capacitance was measured as

$$\text{Capacitance} = I \cdot (t_2\text{-}t_1) / (V_2 - V_1)$$

where I, V_2 and V_1 were set at -0.5 Amp, 2.4 and 1.2 V, respectively.

4.2.4 Rechargeable Lithium Metal Battery

For rechargeable lithium metal battery testing, electrode slurries composed of $LiCoO_2$: carbon black : PVDF binder at a 8:1:1 ratio by weight were mixed with an appropriate amount of N-Methyl-2-pyrrolidone (NMP) solvent and doctor bladed onto 25 µm thick stainless steel 316L foil. The thickness of the coated active electrode after cold calendaring was *ca.* 40 µm thick. Active mass loading was *ca.* 0.9 mAh·cm^{-2} or 6.6 mg·cm^{-2} (assuming a theoretical capacity of 137 mAh·g^{-1} when cycled between 3.5 and 4.1 V). Electrodes of 0.31 cm^2 were used for cell testing. Lithium metal was purchased from FMC and was scrapped clean with a glass slide and rolled with a polyethylene rod to a mirror finish prior to all experiments. Electrodes were electrically separated by a single porous 20 µm polypropylene separator and placed inside a custom fabricated coin cell

constructed of high density polyethylene equipped with stainless steel 316L current collectors for both electrodes. All cell assembly was done under an argon atmosphere.

For lithium plating and stripping coulombic efficiency tests, cells were similarly prepared except the LiCoO$_2$ electrode was not used and lithium was directly plated to the stainless steel 316L current collectors, used here as working electrodes, which were polished to a mirror finish. In all tests, all wetted metal components were stainless steel 316 to avoid corrosion issues.

4.2.5 Electrolyte Addition

To form the liquefied gas electrolyte solution, a weighed amount of salt was first pre-loaded into high pressure stainless steel cells along with the capacitor or battery device and sealed under argon atmosphere. The cells were then cooled to a low temperature (*ca.* -60 °C) and a controlled amount of solvent was allowed to evaporate from the source and condense into the cell using a mass flow controller (MKS) through a tube connected to the cell, which was then sealed shut with an attached valve. For comparative studies, conventional liquid electrolytes were added under argon atmosphere prior to cell sealing. Cells for comparative study using liquid electrolytes were otherwise mechanically identical to the liquefied gas electrolyte based cells and electrodes were similarly submerged under electrolyte solution.

4.2.6 Thermal and Electrochemical Characterization

For thermal testing, cells were allowed to thermally equilibrate inside a temperature chamber (Espec) before beginning test. Dry ice was used to cool the cells for tests conducted at -78 °C. Temperature measurements were made from a Type K thermocouple with an uncertainty of ±2 °C and pressure measurements were recorded from a digital pressure transducer (Omega

Engineering) with an uncertainty of ±2% of the measured pressure. Temperature and pressure measurements were recorded with a digital data acquisition system (Agilent).

All electrochemical tests were conducted inside high pressure stainless steel cells equipped with electrical feedthroughs which were electrically connected to test electrodes. Cyclic voltammetry experiments were performed with a sweep rate of 1 mV·sec^{-1}. Non-lithium based electrolytes used sputtered platinum counter and reference electrodes. Lithium based electrolytes used lithium metal counter and reference electrodes. All electrolytes used sputtered platinum working electrodes with an area of 1 mm^2 (exposed area defined by a *ca.* 250 nm thick silicon dioxide passivation layer) on borosilicate glass. Separate platinum working electrodes were used for anodic and cathodic potential regions as well as for each temperature to avoid effects from a previous polarization of the working electrode. Potential windows were calculated at the point where current increased beyond 200 µA·cm^{-2}. Battery electrochemical impedance measurements were conducted with a sinusoidal probe voltage of 5 mV and spectra were fitted with ZView software. All electrochemical capacitor cycling, cyclic voltammetry and impedance measurements were conducted with an SP-200 potentiostat (Bio-Logic).

Lithium battery cell cycling was performed with a battery cycler (Arbin). For LiCoO$_2$ cell tests, cycling consisted of a 100% depth of discharge from 3.5 to 4.1 V for all measurements. For lithium platting and stripping experiments, a single cycle consisted of plating lithium metal to the polished stainless steel 316L working electrode at a current density of 1 mA·cm^{-2} with a total charge transfer of 1 coul·cm^{-2}, followed by lithium stripping at 1 mA·cm^{-2} till the working electrode potential rose above 1 V vs. Li/Li+, at which point the current was immediately reversed and the following cycle commenced. The coulombic efficiency was simply calculated as

$$\text{Efficiency } \% = 100 \cdot (Q_{strip}) \cdot (Q_{plate})^{-1}$$

where Q_{strip} is the amount of charge passed during the lithium stripping cycle and Q_{plate} is the amount of charge plated (1 coul·cm^{-2}) each cycle.

4.2.7 Materials Characterization

Powder x-ray diffractions (XRD) of samples were collected on a either a Bruker D8 or Bruker D2 Phaser using Cu Kα radiation. Continuous scanning of a detector covering angles from 10.0° to 80.0° with a scan rate of *ca.* 0.02° s^{-1} and wavelength of λ= 0.154 nm. Air sensitive samples were sealed under argon atmosphere in polyethylene heat sealed bags and their backgrounds are included in the XRD background spectra.

Fourier transform infrared (FTIR) measurements were conducted with a liquid nitrogen cooled Nicolet 6700 Analytical MCT FT-IR Spectrometer using an Attenuated Total Reflectance (ATR) accessory (single bounce, Diamond/ZnSe crystal). For lithium metal measurements, samples were submerged into Nujol Mineral oil under an argon atmosphere. The samples were then transferred in a sealed vial then quickly clamped down with a polyethylene plastic backing onto the ATR crystal. This allowed Nujol oil to spread around the sample, protecting it from the atmosphere. Measurements over several minutes were made to ensure there was no change in FTIR spectra due to atmospheric reaction.

Scanning electron microscopy images were taken on a FEI XL30 SFEG equipped with Ultra High Resolution (UHR) scanning mode at a beam energy of 5 keV. The lithium metal samples imaged were quickly transferred from a vial sealed under argon atmosphere to the SEM chamber to minimize atmospheric exposure. To measure film thickness, a sharp blade was used to cut down the center of the film and the cross section was viewed under SEM at a 30° angle.

X-ray photoelectron spectroscopy measurements were carried out with a AXIS Supra by Kratos Analytical Inc. using monochromatized Al Kα radiation (hυ = 1486.7 eV) as X-ray source with a base pressure of 10^{-8} Pa. To avoid moisture or air exposure, the XPS spectrometer was directly connected to argon atmosphere filled glove box in which samples were prepared for analysis. The analyzed area of all XPS spectra was 300×700 µm^2. XPS was performed with a pass energy of 15 kV and high resolution scans with a step size of 0.05 eV were collected after a survey scan with a step size of 1.0 eV, for lithium 1s, carbon 1s, oxygen 1s, nitrogen 1s, fluorine 1s, and cobalt 2p regions. All of the obtained XPS spectra were analyzed by CasaXPS software and calibrated with a hydrocarbon C 1s signal at 284.6 eV. Core peaks were performed using nonlinear Shirley-type background. The curves were smoothed by a weighted least-squares algorithm and fitted by line shaped composed of 70% Guassian and 30% Lorentzian. Lithium metal samples were not washed, but in the case of liquid electrolyte, were allowed to dry to remove the majority of the electrolyte from the surface. Cycled LiCoO$_2$ electrodes were discharged to 3.5 V vs. Li before XPS analysis and were washed with dimethyl carbonate to remove residual salt. Samples were prepped under argon atmosphere.

4.2.8 Numerical Calculations

Ionization potentials and electron affinities of solvents were calculated via *ab initio* molecular orbital theory using Gaussian 09W on an isolated molecule in the gas phase. Solvent structures were first geometrically optimized in the ground state at the B3LYP/6-31+g(d,p) level of theory. The ionization potential and electron affinity were calculated from the difference in the electronic energy between the ground state and radical solvent molecules with identical ground state geometry through a vertical electronic transition (Franck-Condon principle). Electrostatic maps of the solvents were visualized via GaussView.

4.3 Physical and Chemical Properties of Liquefied Gas Solvents

The electrochemical stability for a range of liquid and liquefied gas solvents was qualitatively estimated by calculating the ionization potential and electron affinity of the solvents, shown in Supporting Information. Selecting from the solvents with optimal electrochemical stability and polarity, six promising liquefied gas solvents were identified and are compared with conventional liquid solvents in Figure 4.1A. In general, these liquefied gas solvents show improved oxidation and reduction resistance compared to conventional solvents. In particular, these calculations suggest fluoromethane (FM) and difluoromethane (DFM) would have improved electrochemical stability over tetrahydrofuran (THF) and ethylene carbonate (EC) which are known for their high stability at highly reductive and oxidative potentials, respectively. Electrostatic potential maps are overlaid on the physical structures of these solvents for comparison in Figure 4.1B, which may be used as a tool to qualitatively determine electrochemical reduction stability of solvents. The regions of highest electrostatic potential (bluest regions) increases in the order of THF < FM < DFM < EC, which correlates well to the high electrochemical reduction stability of THF and indicates FM should similarly have good reduction stability. The regions of lowest electrostatic potential (reddest regions) increases in the order of EC < THF < FM < DFM, which correlates well with the high solubility for the relatively small Li^+ cation in EC and THF and indicates the solubility would be better in FM than DFM.

The dielectric constant of the gaseous solvents (*ca.* $\varepsilon = 10 \sim 15$) is significantly lower than conventional liquid solvents which may limit their ability to solubilize various salts. However, the room temperature viscosities of the liquefied gas solvents are also significantly lower than conventional liquid solvents. These properties for the liquefied gas solvents fluoromethane and difluoromethane are compared in Figure 4.1C. Both fluoromethane and difluoromethane have a

liquid viscosity about three times lower than acetonitrile, which is commonly used in high power devices such as electrochemical capacitors. Because of their exceptionally low viscosities, it is expected that the ion mobility is quite high in electrolytes composed of these solvents. As a qualitative measure of the electrolytic conductivity for a range of solvents, the ratio of dielectric constant to viscosity ($\varepsilon_r \cdot \eta^{-1}$), or the solvent dielectric-fluidity factor, is compared in Figure 4.1C. It is found that the liquefied gas solvents have a superior dielectric-fluidity factor compared to conventional liquid solvents, including acetonitrile, which generally shows some of the highest electrolytic conductivities.[101] This qualitative comparison demonstrates that relatively high electrolytic conductivities may be expected in these solvents having only moderate dielectric constants. Further, the viscosities of these solvents remain favorable at very low temperatures, as shown in Supporting Information, which may allow for high electrolytic conductivity at temperatures where conventional solvents may freeze.

Vapor pressure curves of the six liquefied gas solvents studied over a range of temperatures are moderate and compared in Figure 4.1D. Of the solvents studied, fluoromethane and difluoromethane have the highest vapor pressures of 3.8 and 1.8 MPa, respectively, at +25 °C. The melting points for each of the solvents are below -100 °C. While the boiling points of these solvents are all below room temperature, the present study utilizes these solvents while they are liquefied under their own vapor pressure in a hermetically sealed cell, allowing for electrolyte and cell characterization at increased temperatures where the solvent would normally be gaseous. Further, these solvents have fairly accessible super-critical points, as detailed in Table 4.1. Having zero surface tension in the super-critical phase, these solvents may provide additional advantages such as superior wetting or access to nano pores in high surface area electrodes.[102]
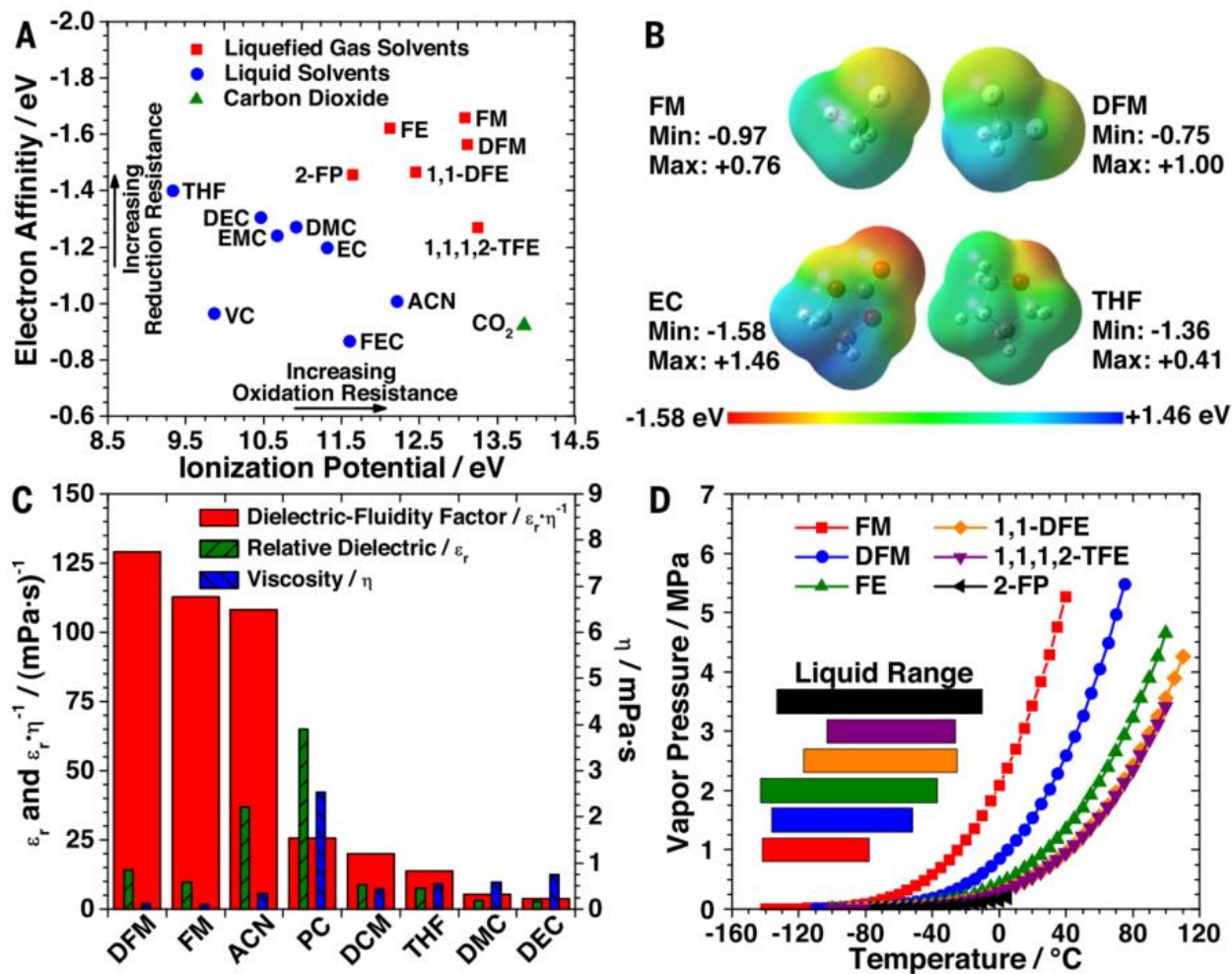
Figure 4.1. Physical and chemical properties of liquefied gas solvents. (A) DFT calculated ionization potentials and electron affinities, (B) electrostatic potential maps, (C) relative dielectric, viscosity, dielectric-fluidity values and (D) vapor pressure curves with liquid range of various conventional and liquefied gas solvents.

Table 4.1. Physical properties of the liquefied gas electrolytes studied.

Solvent	Structure	T_m (°C)	T_b (°C)	T_c (°C)	P_c (MPa)	Vapor pressure (MPa)	M wt (g·mol⁻¹)	Density (g·cc⁻¹)	Dipole (debye)	Relative dielectric	Viscosity (mPa·s)	$\varepsilon_r\cdot\eta^{-1}$ (mPa·s)⁻¹
Fluoromethane		−142	−78	44	5.90	3.41	34.03	0.599	1.85	9.7	0.085	114
Difluoromethane		−136	−52	78	5.78	1.47	52.02	0.981	1.98	14.2*	0.120	118
Fluoroethane		−143	−38	102	5.01	0.79	48.06	0.707	1.94	−	0.125	−
1,1-Difluoroethane		−117	−24	113	4.52	0.51	66.05	0.912	2.26	12.5†	0.173	72
1,1,1-Tetrafluoroethane		−101	−26	101	4.06	0.57	102.03	1.225	2.06	9.7‡	0.207	47
2-Fluoropropane		−133	−9	143	4.20	0.18§	62.09	0.969‖	−	−	−	−

*20°C and 2 MPa. †24°C. ‡30°C. §0°C. ‖−9.4°C.

4.4 Electrolytic Conductivity Measurements

Electrolytic conductivity measurements of the liquefied gas electrolytes were conducted in order to determine the most promising solvents. Various liquefied gas solvents and salts were tested over a range of temperatures and it was found that these electrolytes do not follow typical conductivity vs. temperature curves. Generally, the electrolytic conductivity for a liquid electrolyte will scale approximately linearly with increasing temperature, due to decreasing solvent viscosity. However, the liquefied gas electrolytes show three distinct regions of conductivity over a wide range of temperatures, as shown in Figure 4.2A for 0.1 M TBAPF$_6$ (tetrabutylammonium hexafluorophosphate) in difluoromethane. The first region at lower temperatures shows the typical increasing conductivity with increasing temperature, which is due to the decreasing viscosity with increasing temperatures ($\eta_{DFM,-60°C} = 0.31$ mPa·s, $\eta_{DFM,+20°C} = 0.12$ mPa·s)[103]. At moderate temperatures, there is a clear maximum followed by a gradual decrease in conductivity. As the solvent approaches the super-critical point ($T_{c,DFM} = +78$ °C), a drop in conductivity is expected[104]

and occurs due to the decreasing dielectric constant lowering the ion mobility ($\varepsilon_{DFM,-57°C}$ = 28.2, $\varepsilon_{DFM,+20°C}$ = 14.2)[105,106]. While all solvents generally show a decreasing dielectric constant with increasing temperature, the studied solvents already have a comparably low dielectric constant at room temperature and would be susceptible to considerable ion pairing at increasing temperatures. At even higher temperatures, an abrupt change in the conductivity is observed, which separates the second and third regions of the conductivity curve. Because this sharp change occurs at temperatures considerably lower than the super-critical point, any related phenomena are not thought to contribute to this behavior. It was found that this abrupt change in electrolytic conductivity is concurrent with a sudden increase in the pressure of the electrolyte solution, beyond the normal solvent vapor pressure. This phenomenon may be explained by considering the thermal expansion behavior of the solvent. In practice, nearly the entire volume of measurement cell is filled at a low temperature with liquid solvent, while a small volume remains open, which is naturally filled with gaseous solvent through thermal evaporation. As the temperature increases, the volume of liquid phase increases due to thermal expansion ($\rho_{DFM,-60°C}$ = 1.24 g·cc^{-1}, $\rho_{DFM,+20°C}$ = 0.98 g·cc^{-1})[103] and the volume of the vapor phase decreases. At an elevated temperature, the thermal expansion of the solvent will cause the liquid phase to occupy the entire volume of the cell and any further increase in temperature will result in an isochoric increase in pressure due to the compression of the liquefied gas electrolyte. It should be cautioned that rather high pressures may be observed if solvent thermal expansion is restricted considerably. An increase in pressure on difluoromethane can increase the dielectric constant of the solvent quite dramatically.[107] Therefore, it may be understood that the abrupt change in electrolytic conductivity in the third region relative to second region of Figure 4.2A is due to an improvement in ion mobility from the increased dielectric constant of the solvent, which results from the increased pressure on the electrolyte

system. While this pressure induced effect may be generalized to all electrolytes, it is a particularly significant effect due to the already moderate dielectric constant and high compressibility of this solvent.

Similar electrolytic conductivity phenomena may be observed for the other liquefied gas electrolyte systems explored. The electrolytic conductivity of 0.1 M EMITFSI (1-Ethyl-3-methylimidazolium bis(trifluoromethylsulfonyl)imide) in multiple liquefied gas solvents is shown in Figure 4.2B and decreased in the order of difluoromethane, fluoromethane, 1,1-difluoroethane, fluoroethane, 2-fluoropropane, and 1,1,1,2-tetrafluoroethane. This follows the order of decreasing dielectric-fluidity factors for the solvents described previously in Table 4.1, which gives credibility to the simple qualitative model proposed (the dielectric constants for fluoroethane and 2-fluoropropane were unavailable in the literature). Since difluoromethane was found to exhibit the highest electrolytic conductivity, various salts were tested in this solvent, shown in Supporting Information. It was found that $TBAPF_6$ exhibited the highest electrolytic conductivity in difluoromethane and further studies of this electrolyte system were studied with various concentrations of salt, shown in Figure 4.2C. There is a considerable increase in the conductivity of the liquefied gas electrolyte from a concentration of 0.02 to 0.50 M $TBAPF_6$, which shows the salt has good solubility in difluoromethane despite its relatively low dielectric constant. The electrolytic conductivity of the 0.50 M solution shows a maximum conductivity of 31 mS·cm^{-1} at +30 °C. More notable, however, is the excellent low-temperature conductivity of 13 mS·cm^{-1} at -60 °C. Previous work showed the optimization of binary mixtures of liquid based solvents with close attention to the conductivity, melting points and potential window, and demonstrated a similar electrolytic conductivity at -60 °C for 0.75 M $TEABF_4$ (tetraethylammonium tetrafluoroborate) in acetonitrile : methyl formate 3:1, however, the potential window of this

electrolyte was limited.[108] Figure 4.2C shows that at various concentrations, the conductivity curves exhibit the same general three-regions of electrolytic conductivity across the temperatures measured. A distinct change in the slope of the conductivity curve in the first region, most notably at a concentration of 0.5 M TBAPF$_6$, is thought to be due to increasing ion pairing which is expected to occur in these moderate dielectric solvents with high salt concentrations. There is a gradual change in the temperature separating the second and third regions, which increases from +35 °C to +79 °C from a salt concentration of 0.02 M to 0.5 M. This may be understood by the lower thermal expansion coefficient of the solution with increasing salt concentration, which would require more thermal energy to volumetrically expand and create the isochoric increase in pressure, in turn resulting in the abrupt change in conductivity.

While difluoromethane was shown to have an exceptionally high electrolytic conductivity with many salts, it was found that this solvent was unable to solubilize lithium salts. This is likely due to the steric hindrance of the highly electronegative fluorine atoms of adjacent solvent molecules preventing formation of a solvation shell around the Li$^+$ cation. Further work showed that lithium bis(trifluoromethane)sulfonimide (LiTFSI) could only be solubilized in the mono-fluorinated liquefied gas solvents; fluoromethane, fluoroethane, and 2-fluoropropane. This is in agreement with previous work which also suggested these mono-fluorinated solvents have an increased basicity and binding energy to the Li$^+$ cation over difluoromethane[109] and with the previously discussed electrostatic potential maps of the solvents in Figure 4.1B. The electrolytic conductivities of these three mono-fluorinated liquefied gas solvents with 0.1 M LiTFSI are compared in Figure 4.2D. Fluoromethane is shown to have the highest electrolytic conductivity of the three solvents, as is expected from the exceptionally high dielectric-fluidity factor. A maximum conductivity of 1.2 mS·cm^{-1} is seen at -22 °C and an impressive low temperature conductivity of

1.1 mS·cm^{-1} at -60 °C. For comparison, a low temperature electrolyte using LiPF$_6$ in a mixture of carbonates and methyl acetate had an electrolytic conductivity of 0.6 mS·cm^{-1} at -60 °C, but it had relatively poor performance in a full cell due to the non-ideal solvent system.[110] The electrolytic conductivity at higher concentrations saw little improvement with the LiTFSI salt. At higher temperatures, there is a sudden drop in conductivity due to the precipitation of the salt out of the electrolyte as fluoromethane reaches its critical temperature (T$_{c,FM}$ = +44 °C), which is a useful safety feature among lithium based electrolytes.
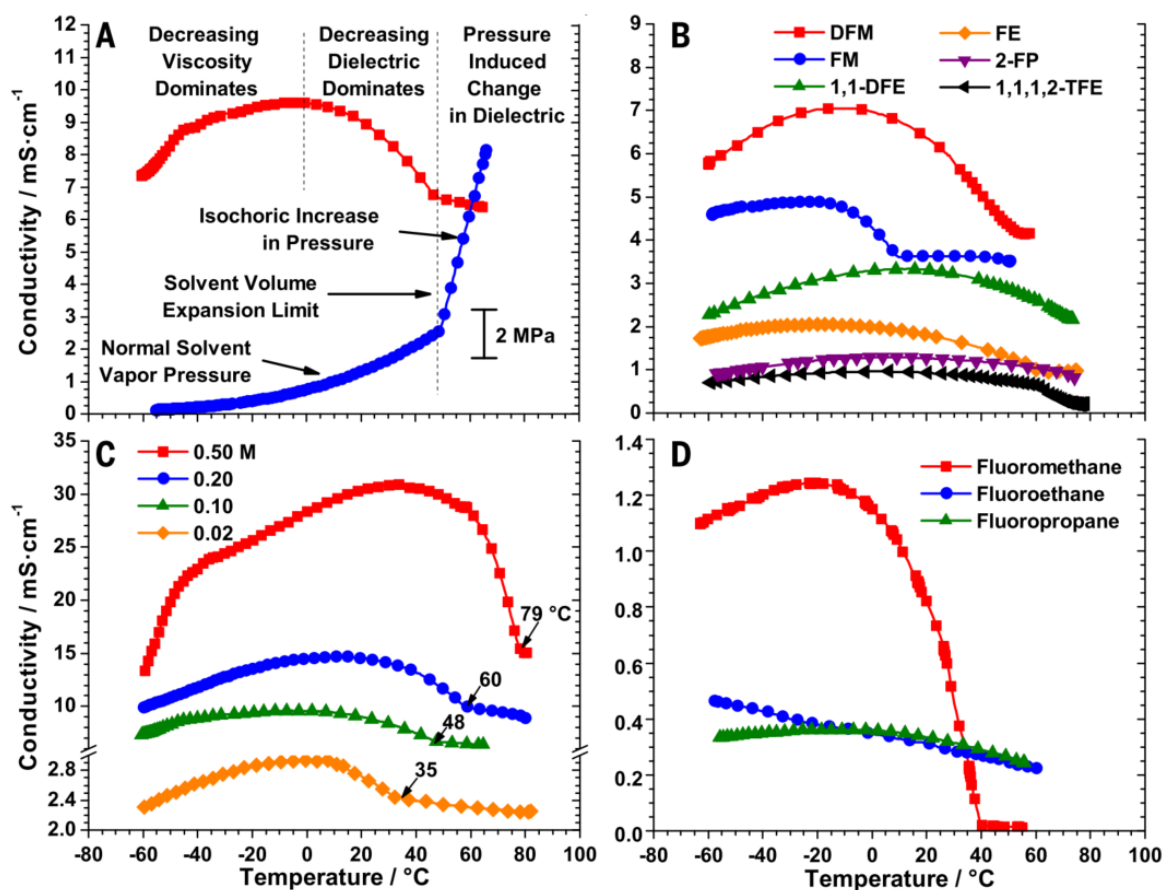
Figure 4.2. Electrolytic conductivity of liquefied gas electrolytes. (A) 0.1 M TBAPF$_6$ in difluoromethane, (B) 0.1 M EMITFSI in various liquefied gas solvents, (C) TBAPF$_6$ in difluoromethane and (D) 0.1 M LiTFSI in various monofluorinated liquefied gas solvents.

4.5 Electrochemical Capacitors

Since difluoromethane shows the highest electrolytic conductivity for non-lithium based salts, the electrochemical stability of this solvent was studied. Figure 4.3A shows the cyclic voltammetry curves for 0.1 M TEABF$_4$ in difluoromethane at both +25 °C and -60 °C. At +25 °C, a potential window of 5.70 V is observed. The positive potential limit of 2.47 V vs. Pt matches well with that of anion oxidation.[95] A significant reduction current is observed with an onset potential of -3.23 V vs. Pt which results in the continuation of a high reduction current in the reverse sweep direction, possibly due to corrosion of the working electrode. These potential limits are in good agreement with previous results with a similar salt system.[95] At -60 °C, the electrolyte shows an impressive electrochemical window of 6.83 V, which is wider than that at +25 °C due to slower chemical kinetics at the decreased temperatures.

Commercial electrochemical capacitors of 350 F rated capacitance were tested with 0.5 M TEABF$_4$ in difluoromethane and with a standard liquid electrolyte composed of 1 M TEABF$_4$ in acetonitrile for comparison, both of which were tested under identical mechanical cell conditions and submerged in electrolyte. The capacitance and resistance over a range of temperatures is shown in Figure 4.3B. At +25 °C, the capacitance for both devices is *ca.* 375 F and remains fairly constant over the temperature range studied, with only a small decrease to *ca.* 350 F at low temperatures. The resistance of 8.5 and 11.0 mΩ for the difluoromethane and acetonitrile devices, respectively, at +25 °C emphasizes the high electrolytic conductivity and applicability of the electrolyte to electrochemical capacitors for high power applications. At low temperatures, while the acetonitrile based device steadily increased in resistance to 14.9 mΩ at -40 °C, just above its freezing point, the difluoromethane based device decreases in resistance to 5.8 mΩ at -20 °C. This is in agreement with the electrolytic conductivity measurements which show a maximum in

electrolytic conductivity around this temperature range. At lower temperatures, the resistance slowly increases, yet is still comparable at -78 °C and +25 °C, highlighting the excellent low-temperature performance of the electrolyte. This operation temperature is nearly 40 °C lower than commercial acetonitrile based electrochemical capacitors are rated for and is unsurpassed by other low-temperature electrolyte formulations.[111] At an elevated temperature of +65 °C, the resistance increases only slightly to 13.4 mΩ. Device cycling performance was also studied with difluoromethane in the super-critical phase, shown in Supporting Information. Though the capacitance of the device is maintained, there is a substantial increase in electrolyte resistance at +90 °C (*ca.* 1500% increase) as the salt precipitates out of the solvent due to the decreasing dielectric constant. When the temperature is lowered, the resistance decreases to nominal as the salt is solubilized back into solution and shows a slight decrease in capacitance due to accelerated cell degradation at the high temperature.

To determine if the novel difluoromethane based electrolyte offers any advantage in terms of energy density, electrochemical capacitors were tested at an elevated voltage and temperature of 3.0 V and +65 °C for over 1500 hours, shown in Figure 4.3C. The device using the acetonitrile based electrolyte rapidly fails under these accelerated conditions, showing a substantial increase in resistance and decrease in capacitance, which agrees with previous studies of electrochemical capacitors under similar conditions.[112] The difluoromethane device, however, shows little decrease in capacitance or increase in resistance under identical conditions. Similarly, a 3.0 V test was carried out at -60 °C to test the low temperature life of the device and shows nearly no change in capacitance or resistance. With a comparable capacitance already demonstrated, the increased voltage rating from 2.7 V (for typical acetonitrile devices) to 3.0 V is equivalent to a 23% increase

in energy density which offers an advantage for a range of electrochemical capacitor applications such as cold engine cranking, start-stop vehicles and hybrid buses.
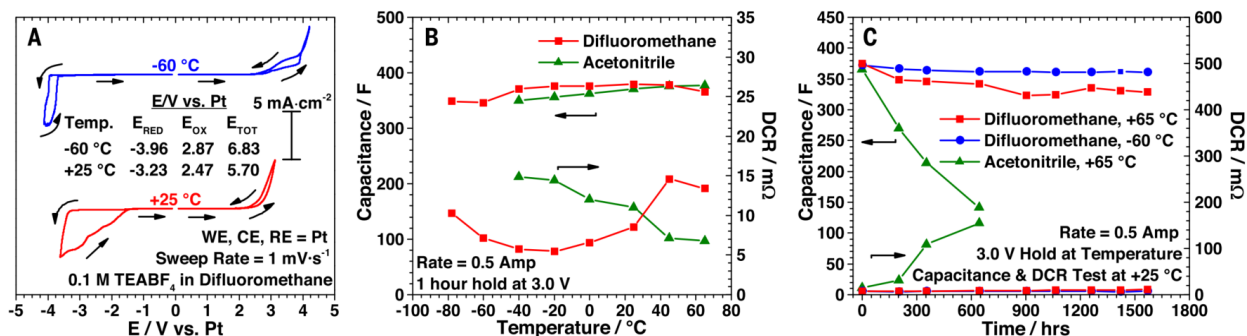
Figure 4.3. Electrochemical stability of difluoromethane and its use in electrochemical capacitors. (A) Cyclic voltammetry curves at +25 and -60 °C. Capacitance and resistance measurements of symmetric 350 F electrochemical capacitors (B) over temperatures from -78 to +65 °C and (C) over time with accelerated life testing at 3.0 V at -60 and +65 °C.

4.6 Rechargeable Lithium Metal Battery

Due to the high reduction potential of lithium (-3.04 V vs. NHE) a thin electrically insulating, but Li-ion conducting solid electrolyte interphase on the lithium metal instantaneously forms when in contact with many commonly used liquid solvents. Optical images of the resulting chemical products after soaking lithium metal in each of the liquefied gas solvents are shown in Supporting Information. The poly-fluorinated solvents (dilfuoromethane, difluoroethane and 1,1,1,2-tetrafluoroethane) each form a stable SEI on lithium metal preventing further decomposition of the lithium metal or solvent. Though thorough characterization of these interfaces was not done on these chemical products, the SEI is thought to be significantly made up of various fluoropolymers. The mono-fluorinated solvents (fluoromethane, fluoroethane, 2-fluoropropane), which are capable of solubilizing lithium salts, each fully decompose lithium

metal into a powder form and no stable SEI is formed. As detailed in Supporting Information, the reaction time for the full decomposition of lithium metal at room temperature in liquid fluoromethane is significantly slower than in liquid fluoroethane or 2-fluoropropane. The chemical reduction of fluoromethane by lithium metal is hypothesized to follow as

1). $CH_3F + Li \rightarrow LiF + CH_3^\bullet$

2). $Li + CH_3^\bullet \rightarrow CH_3Li$

3). $CH_3^\bullet + CH_3^\bullet \rightarrow C_2H_6$
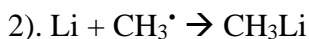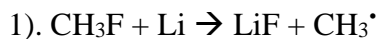
Evidence for LiF and CH_3Li among the chemical products is seen in the x-ray diffraction (XRD) and fourier transform infrared spectroscopy (FTIR) spectra shown in Supporting Information, respectively, which supports this reaction scheme. Since the kinetics for lithium decomposition in fluoromethane are relatively slow, and it is this solvent which had the highest electrolytic conductivity with lithium salts as seen in Figure 4.2D, methods to stabilize the surface of lithium metal were explored. It was found the use of carbon dioxide in additive amounts in fluoromethane was sufficient enough to stabilize the lithium surface, due to the creation of a stable lithium carbonate surface layer. The formation of this stable interface is shown in Supporting Information, which show little evidence for LiF or CH_3Li in the SEI layer on the macroscopic level with the addition of 5 wt% carbon dioxide. Carbon dioxide is an effective additive for use in Li-ion batteries[113] but solubility in common organic solvents is limited to *ca.* 0.5 wt% and strongly dependent with temperature.[114] Conversely, carbon dioxide and fluoromethane are miscible solvents[115] and may enable the use of this highly effective additive in next generation batteries.

With the addition of carbon dioxide to form a stable SEI layer on lithium metal, the electrochemical stability of the fluoromethane based liquefied gas electrolyte was determined by cyclic

voltammetry, shown in Figure 4.4A and in more detail in Supporting Information. The electrolyte is limited by oxidation at 5.57 and 5.79 V vs. Li at +25 °C and -60 °C, respectively, which is indicative of slower solvent oxidation kinetics at decreased temperatures. Carbon dioxide reduction is seen to begin at 2.1 V vs. Li, which matches well with the literature.[116] Typical lithium metal plating and stripping peaks are observed to be centered around 0 V vs. Li. While the cathodic upper potential deposition peaks for lithium and platinum alloying are not observed due to concurrent carbon dioxide reduction, two anodic upper deposition potential stripping peaks are observed; a larger peak followed by a smaller peak at 0.58 and 1.32 V vs. Li, respectively. At -60 °C, a relatively high over potential for lithium nucleation is also observed, with lithium deposition starting at -0.39 V vs. Li.

Lithium metal is known to suffer from poor coulombic efficiency and severe dendrite growth in conventional electrolytes,[117] but because it has the highest gravimetric capacity of all possible anodes (3863 mAh·g^{-1}) there are still numerous efforts to try to enable this anode in a rechargeable battery. Using solvents of low viscosity[118], increased pressure on the electrode[119] and a surface coverage of LiF[120] are all promising methods to improve the lithium metal anode cyclability and lower the severity of dendrite formation. The exceptionally low viscosity, high vapor pressure and LiF chemical reduction products are all properties inherent to the fluoromethane liquefied gas solvent. To explore the effectiveness of the proposed electrolyte system in enabling the lithium metal anode, the coulombic efficiency of lithium plating and stripping was measured on polished stainless steel electrodes. As shown in Figure 4.4B, the fluoromethane based electrolyte shows a stable and high coulombic efficiency of *ca.* 97% over 400 cycles at an aggressive 1 mA·cm^{-2} plating and stripping rate with 1 coul·cm^{-2} of lithium being passed each cycle. For comparison, a conventional liquid electrolyte system (1 M LiPF$_6$ in

EC:DEC 1:1) is shown to have a poor and unstable coulombic efficiency under identical cell conditions. The comparative fluoromethane and liquid electrolyte lithium plating and stripping cells were stopped at 400 cycles to examine the stainless steel substrates with scanning electron microscopy. The surface morphology of the deposited lithium layer from the fluoromethane based electrolyte is found to be highly uniform with micron sized grain-like features and no evidence of dendrite growth (Figure 4.4C). This is in contrast to the highly polymeric and dendritic like surface observed from cycling in the liquid electrolyte. Further, the thickness of the deposited lithium layer in the fluoromethane and comparative liquid electrolyte is found to be *ca.* 60 and 460 µm thick, respectively, reflecting the far superior coulombic efficiency of the novel electrolyte system. The coulombic efficiency for lithium plating and stripping compares with reported values for diethyl ether : tetrahydrofuran 95:5 (98%)[121], 2-methylfuran (97%)[122], and 1,2-dioxolane (98%)[13]. The high efficiencies in these systems are only seen with the use of the toxic lithium hexafluoroarsenate ($LiAsF_6$) salt which is reduced at the lithium metal surface to form a LiF passivation layer. In the fluoromethane system, the solvent itself forms a LiF layer when reduced, which removes the need for $LiAsF_6$ salt. In addition, the reduction of carbon dioxide to form lithium carbonate has been shown to improve the impedance and cyclability of the lithium metal anode,[123] which is used to stabilize the electrode in the present study. More recently, other electrolyte systems have been shown to have high lithium plating and stripping efficiencies without the use of $LiAsF_6$, but none have demonstrated suitable oxidation stability for use with conventional 4 V cathode systems due to the poor stability at increased potentials of these ether based electrolyte.[124] These electrolytes are mostly limited to cathode chemistries which have a low potential and limit the oxidation of these solvents, however, the ability to use a lithium metal anode with a high voltage intercalation cathode would offer a significant increase in energy density as well.

A lithium cobalt oxide ($LiCoO_2$) cathode was used to demonstrate the high oxidation stability and compatibility of the fluoromethane based liquefied gas electrolyte with traditional cathode materials. Fluoromethane and conventional liquid based electrolyte systems were used for comparison to test this cathode under identical cell conditions. All charging and discharging of cells was done at a fixed temperature, rather than charging at a higher temperature followed by discharge at a lower temperature. The electrode performance in both electrolyte systems is shown over a number of cycles at various temperatures and C-rates (Figure 4.4D) with corresponding voltage vs. discharge capacity curves (Figure 4.4E). At +25 °C, the discharge capacity at the C/10 rate is very similar, showing *ca.* 133 mAh·g^{-1} using both electrolytes. At higher rates, the performance of the liquid electrolyte system is marginally higher than the fluoromethane based electrolyte, showing a capacity retention of 87.2% and 81.2% at the 1C rate, respectively. However, at lower temperatures the high rate performance of the fluoromethane based electrolyte is far superior. At -10 °C and at the C/10 rate, the fluoromethane and liquid based electrolytes show a 98.3% and 86.2% discharge capacity retention relative to +25 °C, respectively. At higher rates or lower temperatures, the liquid based electrolyte fails to cycle properly due to a high cell impedance. In contrast, the cell utilizing the fluoromethane based electrolyte cycles fairly well at higher rates at various temperatures, most notably showing an excellent capacity retention of 60.6% at the C/10 rate at -60 °C where traditional liquid electrolytes would generally freeze. This compares favorably with a specially developed low-temperature liquid based electrolyte that shows a discharge capacity retention of 43.5% at the C/10 rate at -60 °C using a significantly larger capacity full cell.[125] Impedance spectra for cells at each temperature and fitted parameters are shown in Supporting Information. Stability of the fluoromethane based electrolyte system is compared to the liquid electrolyte in Figure 4.4F at +25 °C and at a C/2 rate. Both electrolytes show very similar

stability, with the fluoromethane based electrolyte showing a 96.7% capacity retention after 100 cycles, which demonstrates the high compatibility of this electrolyte system with conventional 4 V cathodes.
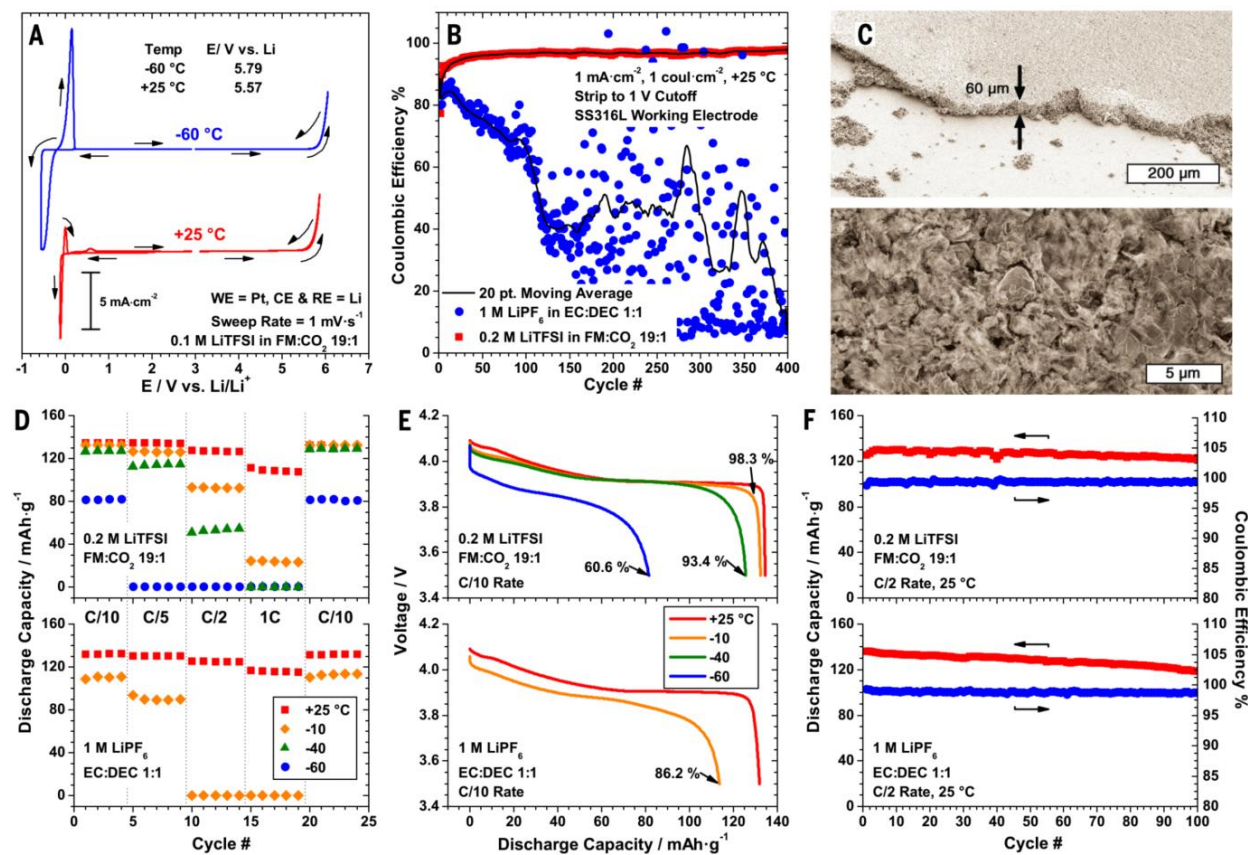
Figure 4.4. Electrochemical stability of fluoromethane and its use in lithium batteries. (A) Cyclic voltammetry curves. (B) Coulombic efficiency and (C) SEMs of cycled lithium anode. (D) Discharge capacity, (E) voltage curve over various temperatures and (F) Li-LiCoO$_2$ full cell cycling.

The low conductivity of traditional liquid electrolytes is not a primary source of the limited low-temperature performance of Li-ion cells.[126] The true origin of these limitations is likely due to charge transfer or solid electrolyte interphase impedance and is sensitive to the type of electrodes and electrolyte used.[127,128] Because identical anodes and cathodes were used in these studies, it is

52

thought the high performance of the fluoromethane based electrolyte at such low temperatures is due to the significantly improved SEI layer on the electrodes. To further explore the electrode-electrolyte interphases seen in the fluoromethane based electrolyte, x-ray photoelectron spectroscopy (XPS) analysis was conducted on both the lithium metal anode and $LiCoO_2$ cathodes. As seen in Figure 4.5, the surface of lithium metal submerged in fluoromethane is significantly composed of LiF and CH_3Li with a minor Li_2CO_3 signal originating from impurities within the lithium metal. The addition of carbon dioxide to stabilize the surface further adds a significant Li_2CO_3 component to the SEI and lowering of the CH_3Li component, results which agree with the XRD and FTIR analyses. After cycling, the surface components show little chemical change and retain a highly ceramic-like SEI composed primarily of LiF and Li_2CO_3, in contrast to the highly polymer-like SEI formed on the surface on lithium metal submerged in conventional carbonate based electrolytes. The formation of a thin Li_2CO_3 layer via carbon dioxide reduction and the high mobility of lithium ions through the grain boundaries of the highly ceramic surface are thought to both contribute to a substantially decreased impedance through the anode SEI layer. Further, the highly chemically uniform interface as seen in the fluoromethane based electrolyte is thought to contribute to a more uniform current distribution which prevents dendrite formation.[129]
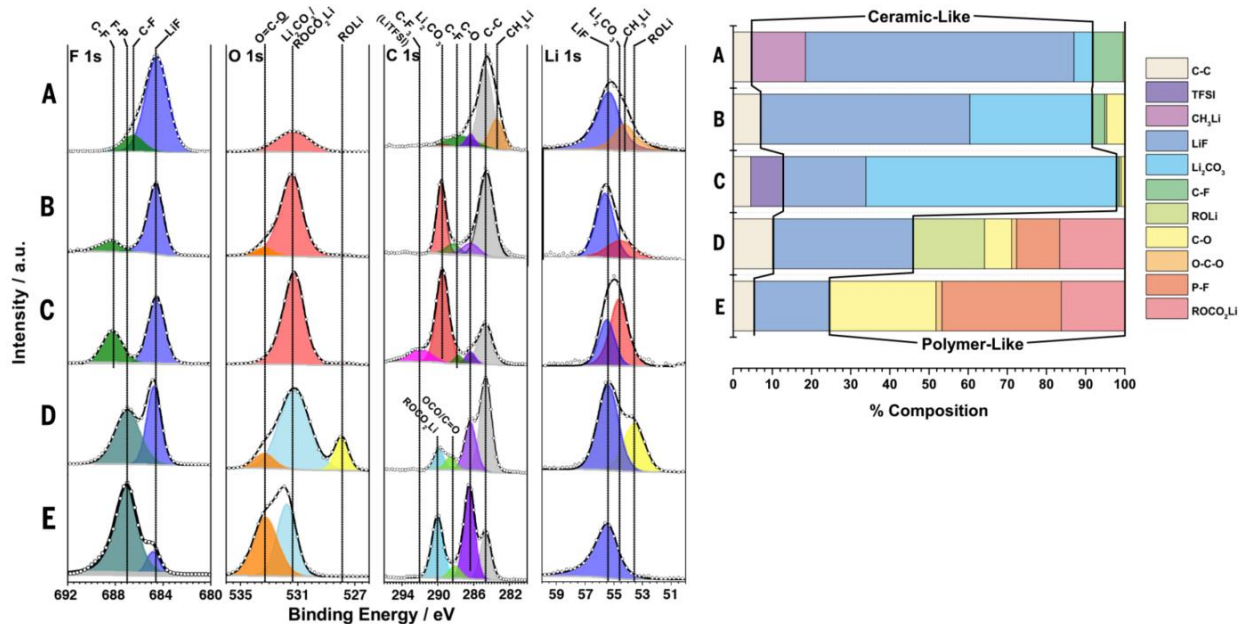
Figure 4.5. XPS of lithium metal surface products. Lithium metal after being submerged in fluoromethane (A) and FM:CO₂ 19:1 (B) for three days, cycled 400 times in 0.2 M LiTFSI in FM:CO₂ 19:1(C), submerged (D) and cycled 400 times (E) in 1 M LiPF₆ in EC:DEC 1:1.

While the improvement on the anode is expected to improve cell performance, previous studies have shown that a significantly higher impedance occurs on the cathode, rather than on the anode, at low temperatures.[130] The chemistry of the cathode-electrolyte interphase was examined via XPS, shown in Figure 4.6. Comparing the XPS spectra of LiCoO₂ electrodes before cycling and after cycling, there are surprising differences. Other than evidence of a small amount of residual LiTFSI salt, there is no change in the Li 1s, C 1s, F1s and Co 2p spectra for the electrode cycled in the fluoromethane based electrolyte. In contrast, the electrode cycled in the conventional liquid electrolyte shows a significant increase of LiF on the surface of the electrode from decomposition of the PF₆⁻ anion. While the O 1s shows the typical increase in polymeric-type species in agreement with other work,[131] the change occurring in the O 1s spectra of the electrode cycled in the fluoromethane based electrolyte is not as clear. Since carbon dioxide is expected to

be stable at the potentials seen at this electrode surface and there is no other source of oxygen, the increased peak seen in the O 1s spectra is thought to be due to a change of the surface oxygen of the LiCoO₂ electrode[132] and not related to the formation of an additional surface layer on the electrode. It is concluded that the improved SEI on lithium metal and a cathode with little or no SEI both contribute to the exceptionally high performance at low temperatures of lithium batteries using these liquefied gas electrolytes.
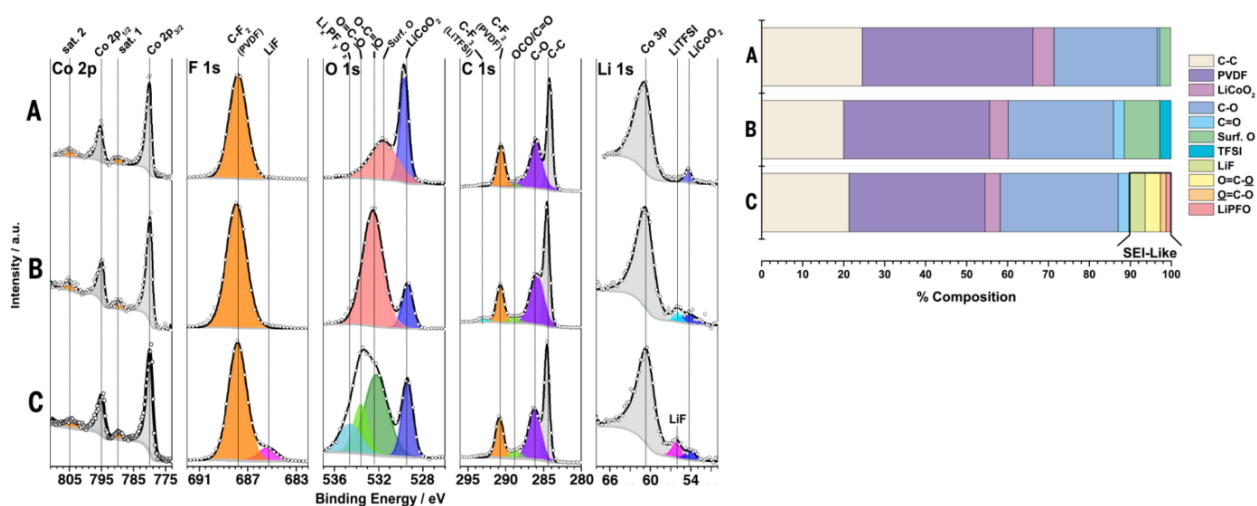
Figure 4.6. XPS of a LiCoO₂ electrode. Electrodes (A) before cycling and after cycling five times from 3.5 to 4.1 V vs. Li with (B) 0.2 M LiTFSI in FM:CO₂ 19:1 and (C) 1 M LiPF₆ in EC:DEC 1:1.

4.7 Conclusion

Through a combination of superior physical and chemical properties, hydrofluorocarbon based liquefied gas electrolytes are shown to be compatible for energy storage devices. The low melting points and high dielectric-fluidity factors of these liquefied gas solvents allows for exceptionally high electrolytic conductivities over a range of temperatures. High performance in electrochemical capacitors and lithium batteries at temperatures as low as -78 °C and -60 °C,

respectively, has been demonstrated for potential use in aerospace and high-atmosphere applications. Comparable conductivities and performance to conventional electrolytes at moderate temperatures has also been shown, which may be applicable to more mainstream applications such as hybrid and electric vehicles. With the use of difluoromethane as an electrolyte solvent, electrochemical capacitor operation at an increased voltage under accelerated life conditions has been demonstrated, equating to a 23% increase in energy density. With the use of fluoromethane as an electrolyte solvent, a high coulombic efficiency of *ca.* 97% for lithium metal plating and stripping with no evidence of dendritic growth as well as the compatibility with the traditional 4 V $LiCoO_2$ cathode offers a promising path towards developing a high energy density rechargeable lithium metal battery.

This chapter in full, is a reprint of the material "Liquefied gas electrolytes for electrochemical energy storage devices" as it appears in Science, Rustomji, C. S.; Yang, Y.; Kim, T. K.; Mac, J.; Kim, Y. J.; Caldwell, E.; Chung, H.; Meng, Y. S., 2017, 356(6345). The dissertation author was the co-primary investigator and second author of this paper. The author involved in all the tests and performed all the batteries tests and XPS characterization.

Chapter 5. High-Efficiency Lithium-Metal Anode Enabled by Liquefied Gas Electrolytes

5.1 Introduction

With the highest specific capacity (3860 mAh·g⁻¹), and the lowest electrochemical potential (-3.04 V vs. SHE), the lithium (Li) metal anode has long been considered as the "holy grail" of Li-based battery chemistry.[4,18,133–135] Nevertheless, its practical application has been hindered by numerous challenges over the past several decades, including dendrite growth, low coulombic efficiency (CE), and large volume change.[4,5,7,136] Due to the high reactivity of Li metal, electrolytes are readily reduced and form a solid electrolyte interface (SEI) on the anode surface. Although the SEI can passivate the Li metal surface, the inhomogeneous physical-chemical nature of the SEI often induces dendrite formation, resulting in battery failure and safety concerns. The dendrite growth also causes the formation of inactive Li during cell discharge and creates a porous Li metal structure, which consumes both active Li and electrolyte, thus decreasing both CE and cycle life.

The nature of Li deposition and the properties of the SEI (ionic conductivity and mechanical stability) are closely correlated with the properties of the electrolyte (viscosity, ionic mobility, pressure, transport properties, etc.)[16], which are key to suppress the dendritic growth, improve CE and enhance cycling stability of the Li metal anode. There is currently a global effort to develop various electrolyte formulations to enable solutions which address these shortcomings of the Li metal anode. With a relatively flexible and stable SEI, ether-based electrolytes deliver a CE of about 95-99%, but their applications are hindered by their low oxidation stability (<4.0 V vs. Li).[7,13,15] Despite their high oxidation stability (4.3 V vs. Li) and successful commercialization

in Li-ion batteries, carbonate-based electrolytes decompose into polymer-like SEIs which show poor compatibility with Li metal, causing low CE and dendrite growth.[56] Efforts were also made to form more ceramic-like SEIs by tailoring additives[32], solvents[74], salts[30], and their ratios[61,63,137]. Notably, high-concentration electrolytes have been shown to minimize solvent decomposition and form LiF-rich SEIs via salt decomposition which enables Li metal cycling with a relatively high CE of ~99%.[61] It has also been shown that high-concentration electrolytes may also improve the oxidation stability of ether-based electrolytes by reducing free ether molecules.[63,69] Recently, the disadvantages of high-concentration electrolytes, such as high cost, high viscosity, and poor wettability, have been partially mitigated by diluting the electrolyte with non-solvating solvents to form localized high-concentration electrolytes.[36,71] However, the low-temperature performance and rate capability of the localized high-concentration electrolytes are inferior even to conventional electrolytes. Lastly, a newly developed electrolyte composed of 1 M $LiPF_6$ in a mixture of all fluorinated ether and carbonate solvents shows excellent stability with Li metal (CE >99%)[74], which highlights the positive contribution of fluorinated electrolytes to SEI formation.

The recently developed fluoromethane (CH_3F, FM)-based liquefied gas electrolyte enables dendrite-free Li metal cycling with relatively high efficiency (97.5%) by forming a dense, uniform, ceramic-based SEI layer, composed primarily of LiF and Li_2CO_3.[39] As demonstrated in this earlier work, the solvent itself, rather than the salt, plays a more critical role in stabilizing the Li metal. Additionally, the low melting point and low viscosity of these electrolytes enable low-temperature operation as low as -60°C. However, cell performance in this previously reported work was limited by the low salt solubility and the correspondingly high polarizations. In the present study, the limited salt solubility and high polarizations are resolved by introducing tetrahydrofuran (THF) as

a co-solvent. The solvation structure and improved lithium transport of the electrolyte are more thoroughly understood through a combination of experimental and computational techniques. Additionally, thorough analyses of the Li metal morphology and structure of the SEI are carried out to understand the excellent stability, CE, rate capability, and low-temperature performance achieved by the new liquefied gas system with the Li metal anode.

5.2 Materials and methods

5.2.1 Materials

Fluoromethane (99.99%) was obtained from Air Liquide. The salts lithium hexafluorophosphate ($LiPF_6$) (99.9%) and lithium bis(trifluoromethane)sulfonimide (LiTFSI) (99.9%) were purchased from BASF. 1M $LiPF_6$ in EC: DEC 1:1 (LP40) was purchased from BASF. Tetrahydrofuran (THF, anhydrous, 99.9%), 1,2-dimethoxyethane (DME, 99.5%), and 1,3-dioxolane (DOL, 99.8%) were purchased from Sigma-Aldrich and stored over molecular sieves.

5.2.2 Electrochemical measurements

Electrolytic conductivity measurements were carried out in a custom fabricated high-pressure stainless-steel cell, in which polished SS 316L were used as both electrodes. The cell constant was calibrated from 0.447 to 80 mS·cm^{-1} using OAKTON standard conductivity solutions.

Electrochemical impedance spectroscopy measurements were conducted with a sinusoidal probe voltage of 5 mV from 0.1 Hz to 1 MHz in the same device. The impedance of Li plating/stripping cells were measured after 20 cycles (1 mAh·cm^{-2}, 0.5 mAh·cm^{-2}). The spectra were fitted by an equivalent circuit model using ZView software.

Battery cycling performance was evaluated by an Arbin battery test station (BT2043, Arbin Instruments, USA) in custom designed coin cells, with Li metal (FMC Lithium, 1 mm thickness, ¼ inch diameter) as the counter electrode and a polished stainless-steel (SS316L) as the working electrode. A single 20 µm porous polypropylene separator (Celgard 2075) was used for all the electrochemical experiments.

For Li metal plating and stripping experiments, lithium was first deposited onto the working electrode at 0.5 mA·cm^{-2} until 0 V vs. Li and the voltage was held for 5 hours to form a stable SEI on the current collector, the capacity of which is around 0.02-0.04 mAh·cm^{-2} and is also accounted for in the first cycle efficiency. The first plating cycle was then started, followed by complete lithium stripping to a 1 V vs. Li cut off voltage. For one-time deposition, a total charge of 1 mAh·cm^{-2} was transferred at current density of 0.5 mA·cm^{-2}. The current collector with deposited Li was taken from the glovebox for further characterization and analysis. For long-term lithium metal cycling, the cells were cycled at a specific current density and capacity, with a cutoff potential of 1 V vs. Li for Li stripping under the same current density. The CE was calculated as the Li stripping capacity divided by the Li plating capacity during a single cycle. For the rate and temperature test, the cell was placed in a temperature chamber (Espec), soaked at the testing temperature for several hours, then was cycled with capacity of 1 mAh·cm^{-2} for 3 cycles at each selected current density (from 0.1 to 10 mA·cm^{-2}) at each selected temperature (from +20 to -60°C), respectively.

Coulombic efficiency uncertainty was calculated by finding the error in current measurement from the Arbin using a current equivalent to that used in lithium plating/stripping experiments (0.5 mA/cm^2). Current measurements were made through a calibrated ammeter and a shunt resistor in series with the Arbin. Errors on several Arbin channels were measured. When

describing the uncertainty in the measurements, we report the largest error seen among the channels tested. These come out to be a 0.30% underestimation, and a 0.29% overestimation of the measured efficiency – which are rounded to measurement uncertainties of $\pm 0.3\%$.

Room temperature cycling of the 18650 form factor cells with the liquefied gas was performed in conventional 18650 nickel-plated steel cans (0.25 mm wall thickness) using a custom designed cell cap to enable liquefied gas electrolyte injection and contain the pressurized electrolyte.

5.2.3 Electrolyte addition

Electrolyte addition procedures have been described previously.[39]

5.2.4 Material characterization

Scanning electron microscopic (SEM) images were collected with a Zeiss Sigma 500 Field-emission equipped with Ultra High Resolution (UHR) mode operating at 5 kV, 0.1 nA.

Cryogenic focused ion beam (Cryo-FIB) (FEI Scios DualBeam equipped with a CryoMat integrated cryo-stage and air-free quick loader) was applied to explore the morphology of the cross-section and bulk structure of electrochemically deposited Li. To reduce curtaining artifacts during milling, the samples were coated with organometallic platinum at room temperature using a gas injection system. To minimize the beam damage, at high vacuum (~10^{-6} mbar) the samples are cooled down to -170°C and maintained under continuous chilled nitrogen gas cooling during SEM imaging and FIB operation. To prepare cross-sectional images samples were rough milled with a cross-sectional cut (30 kV, 5 nA) followed by a cross-sectional cleaning cut (30 kV, 0.5 nA). To explore the 3D bulk structure, cross-sectional images were sequentially collected while

continuously milling through a large sample area. Using Amira-Avizo software these images were segmented to generate a 3D reconstruction model for quantitative analysis.

X-Ray photoelectron spectroscopy (XPS) was performed using a Kratos AXIS Supra DLD XPS with monochromatized Al Kα radiation (λ= 0.83 nm and hυ=1486.7 eV) under a base pressure <10^{-8} Pa. To avoid moisture and air exposure, samples were transferred to the XPS chamber directly from a glovebox via vacuum transfer. All spectra were calibrated with hydrocarbon C 1s (284.6 eV) and analyzed by CasaXPS software. The surface is also cleaned by 30s Ar^+ sputtering under 10k eV.

To remove residual salt on the surface, all samples were slightly rinsed with DMC and dried in glovebox antechamber before analysis.

5.2.5 Computational methods

Molecular dynamics (MD) simulation were performed using APPLE&P polarizable force field[35,138]. The LiTFSI force field parameters from previous work were used.[138] The Li^+/THF and Li^+/FM parameters were developed in this work following previously described methodology by fitting to quantum chemistry (QC) data.[139] Partial charges were fit to reproduce electrostatic potential around the solvents and solvent/Li^+ complexes calculated using Møller–Plesset perturbation theory (MP2) with aug-cc-pvTz basis set. The dihedral parameters for THF were fit to reproduce molecular deformation energy that was also calculated at MP2/aug-cc-pvTz level. Binding energy for the $Li^+(FM)_4$ complex was 344 kJ/mol from molecular mechanics (MM) calculations using force field parameters, which is slightly lower than predictions from G4MP2 hybrid QC methodology of 353 kJ/mol. Binding energy of Li^+(THF) was 173 kJ/mol from both

MM calculations using developed force field and G4MP2 QC calculations indicating accurate description of the Li$^+$ binding to FM and THF by the developed force field.

MD simulation cells contained 64 LiTFSI, 64 THF and 2163 FM molecules corresponding to the experimentally investigated electrolyte composition for 0.5 M LiTFSI, 0.5 M THF in FM at room temperature. Two replicas were created by randomly removing 77 FM molecules from the equilibrated system comprised of 64 LiTFSI, 64 THF and 2240 FM that were simulated for 60-90 ns at -20, 0, and +20°C. Simulations were performed in constant volume – temperature (NVT) ensemble using Nose – Hover thermostat. Equilibration runs were 40-112 ns followed by 70-131 ns production runs as shown in Supporting Information for all simulated systems. Multiple timestep integration was employed with timestep of 0.5 fs for bonded interactions, time step of 1.5 fs for all non-bonded interactions within a truncation distance of 8.0 Å and an outer timestep of 3.0 fs for all non-bonded interactions between 8.0 Å and the nonbonded truncation distance of 18 Å. Due to high aggregation and non-homogeneous distribution of salt and solvent, a very large cut-off distance of 18 Å for dispersion and real space of electrostatic interactions was adopted. The Ewald summation method was used for the electrostatic interactions between permanent charges with permanent charges or induced dipole moments with $k = 7^3$ vectors. The reciprocal part of Ewald was calculated every 3.0 fs. Induced dipoles were found self-consistently with convergence criteria of 10^{-9} (electron charge * Å)^2. Additional simulation details and methodology used for calculation of transport properties is given in Supporting Information. The MD source code and input files are attached in a separate zip file.

5.3 Result and Discussion

5.3.1 Physical/chemical properties of liquefied gas electrolytes

While previous work focused on an electrolyte composition of 0.2 M bis(trifluoromethane)sulfonimide (LiTFSI) in FM[39], more recent optical observations using high-pressure glass window cells show that less than 0.1 M LiTFSI is soluble in pure FM (Figure 5.1A), so several possible methods were explored to increase the solubility of the salt. It was found that THF is miscible with FM and the addition of this cosolvent (2.4 vol%) with a salt-to-THF molar ratio of 1:1 increases the Li salt solubility considerably (Figure 5.1A). By controlling the 1:1 salt-to-additive molar ratio, THF is thought to be fully coordinated with Li cations, as illustrated in Figure 5.1B. Similar to high-concentration electrolyte systems, the fully coordinated THF solvation structure is expected to suppress the oxidation of this additive.[63,69,140]

Electrolytic conductivity measurements of the modified liquefied gas electrolytes were carried out. As detailed previously[39], the conductivity versus temperature curves of the liquefied gas electrolytes do not follow that of typical electrolytes. Due to the exceptionally low melting point of FM (T_m = -142°C), minimal viscosity (η = 0.085 mPa·s), and high dielectric-fluidity factor ($\varepsilon_r \cdot \eta^{-1}$ = 114 (mPa·s)$^{-1}$), the conductivity is well maintained at low temperatures. Notably, the conductivity is substantially enhanced with an increase in concentration of the salt and additive while the conductivity still follows the same temperature trends as the FM based electrolyte without the addition of THF. The electrolytic conductivity of the 0.5 M LiTFSI, 0.5 M THF in FM shows a maximum conductivity of 3.9 mS·cm^{-1} at +20°C. An impressive low-temperature conductivity of 2.8 mS·cm^{-1} is achieved at -60°C, which is substantially higher than the previously reported (1.1 mS·cm^{-1})[39] and compares favorably with some state-of-the-art low-temperature

electrolytes[110,141]. Due to the decreasing dielectric constant and precipitation of salt out of the electrolyte as the temperature approaches the critical point of FM ($T_{c, FM}$ = +44°C), the conductivity shows a sudden drop.[39] Similar electrolytic conductivity phenomena are observed with the introduction of THF (Figure 5.1C) which indicates that the salt still strongly aggregates at increased temperatures despite the improved solubility with the addition of THF. Strategies to enable an increased operating temperature at commercially acceptable temperatures has been demonstrated and will be published in future work.

In order to obtain further insight into the solvation structure and the lithium transport mechanisms of the modified liquefied gas electrolytes, molecular dynamics (MD) simulations were performed with the focus on the most conductive concentration of 0.5 M LiTFSI, 0.5 M THF in FM. Predicted conductivity from MD simulations agrees well with the experimental value as shown Figure 5.1C. A drop in conductivity as temperature increases to +40 ° C is attributed to the decrease of ionicity (degree of ion uncorrelated motion) to *ca.* 2 % as shown in Figure 5.1D. This is attributed to a drop in the fraction of free lithium ions below 0.5%. Further analysis of the ion solvation shell indicates that at all simulated temperatures there are no free TFSI⁻ ions are observed, while the fraction of free Li⁺ uncoordinated by TFSI⁻ anions increases approximately linearly with decreasing temperature. Snapshots from MD simulations Figure 5.1E-G) indicate that at +40°C most ions aggregate forming essentially one large cluster with an occasional free Li⁺ cation and a few smaller aggregates. Figure 5.1H quantitatively confirms that at +40°C most ions belong to large aggregate clusters with a peak at 90 ions out of 128 total number of ions in the simulation cell. The formation of smaller clusters and a subsequent increase in the fraction of free lithium ions is observed as temperature drops to +20°C and below, thus compensating for the slight decrease of ion self-diffusion coefficients shown in Supporting Information. This results in the

approximately constant conductivity over a wide temperature range from -20 to +20°C. Despite similar average self-diffusion coefficients for Li^+ and $TFSI^-$, the diffusion of the free Li^+ is 2-2.5 times faster than the average diffusion coefficients of all Li^+ and $TFSI^-$ anions as shown in Supporting Information. The much higher fraction of free Li^+ as compared to free $TFSI^-$ indicates a high contribution of Li^+ to the electrolytic conductivity compared to anion contribution that move slower and essentially do not exist as free ions. The lithium transference number (t_+) is calculated using the Onsager reciprocal relations combined with a linear response theory as yielding $t_+ > 0.95$, which is supported by the measured Li^+ transference number as high as $t_+ = 0.79$. High ionic correlations are responsible for the increased t_+ compared to the transport number based upon self-diffusion coefficients that is only 0.5 as shown in Supporting Information.

Analysis of the Li^+ solvates yields 0.98-1.02 THF, 2.09-2.22 TFSI anions and 0.4-0.67 CH_3F coordinating to each Li^+ on average. Interestingly, THF is not uniformly distributed among free Li^+ and Li^+ participating in aggregates. Free Li^+ tends to be primarily coordinated by 2, 3 or 4 THF molecules with 2, 1 or 0 FM, respectively, as shown in Supporting Information, with the $Li^+(THF)_3FM$ solvate being the most frequently observed. Thus, free Li^+ are surrounded preferentially by THF while the Li^+ participating in aggregates have fewer coordinating THF on average clarifying the role of THF in salt dissociation.
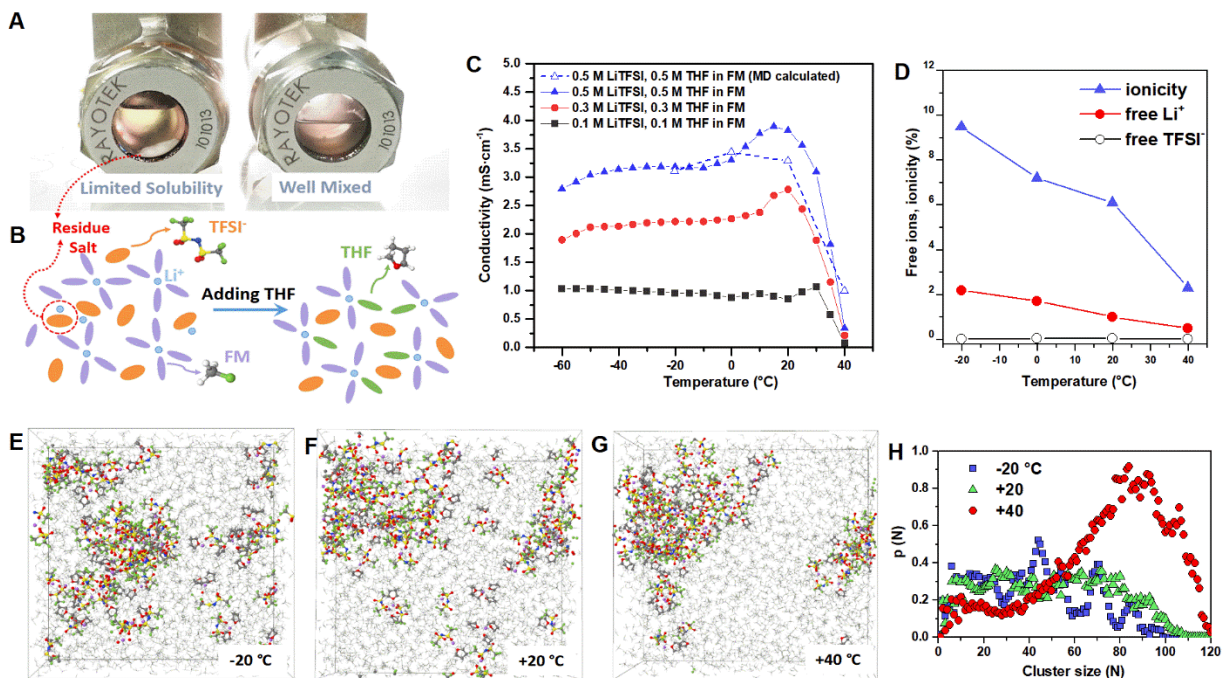
Figure 5.1. Properties of liquefied gas electrolytes (A) Photographs of solubility tests, (B) schematic of the solvation mechanism, (C) conductivity measurements, (D) calculated fraction of free ions, (E-H) snapshots of the MD simulation cell and the distribution probability.

5.3.2 Lithium metal cycling performance

The cycling and rate performances of Li metal plating/stripping in liquefied gas electrolytes were examined on polished stainless-steel electrodes. As discussed previously[39], the addition of 5 wt% CO_2 to the fluoromethane-based liquefied gas electrolyte helps stabilize the Li-metal anode and is similarly used in the present study. At a current density of 0.5 mA·cm^{-2}, an overpotential of 13 mV is observed, which is comparable to that of the carbonate-based electrolyte, 1M $LiPF_6$ in ethylene carbonate/diethyl carbonate (EC:DEC 1:1), and the ether-based electrolyte, 1M LiTFSI, 2 wt% $LiNO_3$ in 1,3-dioxolane/1,2-dimethoxyethane (DOL:DME 1:1), and improved from a similar liquefied gas electrolyte without the THF additive (Figure 5.2A). Liquefied gas electrolytes

with THF additives significantly improved the Li metal cycling stability and CE. All CE efficiencies reported have an uncertainty of $\pm$ 0.3%, as described in the method's section. As shown in Figure 5.2B, at 0.5 mA·cm^{-2}, the CE ramps up from an initial value of 93.6% to an average CE of 98.6% during the first 100 cycles. An impressive average CE of 99.9% is achieved from the 100th to 500th cycle, demonstrating an overall average CE of 99.6% ($\pm$ 0.3%) over all 500 cycles. It is thought that a stable interface is formed during the first *ca.* 100 cycles, after which more stable cycling is observed via the increase in CE. CE slightly above 100% is observed regularly. It is hypothesized that a small portion of electrically disconnected metallic Li formed within the SEI of previous cycles electrically reconnects to the metallic bulk structure in a future cycle which accounts for the CE occasionally being over 100. This is likely due to the breaking of a relatively brittle SEI layer by temperature and volume change during cycling. A similar phenomenon has also been observed in other dendrite-free electrolytes.[74,137] The voltage profile also remains stable with a slight increase in overpotential (Figure 5.2C). For comparison, carbonate-based and ether-based electrolytes demonstrate unstable CE with averages of *ca.* 85% and 95%, respectively (Figure 5.2B). At an increased Li cycling capacity of 1 mAh·cm^{-2} at the same current density, the CE in the liquefied gas electrolyte remains at 99.4% for 200 cycles with less CE fluctuation after 20 initial activation cycles. At an increased current density and capacity of 1 mA·cm^{-2} and of 1 mAh·cm^{-2} respectively, an average CE of 98.7% is achieved after initial activation from cycles 100 - 900 with a similarly stable overpotential throughout cycling (Supporting Information). The electrochemical performance of the liquefied gas electrolyte is also impressive at high rates up to 10 mA·cm^{-2} with a stable voltage profile (Figure 5.2D). The polarization of the liquefied gas electrolyte increases nearly linearly and symmetrically with the current density, reaching 100 mV at 10 mA·cm^{-2} (Figure 5.2D-E). The nearly linear polarization

is indicative of the highly ionically conducting Li metal SEI layer and high ion diffusion through the electrolyte. Combined with the high CE, this high rate performance is substantially superior in comparison to the carbonate-based electrolyte, ether-based electrolyte , all-fluorinated electrolyte[74], high concentration electrolyte[137] and localized high concentration electrolyte systems[36] (Figure 5.3).
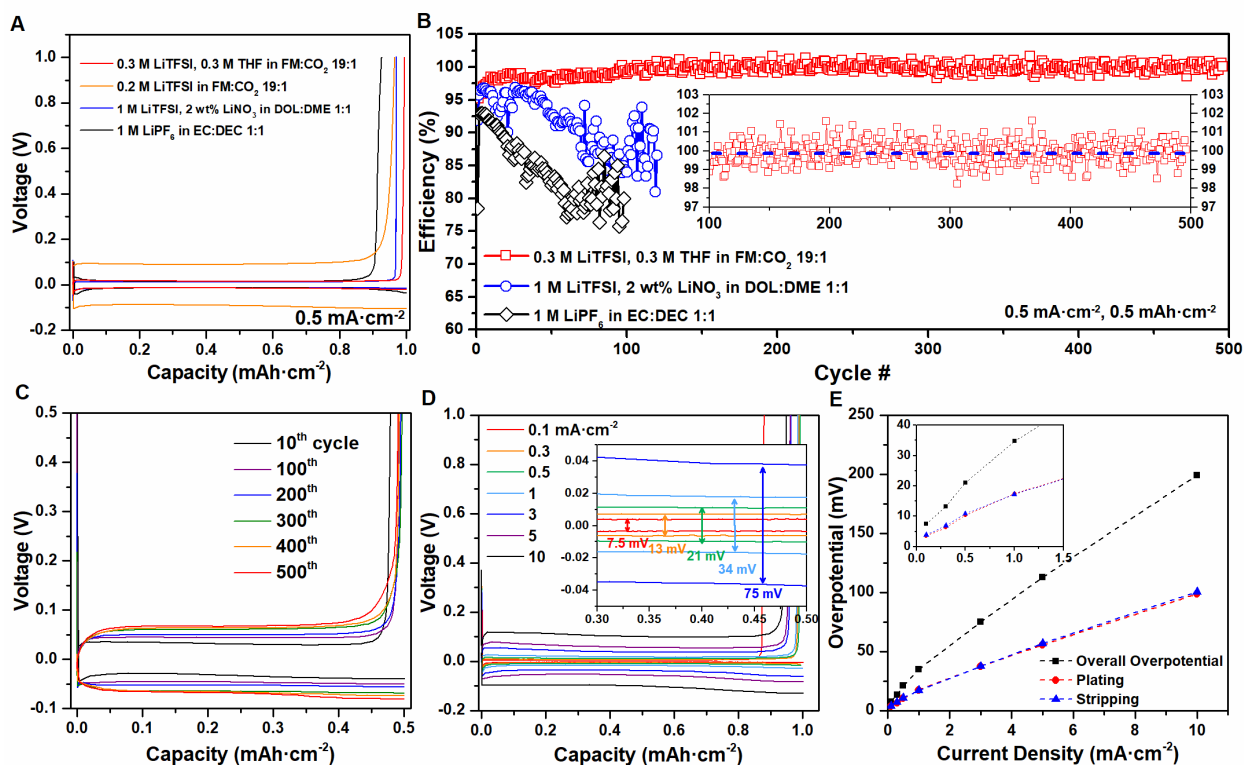
Figure 5.2. Electrochemical performance of Li metal anode (A) Voltage profiles of the 20th cycle, (B) the CE over 500 cycles, (C) voltage profiles for the cell using the liquefied gas electrolyte used in (B). Polarization profiles (D) and quantitative summary (E) for Li plating/stripping at various current densities.
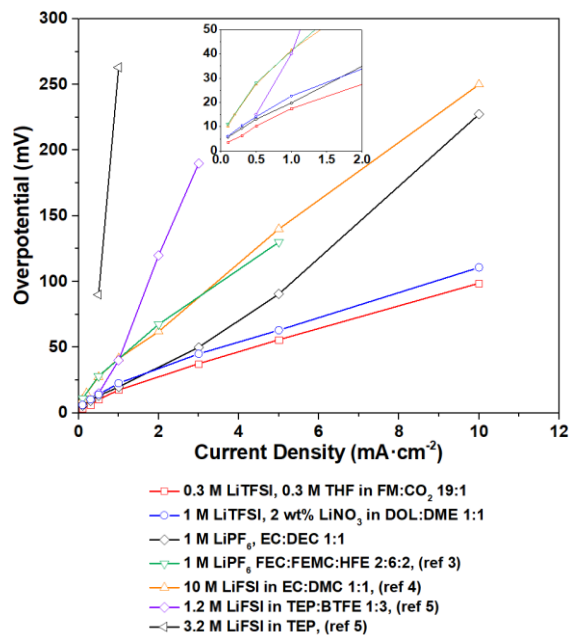
Figure 5.3. Polarization summary of Li metal plating and stripping in different electrolytes3-5 at various current densities.

In order to ascertain the commercial viability of the use of these electrolytes, we also demonstrate successful cycling of an LTO/NCA jelly-roll (0.8 Ah, 1.3 V-2.7 V, 4.2 V vs Li) in a conventional 18650 form factor with a custom cell cap to enable liquefied gas electrolyte injection and solvent containment under pressurized conditions (Figure 5.4). Although manufacturing challenges remain, the demonstration of a conventional 18650 form-factor to safely contain the electrolyte under pressurized conditions reduces barriers to commercialize practical devices.

70
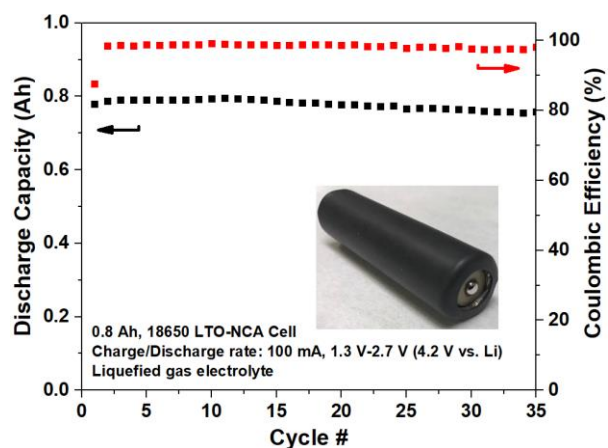
Figure 5.4. Demonstration of an LTO-NCA Jelly Roll in an 18650 cell format with the liquefied gas electrolyte.

5.3.3 Low-temperature performance

The low-temperature operation is a large challenge for lithium ion batteries, resulting from a reduced electrolytic conductivity, an increase in SEI impedance, and a limited Li ion diffusivity within the electrodes.[128] Contrary to intercalated anodes, such as graphite[142], the hostless feature of the Li metal anode removes the necessity for long distance charge transfer in the host which is a substantial benefit of the Li metal anode for low-temperature applications. Due to the unique nature of liquefied gas electrolytes, the low melting point and high dielectric-fluidity factors enable excellent conductivity down to -60°C. Therefore, the low-temperature performance of the Li metal anode with the liquefied gas electrolyte was further explored.

Extended cycling of Li metal at various temperatures was compared in liquified gas electrolyte, carbonate-based and ether-based electrolyte systems (Figure 5.5A). At +20 °C, the CE of the carbonate-based electrolyte is limited to *ca.* 90% and at -20°C shows a continuous drop in CE (*ca.* 78%) with a considerable increase in overpotential. The cell fails to cycle at lower

71

temperatures and shows reduced performance when warmed to room temperature (Figure 5.5B). In the ether-based electrolyte, the CE fading at low temperature is even worse and the cell fails to cycle when warmed back to room temperature. In contrast, the CE of the liquified gas electrolyte increases to 99.5% within 20 cycles at +20°C, and an average CE of 98.6% with stable polarization is observed at -20°C. The cell cycles equally well at lower temperatures, demonstrating a stable CE of 98.4% at -60°C with an average overpotential of 0.28 V. When brought back to +20 °C, the voltage profile of the cell perfectly matches that of the initial state, with a CE marginally higher than 100%, indicating recovery of dead Li formed at lower temperatures, which is likely due to the restructuring and volume expansion of the surface layer during the temperature increase.

The voltage profiles for Li metal rate tests at various temperatures are shown for both the liquefied gas electrolyte (Figure 5.5C) and the carbonate-based electrolyte (Supporting information). The liquefied gas electrolyte demonstrates highly stable Li metal cycling with remarkable capacity retention down to -40°C at 10 mA·cm^{-2} and even down to -60°C at 5 mA·cm^{-2} (Figure 5.5C), while the overpotential increases irregularly for 10 mA·cm^{-2} cycling at -60°C. As summarized in Figure 5.5D, the polarization linearly increases with current at temperatures down to -40°C, which suggests the impedance is dominated by ohmic resistance and the electrolyte is not diffusion limited even at such low temperatures. The carbonate-based electrolyte in contrast is only stable at low platting/stripping currents (< 0.5 mA·cm^{-2}) and shows unstable cycling with a substantial increase in overpotential at higher current densities at -20°C (Supporting Information). Estimated from Tafel plots the exchange current densities show the fast kinetics of the liquefied gas electrolyte and its interfaces at different temperatures, which are 1.4, 6.5, and 14.9 times higher than that of carbonate-based electrolyte at +20, 0, and -20°C, respectively.
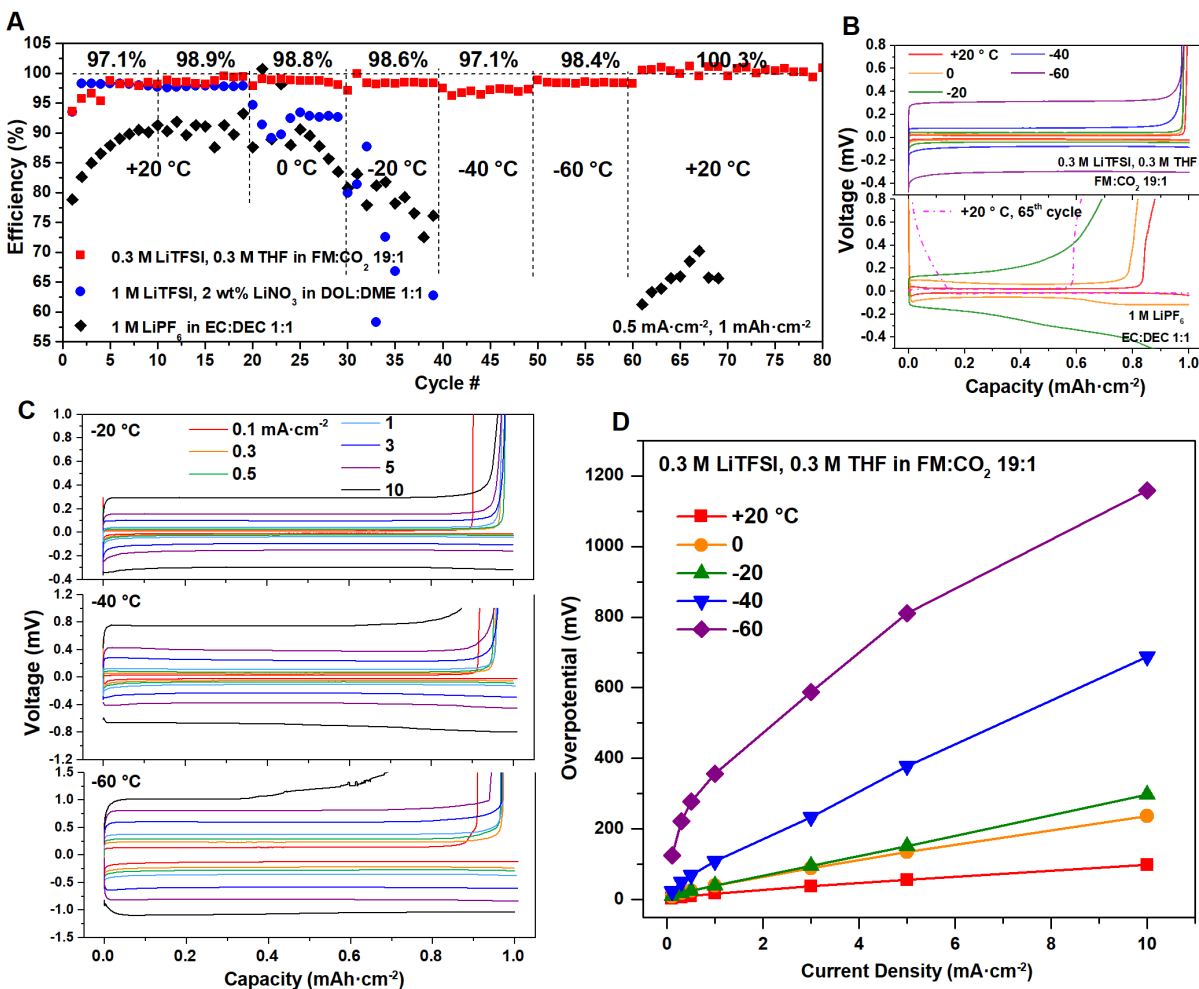
Figure 5.5. Li metal low-temperature performance (A) The CE at various temperatures, (B) voltage profiles for the cells cycled in (A), (C) Li metal plating/stripping voltage profiles at various currents and temperatures, (D) average overpotential summary of the liquefied gas electrolyte.

5.3.4 Li metal morphology

The surface and cross-sectional morphology of Li metal deposition in the liquefied gas electrolyte was observed via scanning electron microscopic (SEM) and cryogenic focused ion beam (cryo-FIB). Cryogenic techniques have proven useful for preserving and probing morphological and chemical phenomena of Li metal and recently cryo-FIB has been demonstrated

to quantitatively characterize bulk morphology of electrochemically deposited Li and enable transmission electron microscopy (TEM) analysis of Li-metal/electrolyte interfaces.[22,45–47] Li metal is extremely reactive at room temperature because of its low melting temperature, density, thermal conductivity, and shear modulus, making samples prone to deleterious cascade effects and Ga-ion implantation during FIB milling resulting in morphological and chemical artifacts. To overcome this challenge, cryo-FIB was applied to minimize damage when preparing Li cross-sections for SEM imaging and 3D reconstruction to explore the bulk microstructure of the deposited Li metal (Figure 5.6A). Samples were plated with a capacity of 1 mAh·cm^{-2} at 0.5 mA·cm^{-2} on a stainless-steel electrode, which corresponds to a theoretical thickness of ~5 µm for perfectly dense Li.

As shown in Figure 5.6B, the Li deposited in carbonate-based electrolyte generates needle-like dendrites with numerous pores. The cross-sectional observations reveal the Li metal film having a porous structure and large voids present at both the Li/substrate interface and the bulk structure of the deposited Li, resulting in a total thickness of >10 µm (Figure 5.6C). The 3D reconstructed model of deposited Li metal in the carbonate-based electrolyte illustrates that large void spaces (16.8%) are present through the entire bulk and the interface (Figure 5.6D), causing a large normalized void surface area of 1.32 µm^{-1} (Table 5.1). The ether-based electrolyte enables a dendrite-free Li deposition with roundly shaped Li particles (Figure 5.6E). However, the cross-sectional view shows that large voids are generated on the Li/substrate interface (Figure 5.6F), which is further elucidated in the 3D reconstruction which shows a relatively large porosity of 8.2% (Figure 5.6G). In contrast, the liquefied gas electrolyte presents densely packed, large, roundly shaped Li particles forming a smooth dendrite-free surface (Figure 5.6H). From the cross-sectional view, the liquefied gas electrolyte forms a very dense Li deposition with a thickness of 5.3 µm

(Figure 5.6I). At an increased 3 mAh·cm^{-2} capacity of deposited Li, the compact bulk structure is well maintained with a thickness of 15.5 µm (Supporting Information). The 3D reconstructed model of deposited Li metal in the liquefied gas electrolyte shows much denser deposition with minimal porosity (0.90%) and normalized void surface area (0.096 µm^{-1}) (Figure 5.6J). The deposited Li metal morphology after 20 cycles for all tested electrolyte is consistent with the initial plating (Supporting Information). Additionally, the large particle size and compacted morphology in the liquefied gas electrolyte is maintained even after 100 cycles (Supporting Information). On the stripping side, the liquefied gas electrolyte enables a thinner and denser layer of sheet-like residue, revealing minimal formation of dead Li. In summary, unlike the dendrite formation in the carbonate-based electrolyte or the large voids at Li/substrate in the ether-based electrolyte, the liquefied gas electrolyte shows a densely packed deposition of Li which allows for excellent structural connection with low porosity, increasing the CE, limiting the volume change, and limiting the increase in polarization during long-term cycling.
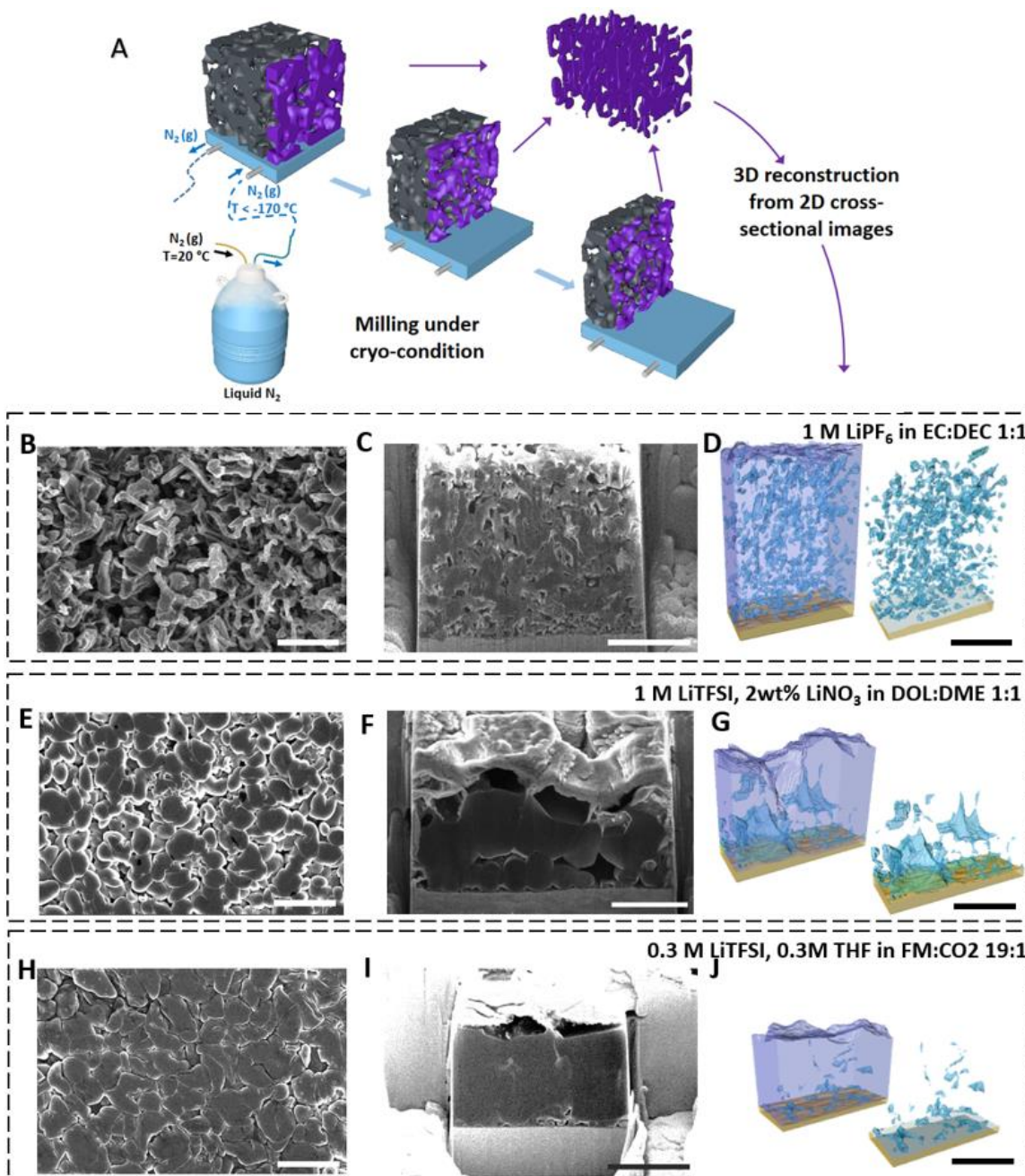
Figure 5.6. Cryo-FIB characterization of the morphologies of electrochemically deposited Li and its 3D reconstruction

Table 5.1. Physical properties of the bulk structure of plated Li in different electrolytes.

Electrolyte	1 M LiPF$_6$ in EC/DEC	1 M LiTFSI, 2wt% LiNO$_3$ in DOL/DME	0.3 M LiTFSI, 0.3M THF in FM:CO$_2$ 19:1
Ideal Thickness (μm)	5	5	5
Real Thickness (μm)	10.1	5.5	5.3
Particle Shape	Needle like	Grain like	Grain like
Particle Size	~100 nm	1 - 7 μm	3 - 7 μm
Porosity (%)	16.8	8.2	0.90
Normalized Void Surface Area (μm^{-1})	1.32	0.82	0.096
1st Cycle CE (%)	86.7	91.9	93.6

5.3.5 Chemistry at the interphase

The impedance of the electrolyte and the Li metal SEI layer at various temperatures were investigated by electrochemical impedance spectroscopy (EIS, Figure 5.7A-C). The x-axis intercept in the high-frequency region corresponds to the bulk electrolyte resistance R_e, and the following semicircle is assigned to the interfacial resistance ($R_{int} = R_{int1}+R_{int2}$) from the electrodes. In both carbonate and ether-based electrolytes, R_e exhibits a 5x enlargement when the temperature is reduced to -40°C while the liquefied gas electrolyte shows good low temperature compatibility with only a 20% increase in R_e down to -60°C (Figure 5.7C), which is in the agreement with the previous electrolyte conductivity measurements. Nevertheless, it is known the SEI often contributes to a higher impedance compared to that of the electrolyte at low temperatures.[128] As summarized in Figure 5.7C, the SEI layer is the dominant component of the impedance in all these systems as temperature increases. At all measured temperatures, the R_{int} of the liquefied gas electrolyte is roughly an order magnitude less than that of the carbonate and ether-based electrolyte,

which indicates that a dense and highly ionically conductive SEI is present in the liquefied gas electrolyte system.

Insights into the composition and formation mechanism of the SEI in liquefied gas electrolytes can be obtained from the X-ray photoelectron spectroscopy (XPS) on the cycled Li metal electrode (Figure 5.7D). The differences in the SEI components and formation mechanisms between conventional liquid electrolytes and liquefied gas electrolytes are pronounced. For the carbonate-based electrolyte (Fig. 5d(i), 1 M $LiPF_6$ in EC:DEC 1:1), the SEI formed is dominated by Li alkyl carbonates ($ROCO_2Li$) with a heterogeneous distribution of inorganic LiF from $LiPF_6$ decomposition. This results in a poorly ionically conducting and unstable SEI.[14,15] The ether-based electrolyte (Fig. 5d(ii), 1 M LiTFSI, 2wt% $LiNO_3$ in DOL:DME 1:1) is able to partially passivate Li metal surface by forming mainly inorganic components like Li formate (HCO_2Li), and organic species like $-(CH_2CH_2O)_n-$ and short chain oligomers with -OLi edge groups (ROLi)[15,143]. The relatively small S 2p and N 1s spectra (Supporting Information) confirm that the low fluorine concentration in the SEI (Figure 5.7D, F 1s) is caused by the limited decomposition of LiTFSI. In contrast, a highly fluorinated ceramic-like SEI is formed in the liquefied gas electrolyte without addition of THF (Fig. 5d(iii), 0.2 M LiTFSI in FM:CO_2 19:1). Although the LiTFSI decomposition is still limited (S 2p, N 1s), the main components of the solvent, fluoromethane and carbon dioxide, reduce to LiF and Li_2CO_3 respectively, components which previous computational studies have shown combine synergistically to enhance ionic conductivity[144]. Importantly, there is no notable change in the SEI chemical composition with, (Fig. 5d(iv)) and without, (Fig. 5d(iii)) the addition of THF for all spectra. Together with no obvious change in C-O band (Figure 5.7D-E), it indicates that there is little to no decomposition of THF. There is a slight increase in the S 2p and N 1s spectra, suggesting a larger (but still small) amount of LiTFSI may be involved in the SEI

formation due to improved solubility. It is also supported by the enlargement of the ratio of LiF, which may contribute to improve the ionic conductivity of the SEI layer (Figure 5.7E).[137,145] In agreement with previous studies showing benefits of a highly fluorinated interface[78], both the fluoromethane solvent and salt in the present study are rich sources of fluorine and contribute to the large presence of LiF in the SEI. The additional Li_2CO_3 component found in the Li metal SEI from carbon dioxide reduction is thought to combine with the LiF to provide an overall positive impact on the overall electrochemical performance.[144]
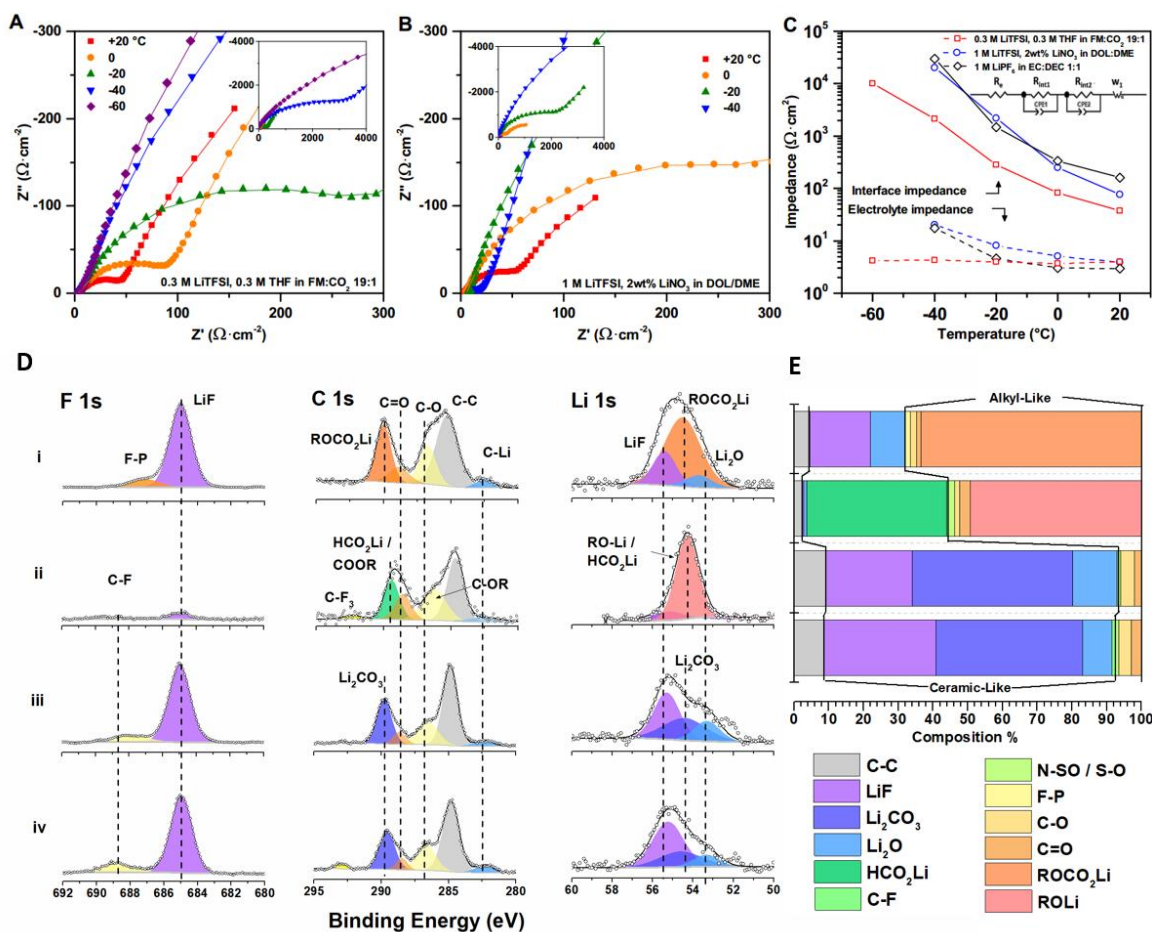
Figure 5.7. Impedance and chemical characterization of lithium metal interface. (A-C) Electrochemical impedance spectra of different electrolyte and their fitting analysis. (D and E) XPS chemical analysis (D) of the lithium metal interface using different electrolytes.

5.4 Conclusion

Combining superior physical and chemical properties, liquefied gas electrolytes have high compatibility with the Li metal anode, showing excellent CE at high rates and over a wide temperature range. The introduction of THF as a co-solvent, which coordinates with the Li cations, increases salt dissociation and transport, ionic conductivity and addresses the solubility and polarization issues previously seen with the liquefied gas electrolytes. The use of the fluoromethane-based liquefied gas electrolyte yields a dense and uniform Li metal deposition and stable and dendrite-free Li metal cycling with a high average CE over 500 cycles of 99.6%, with remarkable rate performance up to 10 mA·cm^{-2}. The Li metal cycling and rate performance is well maintained down to -60°C due to the high dielectric-fluidity factor and exceptional electrolytic conductivity at low temperatures with a low-impedance SEI. Combining dendrite-free cyclability at high rates and over a wide temperature range, as well as demonstration of the compatibility of the electrolyte with conventional form factors, the liquefied gas electrolyte chemistry provides a promising path towards high-energy Li metal chemistries.

This chapter in full, is a reprint of the material "High-Efficiency Lithium-Metal Anode Enabled by Liquefied Gas Electrolytes" as it appears in Joule, Yang, Y.; Davies, M. D.; Yin, Y.; Borodin, Oleg.; Lee, J. Z.; Fang, C.; Olguin, M.; Zhang, Y.; Sablina, E. S.; Wang, X.; Rustomji, C. S.; Meng, Y. S., 2019, 3(8), 1986. The dissertation author was the primary investigator and first author of the paper. All of the tests were performed and analyzed by the author except for the molecular dynamics simulation.

Chapter 6. Liquefied Gas Electrolytes for Wide-Temperature Lithium Metal Batteries

6.1 Introduction

Increasing adoption of EV, UAVs and portable electronics leads to increasing demand to lithium-ion batteries operating over wide temperature range.[18,135] To further boost energy density and reduce cost, researchers revisited lithium metal batteries (LMBs) because of the highest achievable gravimetric energy density of lithium metal.[3,4] However, among the several challenges limiting the applications of LMBs is the development of an electrolyte that is stable with both the Li-metal anode and high-voltage cathodes in a wide temperature range (-60 to +55°C).[16,17]

Extensive efforts have been devoted to improving the electrolyte formulations to make them compatible with more aggressive higher energy density anode-cathode couples.[7,20,31,146] Commercialized ethylene carbonate (EC)-based electrolytes have moderate oxidation stability (~4.3 versus Li) for cathode operation. However, EC-based electrolytes have issues of dendrite formation and low Coulombic efficiency (CE) with Li-metal anode, along with a narrow operational temperature range, only down to -20°C due to high melting point of EC of 35°C.[7] Ether-based electrolytes show improved compatibility with the Li-metal anode and low-temperature performance due to the formation of a relatively favorable SEI and the lower melting point. Yet, the low oxidation stability (<4.0 versus Li) prevents its potential applications.[15] In recent years, high-concentration electrolytes have been shown to be able to stabilize Li-metal anode and cathodes by reducing the amount of free solvent.[61,63] However, these high concentration electrolytes sacrifice cost, viscosity, wetting, and low-temperature operation. Localized high-concentration electrolytes were developed by diluting electrolytes with different non-solvating

solvents, which presented more balanced properties.[71,73] For example, the use of fluorinated non-polar diluents in concentrated fluorinated electrolytes with an optimized ratio demonstrated stable interfaces with Li-metal batteries and impressive low-temperature performance down to -85°C.[70,74] Nevertheless, the low-temperature conductivity was quite low (0.011 mS·cm^{-1} at -80°C) and the reported cells were charged at room temperature and only discharged at low temperatures. Also, the Li-metal anode's low-temperature performances, such as deposition morphology, CE, have not been verified separately.[70] At the same time, nitrile-based electrolytes regained attention: Acetonitrile's (AN) stability with Li-metal anode has been improved by increasing the salt concentration, limiting the free AN molecules.[62,147] AN and other nitrile-based solvents were also used as cosolvents to improve the stability and the low-temperature performance of both aqueous electrolytes[65] and non-aqueous electrolytes[148]. Additionally, recent studies[149–151] have shown that the solvation of Li ion has significant impact on the properties of the electrolyte and interface formation. Understanding and formulating the solvation structure of electrolyte are the key for developing next-generation electrolyte.

The recently developed fluoromethane (CH$_3$F, FM)-based liquefied gas electrolytes demonstrated an impressive low-temperature operation down to -60°C and good stability with both a Li-metal anode and a 4 V class cathode.[39] This can be attributed to its unique physical and chemical properties, including low melting point, low viscosity and ability to form F-rich SEI/CEI. The electrolyte system was further enhanced by the introduction of tetrahydrofuran (THF) as a cosolvent to improve the salt solubility and the conductivity.[38] The unique solvation structure presented an impressive Li-metal efficiency at both room temperature (99.6%) and low temperature (98.5% at -60°C) using a current density of 0.5 mA·cm^{-2} and 1 mAh·cm^{-2}. Interestingly, a sudden drop in conductivity was observed when the temperature reached FM's

critical point ($T_{c, FM}$ = +44°C). This phenomenon has been identified as a potential reversible battery shut-down mechanism, yet this shutdown temperature is relatively low for many applications. Additionally, although the THF cosolvent is fully coordinated with Li salt, it still limits the further improvement of the oxidation stability.

Herein, we rational formulated liquefied gas electrolytes using AN as a cosolvent and enabled a higher, yet practical salt concentration of 1.2 M bis(trifluoromethane)sulfonimide (LiTFSI) for high-voltage Li-metal batteries in a wide temperature range. The electrolyte shows impressive ionic conductivity in wide temperatures ranging from -78 to +75°C. The new solvation structure expanded the liquefied gas electrolyte's high-temperature range beyond FM's critical point for the first time. This work also demonstrates the use of liquefied gas electrolyte for stable cycling of both Li-metal anode and 4.5 V Li-metal batteries in temperatures extending from -60 to + 55°C.

6.2 Experimental section

6.2.1 Materials

The salts Lithium bis(fluorosulfonyl)imide (LiFSI) (99.9%) and lithium bis(trifluoromethane)sulfonimide (LiTFSI) (99.9%) were obtained from BASF. Fluoromethane (99.99%) was purchased from commercial sources. 1.2 M $LiPF_6$ in EC/EMC 3:7 was purchased from BASF. Acetonitrile (AN, anhydrous, 99.8%), 1,2-dimethoxyethane (DME, 99.5%), and 1,3-dioxolane (DOL, 99.8%) were purchased from Sigma-Aldrich and stored over molecular sieves. The NMC622 (A-C023) was obtained from Argonne national laboratory.

6.2.2 Electrochemical measurements

Electrolytic conductivity measurements were performed in custom fabricated high-pressure stainless-steel coin cells, using polished stainless-steel (SS 316L) as both electrodes. The cell constant was calibrated from 0.447 to 80 mS·cm^{-1} by using OAKTON standard conductivity solutions.

The Li$^+$ transference number is measured by the potentiostatic polarization method with an applied voltage of 10 mV. Electrochemical impedance spectroscopy was collected by a Biologic SAS (SP-200) system and the spectra were then fitted using ZView software.

Battery cycling test was performed by an Arbin battery test station (BT2043, Arbin Instruments, USA) in custom designed high-pressure stainless-steel coin cells, with Li metal (FMC Lithium, 1 mm thickness, ¼ inch diameter) as the counter electrode and a polished SS316L as the working electrode. A single 25µm porous polypropylene separator (Celgard 2075) was applied for all the electrochemical experiments.

For Li metal plating and stripping experiments, lithium was first deposited onto the working electrode at 0.5 mA·cm^{-2} until 0 V vs. Li and the voltage was held for 5 hours to form a stable SEI on the current collector. The first plating cycle was then started, followed by complete lithium stripping to a 1 V vs. Li cut off voltage. The CE was calculated as the Li stripping capacity divided by the Li plating capacity during a single cycle. For the test in different temperatures, the cells were soaked at the testing temperature in a temperature chamber (Espec) for several hours before cycling. In Li-NMC cycling, the cell was firstly cycled at C/10 rate at room temperature for 2 activation cycles and then cycled at selected rate and temperature.

6.2.3 Electrolyte addition

The liquefied gas electrolyte of 1.2 M LiTFSI, 1M AN in $FM:CO_2$ 19:1 is labeled as 1.2 M LiTFSI-AN-FM. 1 M AN cosolvent is around 5% in volume. As similarly used in the previous study[39], addition of 5 wt% CO_2 is added to helps stabilize the Li-metal anode. Electrolyte addition procedures have been described previously.[39]

6.2.4 Material characterization

Raman spectra of liquefied gas electrolytes were carried on Renishaw inVia confocal Raman microscope with an excitation wavelength of 532 nm. All spectra were calibrated with Si (520 nm) and analyzed by Wire 3.4 software developed by Renishaw Ltd.

Cryogenic focused ion beam (Cryo-FIB) (FEI Scios DualBeam equipped with a CryoMat integrated cryo-stage and air-free quick loader) was applied to explore the morphology of the cross-section of electrochemically deposited Li. To minimize the beam damage during FIB operation, the samples are cooled down to -170°C under continuous chilled nitrogen gas cooling at high vacuum ($\sim 10^{-6}$ mbar). The cross-sections were firstly rough milled with a cross-sectional cut (30 kV, 5 nA) followed by a cross-sectional cleaning cut (30 kV, 0.5 nA).

X-Ray photoelectron spectroscopy (XPS) was performed using a Kratos AXIS Supra DLD XPS with monochromatized Al Kα radiation ($\lambda = 0.83$ nm and $h\upsilon = 1486.7$ eV) under a base pressure $<10^{-8}$ Pa. To avoid moisture and air exposure, samples were transferred to the XPS chamber directly from a glovebox via vacuum transfer. All spectra were calibrated with hydrocarbon C 1s (284.6 eV) and analyzed by CasaXPS software. To remove residual salt on the surface, all samples were slightly rinsed with DMC and dried in glovebox antechamber before analysis.

Cryo-(S)TEM: After cycling, all cells were disassembled in an argon-filled glove box. The cathode was scraped off from current collector and dispersed in DMC solvent with the help of sonication. The obtained suspension containing dispersed particles were dropped on TEM lacey carbon grid which was then thoroughly dried under vacuum to remove residue DMC solvent. The loading and transferring the grid to TEM were carefully controlled to prevent sample from air exposure and detail information can be found in our previous publication.[64] HRTEM was recorded on a field emission gun JEOL-2800 at 200 kV with Gatan OneView Camera (full 4 K x 4 K resolution). STEM-EDS was performed on primary particles a at annular dark field (ADF) mode using the same microscope. All ADF images were acquired at 200 kV with a beam size of $\approx$5 Å. Note that both HRTEM and STEM-EDS were carried out under cryogenic temperature (~180 °C) to minimize beam damage on CEI structure/chemistry.

6.2.5 Computational methods

MD simulation cell contained 2000 FM, 120 AN and 144 LiTFSI. A polarizable force field APPLE&P was used[138] with the previously developed LiTFSI, FM and AN parameters[38,65]. The length of equilibration and production runs, simulation temperatures and predicted parameters are summarized in Table S1. The experimental density estimation was difficult at higher temperatures (+40 and +60°C) due to the changes of liquid phase volume and composition ratios, therefore, compressed states with densities at lower temperatures were applied to interpret high-temperature cases (Table S1). The equations of motions were solved with a time reversible (RESPA) integrator over the following time resolutions: i) the contribution from bonds and angles to the forces were calculated at any 0.5 femtosecond (fs), ii) the contribution of dihedrals and non-bonded forces within 8 Å cut-off were updated at any 1.5 fs, and iii) the remainder of the forces (reciprocal space Ewald and non-bonded forces within 14 or 16 Å cut-off were updated at any 3fs. Nose-Hoover

thermostat was used for temperature control. An archive containing all input files needed to perform bulk MD simulations is included in Supporting Information. The Li^+ cation transference number (t_+) was extracted from MD simulations following formalism suggested by Wohde *et al.*[152] using decomposition of the full charge displacement matrix into the contributions from cation-cation, cation-anion and anion-anion denoted as κ_{++}, κ_{+-} and κ_{--}. Note that κ_{+-} is defined using the opposite sign from Wohde et al.[152] The transference number ($t+$) is defined using two parameters α, β (see Table S1)

$$\alpha=\kappa_{++}/(\kappa_{++} + \kappa_{--}) \text{ and } \beta=-2 \ \kappa_{+-}/(\kappa_{++} + \kappa_{--}) \tag{S1}$$

$$\kappa= \kappa_{++}+ \kappa_{++} + 2 \ \kappa_{+-} \tag{S2}$$

$$t_+=(\beta^2 - 4\alpha+ 4\alpha^2)/(4(1-\alpha)(\beta-1)) \tag{S3}$$

Parameter α is similar to the transport number determined using self-diffusion coefficients. Parameter β is 0.92-0.98 indicates strong ion correlations to t_+.

6.3 Results and discussion

6.3.1 Ion Transport and Solvation of the Electrolytes

AN was selected as a cosolvent for FM solvent due to its high dielectric constant, low viscosity, and good oxidation stability.[62] Solubility tests were first performed with a salt-to-cosolvent molar ratio close to 1:1 to ensure LiTFSI is fully dissolved. The high-pressure window cell clearly shows there is no phase separation of the LiTFSI-AN-FM mixture up to 1.2 M LiTFSI, 1 M AN in FM (Figure 6.1A). With this high salt-to-cosolvent ratio (1.2:1), AN is thought to be fully coordinated with Li cations (Figure 6.1B) and is expected to improve its stability with Li metal anode at the same time.[62] FM is also expected to partially coordinated with Li cations due

to its relatively lower affinity. The solvation structure model is proposed in Figure 6.1B and will be further discussed in later sections.

Electrolytic conductivity measurements of the liquefied gas electrolytes at different salt concentrations were performed (Figure 6.1C). Similar to previous observations[38,39], the conductivity at low salt and cosolvent concentration is well maintained at low temperatures down to -60°C. But as demonstrated by observations from window cells (Supporting information), when temperature closes to FM's critical point ($T_{c, FM}$ = +44°C), the most of FM goes to supercritical state and little liquid is left. Although the liquid left is still a mixture of LiTFSI-AN-FM and should have conductivity, it's impracticable for conductivity measurement and cell cycling. Notably, at higher salt and cosolvent concentrations of 1.2 M LiTFSI and 1 M AN, a substantially different conductivity curve is observed. The electrolytic conductivity of 1.2 M LiTFSI, 1 M AN in FM shows a conductivity of 9.0 mS·cm^{-1} at +20°C, which is comparable to most conventional liquid electrolytes. FM and AN's low viscosity (η_{FM} = 0.085 mPa·s, η_{AN} = 0.37 mPa·s) and low melting point ($T_{m, FM}$ = -142°C, $T_{m, AN}$ = -44°C), coupled with the higher salt concentration enables an impressive low-temperature electrolytic conductivity of 5.8 mS·cm^{-1} at -60°C and 4.8 mS·cm^{-1} at -78°C. These low-temperature conductivity values compare favorably with most known electrolytes, including previously reported liquefied gas electrolyte (3.9 mS·cm^{-1}, -60°C)[38], ethyl acetate-based electrolytes (0.2 and 0.6 mS·cm^{-1}, -70°C)[141,153], and fluorinated localized high concentration electrolyte based on the carbonate solvent (0.044 mS·cm^{-1}, -70°C)[70] and AN solvent (Figure 6.1C). Furthermore, the conductivity is still well maintained at high-temperatures up to +75°C (5.7 mS·cm^{-1}), which is sufficient for most high-temperature applications. The wider temperature range is thought to be related to increasing the amount of salt and cosolvent, which may reduce volume change and maintain increasing amount of FM in LiTFSI-AN-FM mixture,

allowing operation above FM's critical point. The internal pressure above the critical point is also expected to be reduced by the extra amount of cosolvent and salt. Additionally, in a separate study, strategies to further decrease the operating pressure have been demonstrated and will be published in future work.
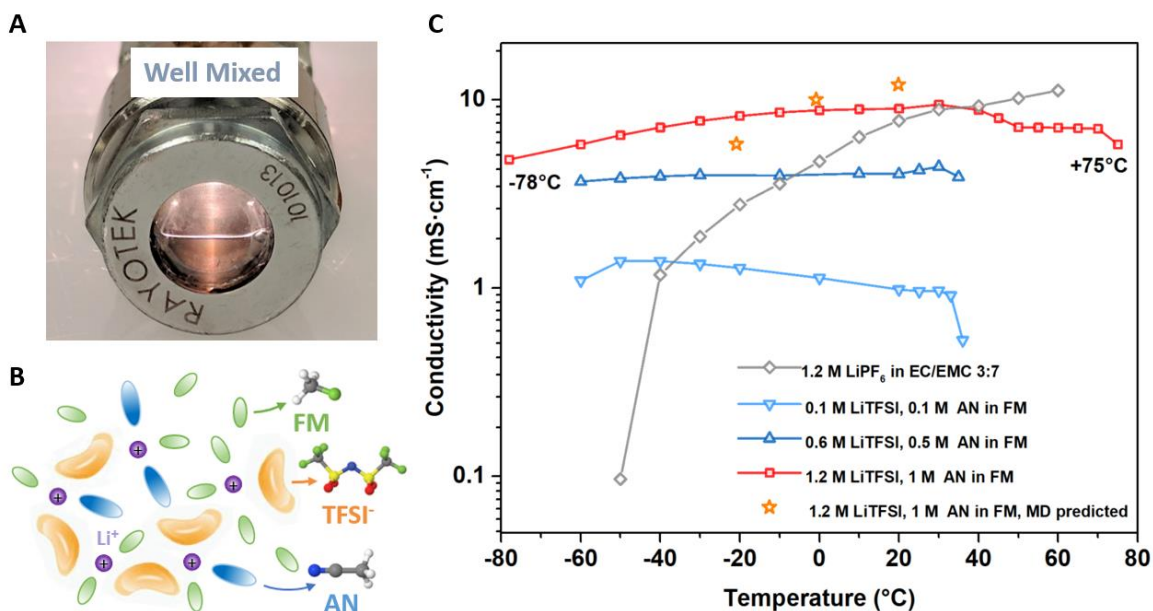
Figure 6.1. Design and conductivity of liquefied gas electrolytes. (A) Solubility test of 1.2 M LiTFSI, 1 M AN in FM. (B) Schematic illustration of the solvation mechanism of liquefied gas electrolyte. (C) Electrolytic conductivity measurements.

The solvation structure of the liquefied gas electrolyte was investigated and verified via Raman spectroscopy and molecular dynamics (MD) simulations. To identify the coordination of Li^+ with AN and FM molecules, Raman spectra were obtained for the 1 M AN co-solvent in FM at various LiTFSI concentrations (0 M to 1.2 M) (Figure 6.2A-C). As shown in Figure 6.2A, the peak of C≡N is located at 2252 cm^{-1}, derived from the pure AN solvent. By increasing the amount of salt, the normalized intensity of the peak at 2252 cm^{-1} gradually decreases, whereas a different peak at 2270 cm^{-1} arises (Figure 6.2A). The appearance of this additional peak is ascribed to the

formation of AN-Li$^+$ solvation structure.[65] At salt concentrations above 1 M, AN's strong coordination with the Li$^+$ and near absence of free AN is believed to improve the reductive stability of AN.[62] The interaction of Li$^+$ and FM was also detected in Figure 6.2B. Although solubility of LiTFSI in FM is low (< 0.1 M), a red-shift of the C-F stretching peak (around 1012 cm^{-1}) is observed after adding 0.1 M LiTFSI into pure FM, indicating the bond order of C-F had been impaired as the flourine's lone electron pair coordinate to lithium ion. Furthermore, with 1 M AN and increasing amount of LiTFSI, the C-F peak moves to a lower frequency (around 1010 cm^{-1}). It is likely because more LiTFSI is dissolved with the present of AN, therefore enabling more FM-Li$^+$ coordination. Unlike the inert dilutes seen in localized high concentration electrolytes that not participate the solvation shell and have slow transport kinetics,[36,71] the slightly solvating feature of FM-Li$^+$ in liquefied gas electrolytes is believed to provide extra benefits for the rapid ion transport and desolvation, especially at low temperatures. Raman spectrum of TFSI$^-$ in the 740-755 cm^{-1} region is particularly sensitive to the Li$^+$ coordination, with a band near 740 cm^{-1} assigned to free TFSI$^-$ and 746-753 cm^{-1} is assigned to aggregates.[154] Following this assignment, Figure 6.2C indicates that most TFSI$^-$ anions in dilute LiTFSI-AN (1:20) exist as free anions, while in the LiTFSI-AN-FM electrolytes the TFSI$^-$ anions participate in aggregates due to the high salt-to-cosolvent ratio.[65] The low free TFSI$^-$ indicates a high Li$^+$ transference number measuring experimentally using Bruce-Vincent method[155] (t_{Li^+}=0.72, Supporting information). Solvated TFSI$^-$ is believed to have higher reduction activity over free TFSI$^-$, leading to a favorable interphase for stable Li-metal cycling.[64,156]

Molecular dynamics (MD) simulations were performed on the 1.2 M LiTFSI, 1 M AN in FM electrolyte in order to obtain further insight into the solvation structure and Li$^+$ transport. Representative snapshots (Figure 6.2D-2I) show that at low temperature (-20°C) ions are

distributed rather uniformly throughout the simulation cell but start slowly separating into the ion-rich domain with increasing ion aggregation and ion-poor domains as temperature increases. Such increased ion aggregation results in the eventual conductivity drop at high temperatures. Note that two different snapshots are shown for +40°C corresponding to two different densities: one approximated from experiments at +40°C, while the other corresponds to the compressed electrolyte having a density estimated from measurements at +20°C but simulated at +40°C (Computational methods). Electrolyte compression (compare Figure 6.2G vs. Figure 6.2H) leads to homogenization of the ion domains, changes in the Li solvation shell and ion transport, which agrees well with previously reported phenomena under liquefied gas electrolytes[39,94]. Analysis of the radial distribution functions (RDFs) (Supporting information) indicates a strong preference for the Li^+ to be coordinated by AN followed by the oxygen atoms of TFSI with a smallest peak observed for the Li-F(FM). Based on RDFs we chose 2.8 Å as a first solvation shell of the Li^+ cations (Figure 6.2J) that comprised, on average, of 2.9 O(TFSI) and 0.83 of AN and 0.89 of FM. The Li^+ coordinates to ~3 oxygen atoms of TFSI coming from two $TFSI^-$ anions, one of which has monodentate binding to a Li^+ (Figure 6.2K) while the other has a bi-dentate binding to Li^+ giving rise to an extended chain of aggregates, especially at higher temperatures >+20°C. Notably, electrolyte compression results in dissociation of the larger aggregates and increase in free ion population. Absence in MD simulations of free $TFSI^-$ and free AN, that is not coordinated to a Li^+, is exceptional consistent with Raman spectra (Figure 6.2A, 6.2C),

Figure 6.2J shows that the number of AN around Li^+ is temperature independent and is equal to the ratio of AN to LiTFSI (0.83) further confirming that nearly all available AN solvents are participating in the Li^+ solvation in excellent agreement with interpretation Raman spectra shown in Figure 6.2A. Interestingly, not all Li^+ have the same number of AN around it. Free Li^+

cation (not coordinated to TFSI) tend to have 2 AN and 2-3 FM solvents (Supporting information), thus AN disproportionately contributes to coordination of free Li^+ at the expense of coordinating Li^+ in ionic aggregates consistent with the representative free Li^+ and aggregate solvates shown in Figure 6.2K. As a result of this preference of AN to free Li^+, even in a highly deficient AN co-solvent regime (AN:Li < 1.0) a substantial fraction of free Li^+ exists leading to high Li^+ conductivity.

A temperature dependence of the fraction of free lithium cations correlates well with the degree ion ionic correlated motion (ionicity) (Supporting information), clearly indicating a drop of free ions at higher temperature. Further compression at the highest temperatures, not only increased ionic dissociation but also prevents a drop in ion diffusion coefficients due to ion aggregation resulting in a conductivity improvement (Supporting information). Due to low viscosity of the main solvent (FM) and much higher diffusion of free Li^+ compared to ionic aggregates, vehicular motion of the $Li^+(AN)_2(FM)_n$, n=2 or 3 is the dominant diffusion mechanism. Also, the residence time for Li-FM (32 ps) is much shorter than Li-AN (7407 ps) and Li-N(TFSI) (6926 ps), indicating the rapid ion transport from FM and supporting the vehicular mechanism for the free Li^+ motion. Indeed, diffusion of free Li^+ is 4 times higher than average Li^+ ion diffusion. Finally, because there is essentially no free $TFSI^-$ anions (<0.3% at all temperatures, unlike Li^+) most charge transport occurs via $Li^+(AN)_2(FM)_n$ diffusion leading to high Li^+ transference number predicted from MD simulations (>0.94).
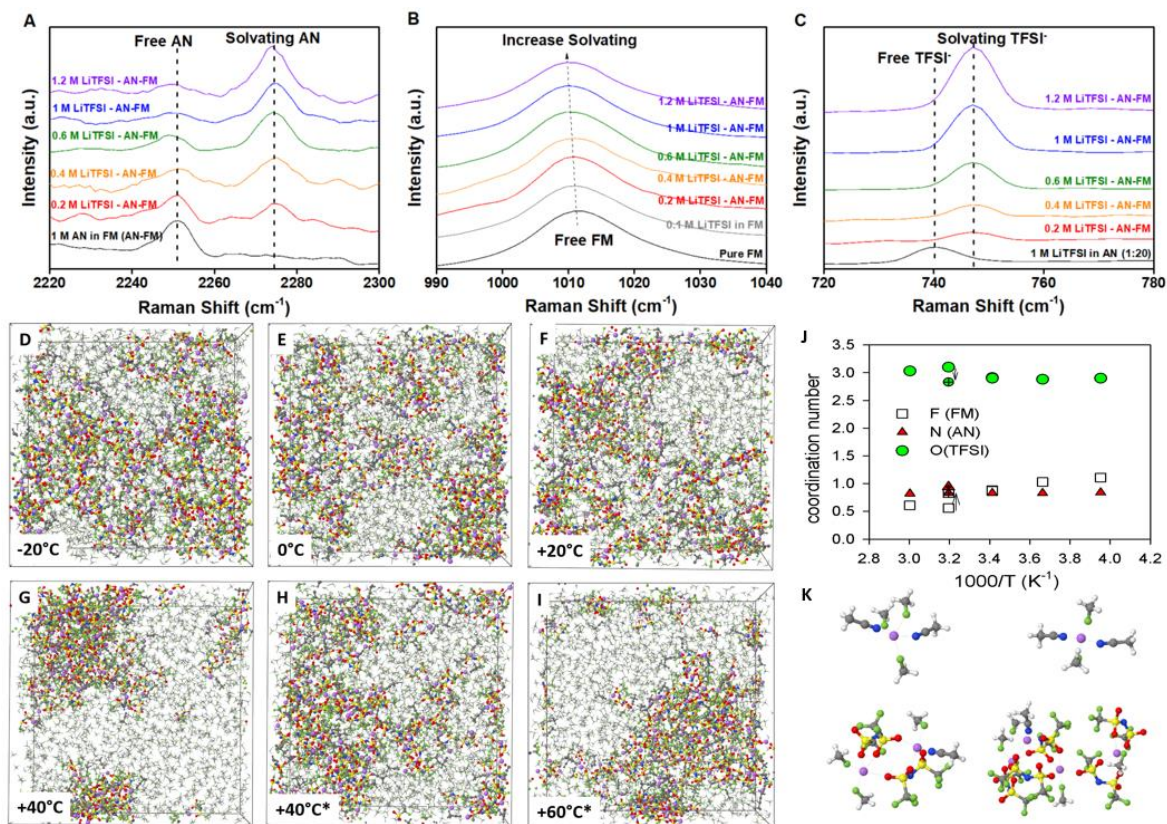
Figure 6.2. Solvation structure. (A-C) Raman spectra. (D-I) Snapshots of the MD simulations cells of 1.2 M LiTFSI-AN-FM electrolyte. (J) Coordination numbers versus temperatures. (K) Representative solvates.

6.3.2 Li Metal Anode Performance

To explore the compatibility of the proposed electrolyte with Li metal anode, Li metal plating and stripping tests were performed. 1 M lithium bis(fluorosulfonyl)imide (LiFSI) in 1,2 dimethoxyethane (DME) was selected as the ether baseline electrolyte due to its well-known compatibility with the Li metal anode. 1.2 M LiPF$_6$ in ethylene carbonate/ethylmethyl carbonate (1.2 M LiPF$_6$ EC/EMC 3:7) was selected as a carbonate baseline electrolyte, as its higher linear carbonate ratio enables an improved low-temperature performance compared to other conventional liquid electrolytes.[7] An aggressive rate of 3 mA·cm^{-2} with a practical capacity of 3 mAh·cm^{-2} was

selected in order to push the limit of this liquefied gas electrolyte.[157] As shown in Figure 6.3A, at 3 mA·cm^{-2} and 3 mAh·cm^{-2}, the CE in the liquefied gas electrolyte (1.2 M LiTFSI, 1M AN in FM:CO$_2$ 19:1, labeled as 1.2 M LiTFSI-AN-FM) increased to >99.1% within the first 20 activation cycles and stable Li plating-stripping was demonstrated up to 200 cycles with an average CE of 99.4%. The minimal increase in overpotential (Figure 6.3B) indicates the SEI formed from liquefied gas electrolyte remains stable even with such a high current density and capacity cycling. In contrast, 1 M LiFSI-DME and 1.2 M LiPF$_6$-EC/EMC electrolytes showed inferior CEs and quick fading, suggesting their poor stability and kinetic limitations.

To further evaluate the Li metal anode performance in a wide temperature range, extended cycling of the Li-metal anode was performed from -60 to +55°C (Figure 6.3C). Using the same aggressive cycling conditions (3 mA·cm^{-2} and 3 mAh·cm^{-2}), the stable Li metal plating/stripping in the liquefied gas electrolyte was maintained in a wide temperature range, showing an average CE of 96.4% at -60°C and 99.4% at +55°C with an overpotential of 310 mV and 28 mV, respectively. After being brought back to room temperature, due to the little affect on the electrolyte and interface properties when exposed to the low and high temperatures, the voltage curve of the Li metal anode matched well with its initial state (Figure 6.3D). As a comparison, ether-based electrolyte and carbonate-based electrolyte provide a lesser performance in a smaller temperature range, even under lower current density and capacity (1 mA·cm^{-2} and 1 mAh·cm^{-2}). Both electrolytes showed an unstable plating and stripping curve at 0 and -30°C, resulting in large fluctuations of CE. Additionally, both cells were unable to cycle at lower temperatures and showed reduced performance after high-temperature cycling.
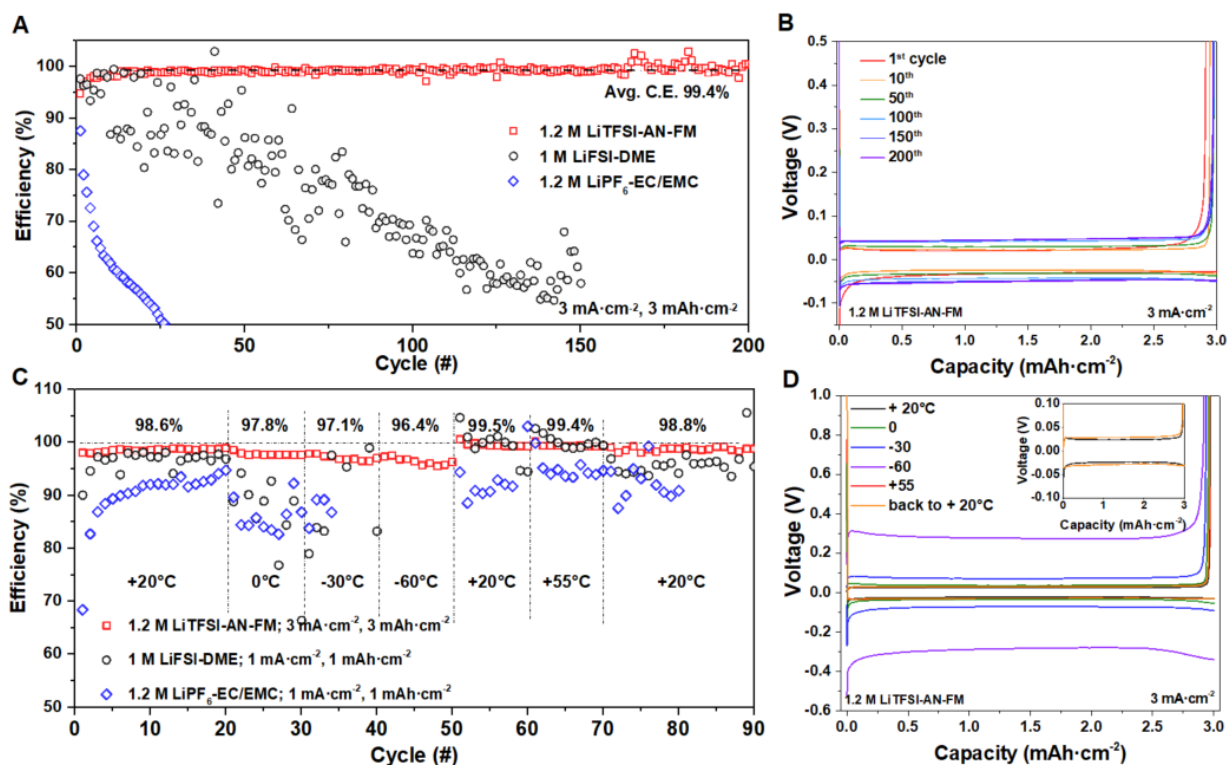
Figure 6.3. Electrochemical performance of Li metal anode. (A) The CE over 200 cycles in various electrolytes, (B) voltage profiles for the cell using liquefied gas electrolyte used in (A). (C) The CE at various temperatures, (D) voltage profiles for the cell using liquefied gas electrolyte used in (C).

6.3.3 Li Metal Structures

The surface morphology and the cross-sectional structure of Li metal deposited in various electrolytes were observed via scanning electron microscopic (SEM) and cryogenic focused ion beam (cryo-FIB). To overcome the difficulties of Li metal characterization due to its high reactivity and low atomic number, cryo-FIB was implemented to minimize the damage and avoid morphological artifacts.[38,47] The samples were prepared with a capacity of 3 mAh·cm^{-2} at 0.5 mA·cm^{-2}, which is close to many potential application scenarios and corresponds to a deposition thickness of ~15 μm for ideal dense Li metal.

Different electrolytes displayed considerably different morphologies in both the surface and the bulk morphologies (Figure 6.4A-H). Consistent with literature, the carbonate-based electrolyte formed needle-like dendrites (Figure 6.4A) with a non-uniform distribution, which leads to a porous bulk structure with high tortuosity and bad structural connections (Figure 6.4E). As shown in Figure 6.4B, dendrite-free deposited Li with large roundly shaped Li particles was enabled by the ether-based electrolyte. Despite the favorable top-view morphology, the cross-section exhibited a large number of voids in the bulk structure, resulting in a relatively high structural tortuosity (Figure 6.4F). However, the Li deposited in the liquified gas electrolyte demonstrated a roundly shaped, densely packed dendrite free surface (Figure 6.4C). Although the primary particle size is slightly smaller than the one generated by the ether-based electrolyte, the bulk structure is largely improved. The liquefied gas electrolyte presents a very dense Li deposition, aside for a few small voids on the Li/substrate interface formed during nucleation (Figure 6.4G). This indicates that the Li growth during deposition is completely uniform, which may be attributed to the high kinetics of the electrolyte and the stable interface. Further, the differences in surface morphology between the conventional liquid electrolyte and the liquefied gas electrolyte are even more apparent after several cycles (Supporting information).

The morphology of Li deposited at low temperature (-60°C) was also investigated in 1.2 M LiTFSI-AN-FM (Figure 6.4D, H). The primary particle deposited at low temperature has a smaller size, which is consistent with previous studies.[42,43] Literature has shown that dendrites are easier to form at low temperatures (< -20°C) in most of the electrolytes due to the smaller nucleation size and sluggish Li$^+$ diffusion.[42,43] However, even at -60°C, the liquified gas electrolyte supports roundly shaped primary particles and a dense Li deposition with a close contacted Li-substrate interface, in which barely any voids are observed (Figure 6.4H). It is

believed that the smaller nucleation size at lower temperature enhances the Li-substrate contact by eliminating the voids seen at room temperature while the dense dendrite-free deposition is maintained due to the fast kinetics of liquefied gas electrolyte at low temperatures. The described Li deposition models are illustrated in Figure 6.4I-L. The structure by liquified gas electrolyte agrees well with the recent proposed ideal Li metal structure.[28] The chunky morphology and low tortuosity of deposited Li in the liquefied gas electrolyte enables an ideal structural connection, and therefore, explains the high CE and stability even at high current and low-temperature.
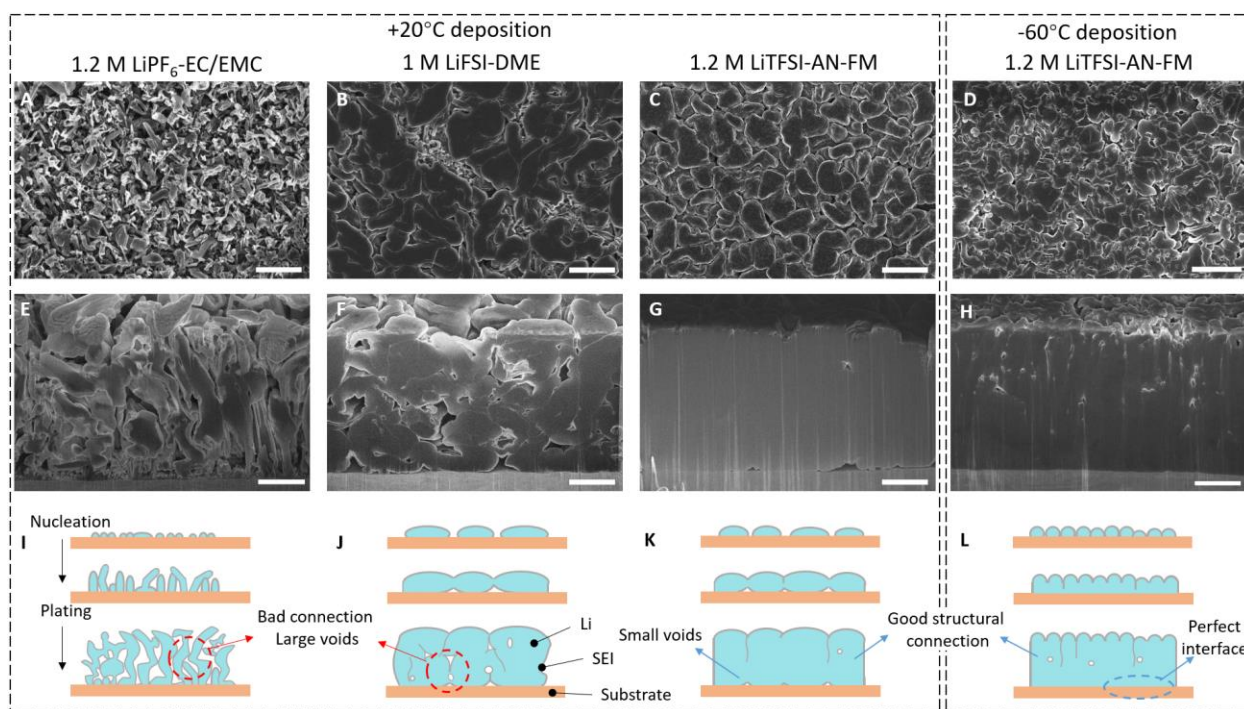
Figure 6.4. Cryo-FIB characterization of the morphologies of electrochemically deposited Li. (A-D) top-view SEM images (A-C, scale bar 10 µm; D, scale bar 5 µm), (E-H) cross-sectional SEM images (scale bar 4 µm) of deposited Li, and its schematic illustration (I-L).

6.3.4 Electrochemical Performance of Li Metal Batteries

Li-LiNi0.6Mn0.2Co0.2O2 (NMC622) full cells with an areal loading of ~1.8 mAh·cm^{-2} were then used to investigate the anodic stability of the various electrolytes. The improved liquefied gas electrolyte showed high anodic stability up to 4.5 V in Li-NMC voltage hold test (Supporting information). At a cutoff voltage of 4.3 V, the Li-NMC cell had a discharge capacity of 167 mAh·g^{-1} and enables >96.5% capacity retention after 500 cycles with an average CE of 99.7% (Figure 6.5A, B). In contrast, carbonate-based and ether-based electrolyte displayed quick fading and limited capacity retention after 200 cycles. When the cutoff voltage was increased to 4.5 V, an initial discharged capacity of 191 mAh·g^{-1} with a >91.5% capacity retention was still maintained after 200 cycles, resulting an average CE of 99.5%. In the liquefied gas electrolyte, the Al corrosion by imide salt (LiTFSI/LiFSI) was also largely reduced (Supporting information) because of the absence of free AN in electrolyte as all AN solvent molecules are bound to Li$^+$. The only free solvent is a fluorinated FM solvent with a low solvation power for the Al corrosion products and containing fluorine to passivate the Al surface.[59,158]

Cyclic voltammetry (CV) tests of Li-NMC full cells were then performed to investigate the kinetic behavior at lower temperatures for different electrolytes (Figure 6.5C, F). At +20°C, 1.2 M LiTFSI-AN-FM and 1.2 M LiPF$_6$-EC/EMC electrolyte showed similar de-lithiation and lithiation peaks. However, at lower temperatures, 1.2 M LiPF$_6$-EC/EMC electrolyte experienced a large voltage shift at -30°C and no redox peak was observed at -60°C, suggesting a higher resistance and slower kinetics occur at reduced temperature. In contrast, the use of liquefied gas electrolyte showed a smaller peak shift in comparison to the carbonate electrolyte and the charging/discharging process is still distinct at -60°C. This behavior is indicative of rapid kinetics

through the bulk electrolyte and interfaces, illustrating improved low-temperature performance. To simulate real battery applications, all cells in cycling tests were charged and discharged at the same temperature, rather than charged at room temperature followed by low-temperature discharge.[70,141] The discharge curves of different electrolytes at various temperatures are shown in Figure 6.5D, G. Although the 1.2 M $LiPF_6$-EC/EMC electrolyte showed a similar capacity of ~200 mAh·g^{-1} at +20°C and rate of C/15, the Li-NMC cell in the carbonate electrolyte could deliver only < 25% capacity retention at -40°C and could not deliver any capacity at -60°C. However, the use of 1.2 M LiTFSI-AN-FM liquefied gas electrolyte enabled 60% and 45% capacity retention at -40°C and -60°C, respectively. Note that if the cell was charged at room temperature, a higher capacity of 65% can be achieved at -60°C (**Supporting information**). This difference highlights the significant influence of temperature on the charging process. The capacity improvement from room temperature charging is likely due to the kinetic barrier in low temperature charging. This kinetic barrier may lead to issues in some electrolytes, even if they show reasonable low-temperature discharge performance. In low temperature (-20°C) long-term cycling, the capacity of the Li-NMC cells using 1.2 M LiTFSI-AN-FM maintains stable and is 36% and 52% higher than the cells using 1.2 M $LiPF_6$-EC/EMC at C/5 and C/3 rate, respectively (**Figure 6.5E**). This superior low-temperature performance is also highlighted by a Li-NMC full cell using liquefied gas electrolyte powering a LED light at temperatures as low as -78°C in dry ice.

The liquefied gas electrolyte with increased amount of salt and cosolvent also demonstrated improved high-temperature operation. When the temperature was increased to +55°C, the cell using the liquefied gas electrolyte showed a similar discharge curve (**Figure 6.5D, G**) and redox process , with slightly faster kinetics than the cell using the 1.2 M $LiPF_6$-EC/EMC. In subsequent charge/discharge cycles, the Li-NMC cell in 1.2 M LiTFSI-AN-FM maintained high capacity

retention at around 200 mAh·g^{-1}, while the liquid cell using 1.2 M LiPF$_6$-EC/EMC started to decay in less than 20 cycles (Figure 6.5H). This fading may result from the increase of electrolyte side reactions and the instability of the SEI/CEI at elevated temperatures.
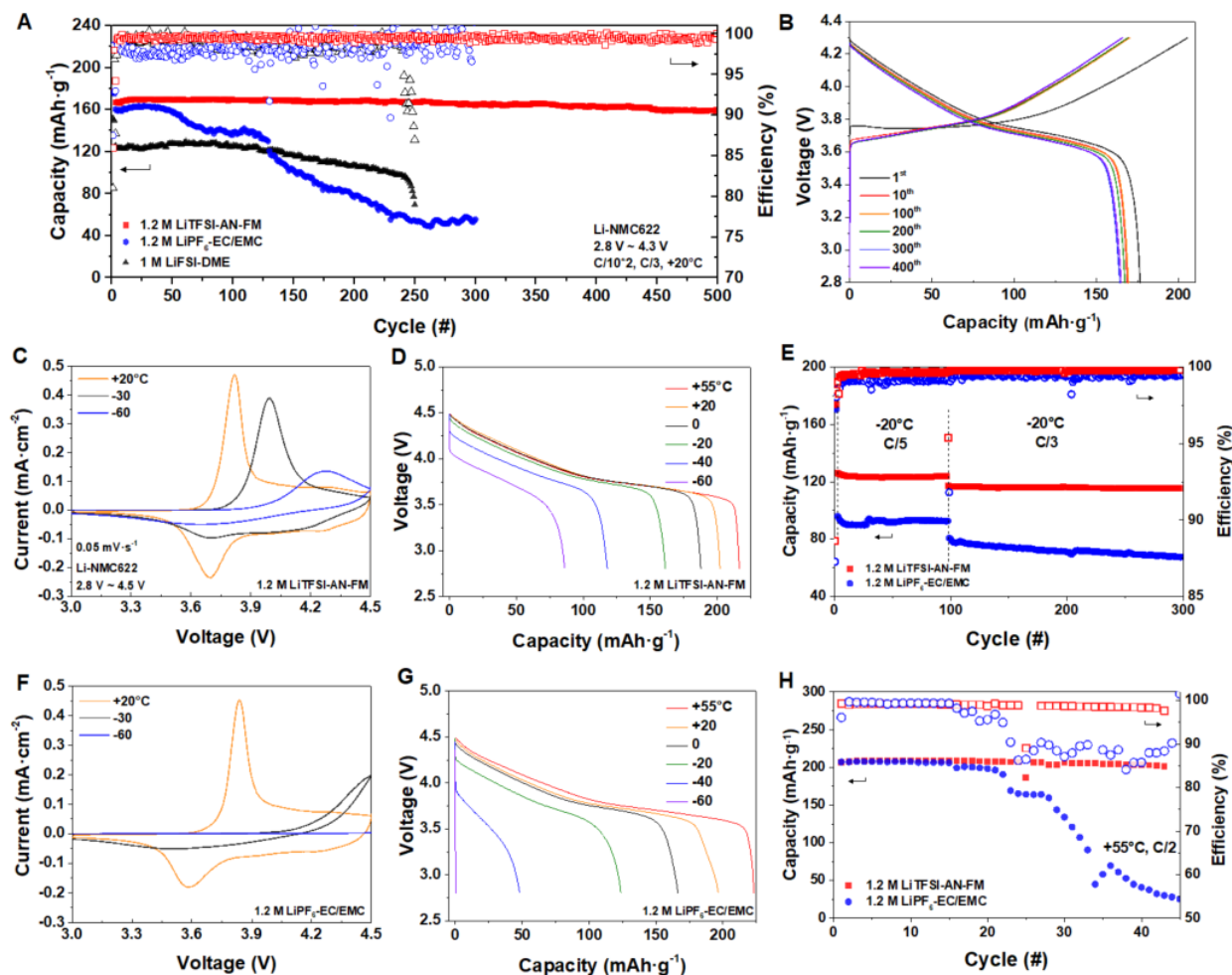
Figure 6.5. Electrochemical performance of Li-NMC622 cells. (A-B) Cycling performance of Li-NMC622. Cyclic voltammetry curves (C, F) and discharge profiles (D, G) of Li-NMC at different temperatures. Cycling performance of Li-NMC622 at -20°C (E) and +55°C (H).

6.3.5 Interface Characterizations

The chemistry and structure of cycled Li-NMC interfaces (CEI, SEI) were characterized by cryogenic-(scanning) transmission electron microscopy (cryo-(S)TEM) and X-ray

100

photoelectron spectroscopy (XPS). Cryo-TEM was applied on cycled NMC622 to preserve the cathode electrolyte interphase (CEI) from beam damage.[64] After 50th discharge, the CEI in carbonate-based electrolytes shows significant variations in both thickness and distribution (Figure 6.6A). This result is consistent with the observation in EDS under STEM mode, that the CEI of the same NMC particle displays a different phosphorus distribution at different planes. In contrast, the CEI generated in the liquefied gas electrolyte exhibits a much more uniform thickness with good surface coverage (Figure 6.6B). This agrees with the relatively uniform sulfur distribution observed in STEM-EDS (Supporting information). XPS of cycled NMC also captures the S 2p signal in the liquefied gas electrolyte and shows different chemistry in various electrolytes (Figure 6.6C). After being cycled in carbonate-based electrolyte, the oxygen ratio largely increased and the shape of carbon peak changed, indicating the formation of an organic-like CEI layer. Whereas the CEI formed using the liquefied gas electrolyte shows a similar carbon peak found in the pristine NMC with less oxygen increase. Additionally, LiF, S-O, N-O species are formed by the decomposition of LiTFSI and FM, which are believed to potentially promote a protective interphase.[19]

Depth-profiling XPS was also applied to cycled Li metal anode interfaces in different electrolytes (Supporting information). Consistent with previously studies,[38,39] the liquefied gas electrolyte forms an inorganic-rich SEI by decomposition of FM, CO_2, and TFSI[-], enabling a robust interface for aggressive Li metal cycling. The detailed discussion and comparison to the carbonate electrolyte are included in the supporting information.
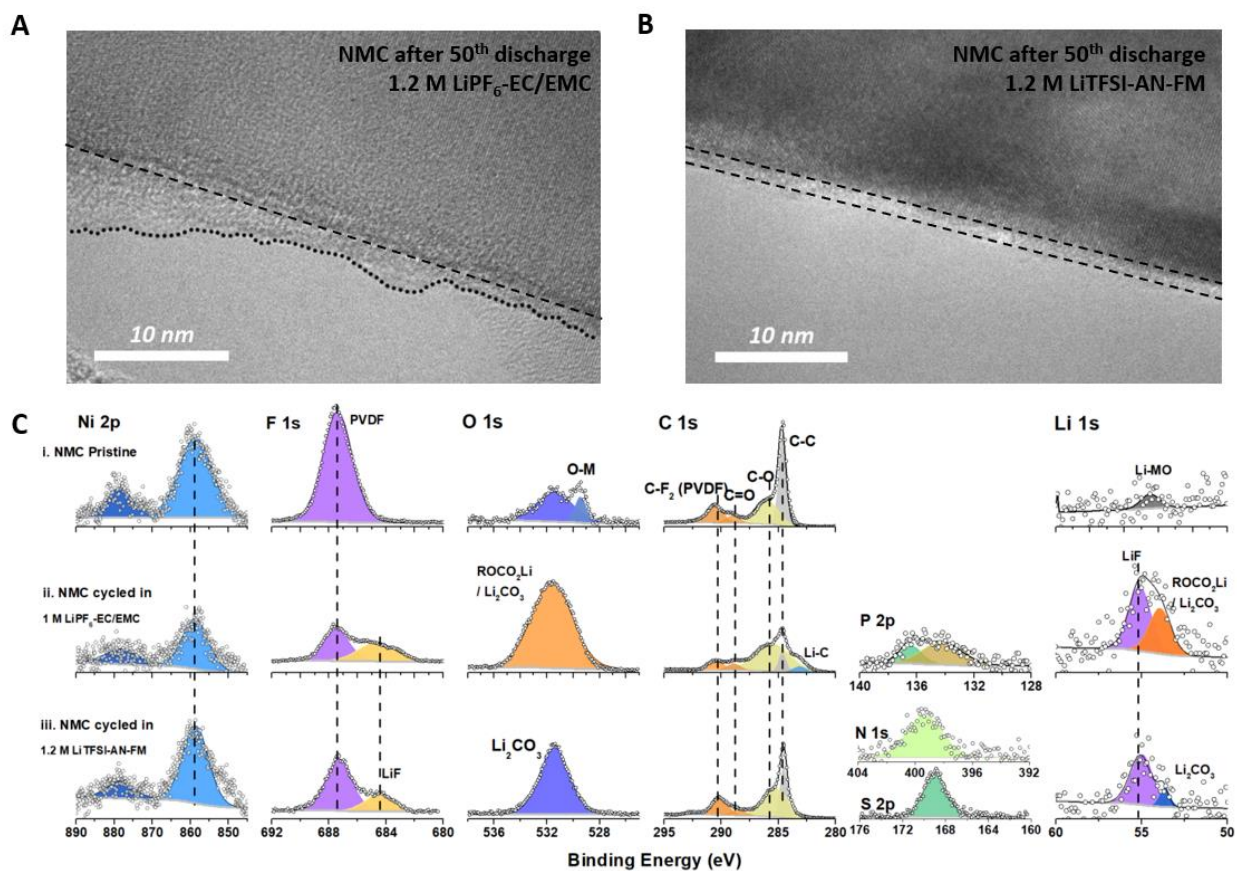
Figure 6.6. Interfaces characterizations of cycled NMC622. (A, B) Cryo-TEM images of NMC particle after 50th discharge in 1.2 M LiPF$_6$-EC/DMC (A) and 1.2M LiTFSI-AN-FM (B). (C) XPS chemical analysis of CEI layers.

6.4 Conclusion

By introducing an AN cosolvent and improving salt concentration, we developed a liquefied gas electrolyte with unique physical and chemical properties that supported rapid ion transport and desolvation, impressive Li-metal compatibility, high anodic stability, and wide temperature operation window. The unique solvation structure uncovered by Raman and MD simulation show that AN cosolvent is fully solvated to Li$^+$ and FM is partially coordinated with Li$^+$ with short residence times. This ideal solvent-cosolvent combination yields superior transport properties, including high low-temperature conductivity (4.8 mS·cm^{-1} at -78°C), expanded high-

temperature operation range (from +40°C to > +75°C), and high transference number. Systems using the liquefied gas electrolyte formed stable interfaces at both the Li-metal and the cathode sides. It enabled high Li-metal CE of 99.4% at high current density of 3 mA·cm^{-2} and 3 mAh·cm^{-2}, as well as stable cycling of 4.5 V Li-metal batteries in the wide-temperature range between +55 and -60°C. The developed liquefied gas electrolyte presents a promising pathway towards next-generation high-energy Li-metal batteries with wide-temperature operations.

Chapter 6, in full, is a reprint of the material "Liquefied Gas Electrolytes for Wide-Temperature Lithium Metal Batteries" as it appears in *Energy & Environmental Science*, Yang, Y.; Yin, Y.; Davies, M. D.; Zhang, M.; Mayer, M.; Zhang, Y.; Sablina, E. S.; Wang, S.; Lee, J. Z.; Borodin, Oleg.; Rustomji, C. S.; Meng, Y. S., 2020, DOI: 10.1039/D0EE01446J. The dissertation author was the primary investigator and first author of the paper. All of the experiments parts and characterizations were performed and analyzed by the author except for the molecular dynamics simulation and cryo-TEM.

Chapter 7. Fire-Extinguishing Recyclable Liquefied Gas Electrolytes for Lithium Metal Batteries

7.1 Introduction

In recent decades, the demand for batteries has increased exponentially and applications have expanded from small-scale portable electronics to large-scale scenario such as EV and grid storage. In addition to the need for high energy density and high cycle life, different scenarios also call for batteries that are safe, capable of operation in a wide temperature range, and readily recyclable. However, the ethylene carbonate (EC)-based electrolytes in commercial batteries are highly flammable with a narrow temperature window (-20 to +50°C), causing a major barrier for battery safety, wide-temperature operations, and recycling processes.[7]

Extensive efforts have been devoted to developing non-flammable electrolytes with balanced properties. Solid-state electrolytes are non-flammable and have shown advantages in safety, however, the ionic conductivity suffers even at moderate low temperatures (< 0°C). In liquid electrolytes, only organic phosphates solvents (i.e. trimethyl phosphate (TMP), triethyl phosphate (TEP)) are non-flammable.[159,160] However, regular phosphates are unable to form stable solid electrolyte interphases (SEI) on both graphite and lithium (Li) metal anode.[159–161] Increasing salt concentrations can promote salt-derived inorganic SEI and consequently improve the interface stability.[162] Yet, cost, viscosity, wetting, and low-temperature performance are sacrificed in high concentration electrolytes. More recently, localized high-concentration electrolytes (LHCE) were formulated by adding inert dilutes and could diminish these issues. Non-flammable LHCEs were formed by coupling flammable inert dilutes like bis(2,2,2-trifluoroethyl) ether (BTFE) with TMP or TEP (~25 wt. %).[36,163,164] Fire-retardant LHCEs were also formulated by using non-flammable

dilutes like 2,2,2-trifluoroethyl 1,1,2,2-tetrafluoroethyl ether (HFE) with main solvents other than phosphates.[70,74] Although these LHCE delivered a relatively good cell cycling performance, the dilutes are either flammable or have high viscosity, with relatively low boiling point (BTFE, +62°C; HFE, +57°C). Due to these unbalanced properties, there are still safety concerns under abusive conditions such as overheating and overcharging.

Battery recycling has been increasingly significant to reduce the capital cost and to minimize environmental impact. A sustainable and practical process is required, which should be able to separate and recycle all the components in safe, environmental-friendly, and cost-effective approaches. However, most recycle studies still only focus on recyclability of the electrodes level with little attention to the electrolyte. The regular method is just washing the electrolyte away with different solvents, compromising cost and resulting in environmental issues. Currently, there are no practical approaches to effectively separate and recycle electrolytes from batteries.

Herein, we rationally designed liquefied gas electrolytes that addressed the above challenges. The tamed electrolytes are non-flammable with unique fire-extinguishing features, which could rapidly cool down the cells under abusive conditions. Additionally, we demonstrated a simple process for electrolyte separation and reuse, attributed to the unique features of the liquefied gas solvents. The electrolytes also exhibit fast ionic transport and enable battery operations in a wide-temperature range from -78°C to +80°C with impressive performance with lithium metal anode and 4 V class cathodes.

7.2 Experimental section

7.2.1 Materials

Dimethyl Ether (99%) and 1,1,1,2-tetrafluoroethane (99%) were obtained from Sigma-Aldrich. Pentafluoroethane (99%) were purchased from SynQuest Labs. The salts Lithium bis(fluorosulfonyl)imide (LiFSI) (99.9%) and lithium bis(trifluoromethane)sulfonimide (LiTFSI) (99.9%) were purchased from BASF. 1.2 M $LiPF_6$ in EC/EMC 3:7 was obtained from BASF. 1,2-dimethoxyethane (DME, 99.5%) were purchased from Sigma-Aldrich and stored over molecular sieves. The NMC622 (A-C023) was supplied by Argonne national laboratory.

7.2.2 Electrochemical measurements

Electrolytic conductivity measurements were performed in custom fabricated high-pressure stainless-steel coin cells, using polished stainless-steel (SS 316L) as both electrodes. The cell constant was calibrated from 0.447 to 80 mS·cm^{-1} by using OAKTON standard conductivity solutions.

Battery cycling test was performed using an Arbin battery test station (BT2043) from Arbin Instruments in custom designed high-pressure stainless-steel coin cells. Li metal (FMC Lithium, 1 mm thickness, ¼ inch diameter) and a polished SS316L were used as the counter electrode and the working electrode, respectively. A single 25µm porous polypropylene separator (Celgard 2075) was used for all the electrochemical tests.

For Li metal plating and stripping experiments, lithium was first deposited onto the working electrode at 0.5 mA·cm^{-2} until 0 V vs. Li and the voltage was held for 5 hours to form a stable SEI on the current collector. The first plating cycle was then started, followed by complete

lithium stripping to a 1 V vs. Li cut off voltage. The CE was calculated as the Li stripping capacity divided by the Li plating capacity during each single cycle.

7.2.3 Material characterization

X-Ray photoelectron spectroscopy (XPS) was performed using a Kratos AXIS Supra DLD XPS with monochromatized Al Kα radiation (λ= 0.83 nm and hυ=1486.7 eV) under a base pressure <10^{-8} Pa. To avoid moisture and air exposure, samples were transferred to the XPS chamber directly from a glovebox via vacuum transfer. All spectra were calibrated with hydrocarbon C 1s (284.6 eV) and analyzed by CasaXPS software. To remove residual salt on the surface, all samples were slightly rinsed with DMC and dried in glovebox antechamber before analysis.

7.3 Results and discussion

7.3.1 Taming the liquefied gas electrolytes

The recently developed fluoromethane (CH3F, FM)-based liquefied gas electrolytes demonstrated impressive battery operations down to -60°C and stable cycling of Li-metal anode and 4 V class cathodes. The performance is attributed to FM's unique properties, including low melting point, low viscosity, and stable C-F bond. However, FM has a relatively low solvation power with Li$^+$ (< 0.1 M LiTFSI solubility) and consequently other liquid cosolvents need to be introduced to improve salt solubility. Additionally, FM is flammable and has a relatively high vapor pressure, which may cause safety threats under harsh conditions.

To address these issues, a wider molecular screen was made, not limited to previously studied hydrofluorocarbons. Criteria for potential liquefied gas solvents include 1) higher solvation ability for better salt solubility; 2) lower vapor pressure and 3) low to non-flammability for

107

improved safety; 4) low viscosity and low melting point for good low-temperature performance. Analogized from other ethers' properties (Figure 7.1A), dimethyl ether (Me_2O) is expected to have relatively good solvation ability, reductive stability, and rapid transport. As the simplest ether, Me_2O is at gaseous state under ambient conditions, with significantly higher critical point and lower vapor pressure over FM (Table 7.1). Although Me_2O is still flammable, the improvement is seen in the combustion products, which are environmentally friendly (i.e. H_2O). Whereas combustion of flammable fluorinated components (i.e. BTFE and FM) results in the generation of hydrogen fluoride.

Furthermore, a non-flammable liquefied gas solvent with lower solvation power could be introduced as a cosolvent. The liquefied gas cosolvent would be expected to not only improve safety but also the anodic stability by decreasing free Me_2O. Inspired by fire-extinguishing agents (Figure 7.1B), 1,1,1,2-tetrafluoroethane (TFE) and pentafluoroethane (PFE) were identified as potential liquefied gas cosolvents, as they are widely used in extinguishers. Unique properties of TFE and PFE include a high flash point (+250°C) and non-flammability, respectively. These molecules also have low viscosity, high chemical stability, and low solvation ability (Table 7.1). With moderate vapor pressure, they could cool down the heat source and its surroundings by gasification endothermic and also suddenly decrease the concentration of oxygen locally. The moderate vapor pressure would also enable a simple separation and recycle process, which will be discussed in later sections. Overall, TFE and PFE are expected to be promising candidates as liquefied gas solvents. Lithium bis(fluorosulfonyl)imide (LiFSI) and lithium bis(fluorosulfonyl)imide (LiTFSI) are considered as appropriate salt options due to their lower desolvation energy over $LiPF_6$ and $LiBF_4$ and formation of advantageous interfaces.

Dedicated solubility tests on LiTFSI/LiFSI-Me$_2$O-TFE/PFE mixture were performed to check the solubility and mixing properties (Figure 7.2), the results of which are detailed in the supporting information. 1 M LiFSI, 1.7 M Me$_2$O in TFE (labeled as 1 M LiFSI-Me$_2$O-TFE) and 1 M LiTFSI, 1 M Me$_2$O in PFE (labeled as 1 M LiTFSI-Me$_2$O-PFE) are selected for this work. The proposed solvation structure of these low solvating power electrolytes (1 M LiFSI-Me$_2$O-TFE) is shown in Figure 7.1C.
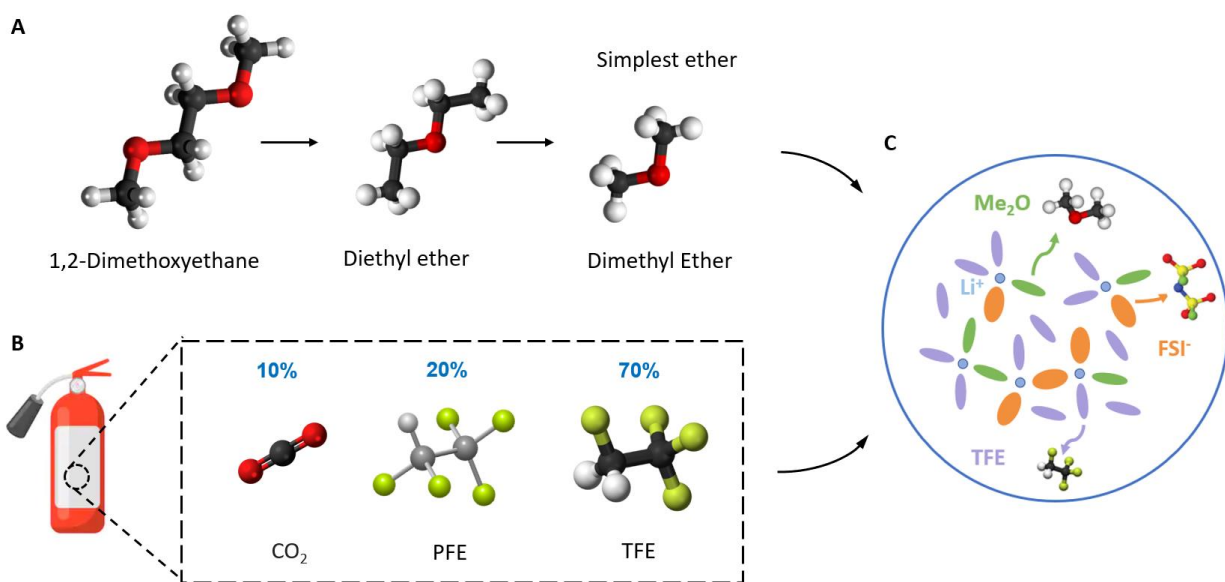
Figure 7.1. Design of the Liquefied Gas Electrolytes (A) As the simplest ether, selected dimethyl ether is expected to exhibit properties like other ethers. (B) Composition of clean extinguishing agent FS 49 C2. (C) Proposed solvation structure of designed liquefied gas electrolytes.

Table 7.1. Physical properties of the liquefied gas solvent studied.

Solvent	Melting Point (°C)	Boiling Point (°C)	Critical Point (°C)	Flash Point	Vapor Pressure (psi)	Dipole	Dielectric Constant	Viscosity (mPa·s)
Fluoromethane	-144	-78	44	-	494	1.85	9.7	0.085
Dimethyl Ether	-141	-24	127	-41	75	1.3	5.02	-
1,1,1,2-Tetrafluoroethane	-103	-26.3	101	250	82	2.06	9.7	0.207
Pentafluoroethane	-103	-48.5	66	None	175	1.56	4.5	0.15

	1 M LiTFSI	1 M LiFSI
Pure Me$_2$O	Dissolved	Dissolved

In TFE		
LiTFSI	1.5 M Me$_2$O	1.7 M Me$_2$O
1 M	P	M
LiFSI	1.5 M Me$_2$O	1.7 M Me$_2$O
1 M	P	M

In PFE		
LiTFSI	1 M Me$_2$O	1.5 M Me$_2$O
1 M	M	M
LiFSI	1 M Me$_2$O	1.5 M Me$_2$O
1 M	S	S

Dissolved/Mixed
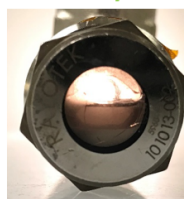
Salt Precipitation

Phase Separation

Figure 7.2. Solubility test on LiTFSI/LiFSI-Me2O-TFE/PFE mixture.

7.3.2 Transport and safety properties

The electrolytic conductivity measurements of the liquefied gas electrolytes were performed (Figure 7.3A). Different from a regular liquid electrolyte conductivity curve, both 1 M LiFSI-Me$_2$O-TFE and 1 M LiTFSI-Me$_2$O-PFE show a relatively flat conductivity curve with sufficient ionic conductivity in a wide temperature range (-78 to +80°C). Especially, 1 M LiFSI-Me$_2$O-TFE enables a conductivity of 5.7 mS·cm^{-1} at +20°C. Attributed to the low viscosity, low melting point, and high critical point, it supports an excellent ionic conductivity of 4.5 and 5.6 mS·cm^{-1} at -78 and +80°C, respectively. The conductivity at low temperature compares favorably to most of the other electrolyte systems.[70,141,153]

110

The vapor pressure curve in a wide temperature range for different liquefied gas solvents and electrolytes is shown in Figure 7.3B. Compared to previously applied FM and CO_2, the vapor pressure of Me_2O, TFE, and PFE is largely decreased. Specifically, Me_2O, TFE and PFE are around 15%, 17%, and 35% of FM's vapor pressure, respectively. Me_2O and TFE have similar vapor pressure in a wide temperature range with high critical points. This results in superior properties for the 1 M LiFSI-Me_2O-TFE electrolyte, such as improved safety and wide temperature operations. The safety feature of these liquefied gas electrolytes will be significant under harsh situations (Figure 7.3C). If the cell is operated at an abusive condition (such as overheated) or if cell penetration occurs, the liquefied gas solvents will evaporate away through a pressure gate or the penetrated hole. The rapid evaporation will absorb the heat and cool down both the overheated cell and the surroundings. As there will be little to no solvent left in the cell, limited ionic transport would eliminate the possibility of thermal runaway. Additionally, the evaporated solvent is fire-retardant, which will create an inert environment around the cell. Even if a fire was started, the evaporated solvents would function exactly as a fire extinguisher by: 1) reducing the heat; 2) isolating the fuel.; 3) reducing the oxygen.
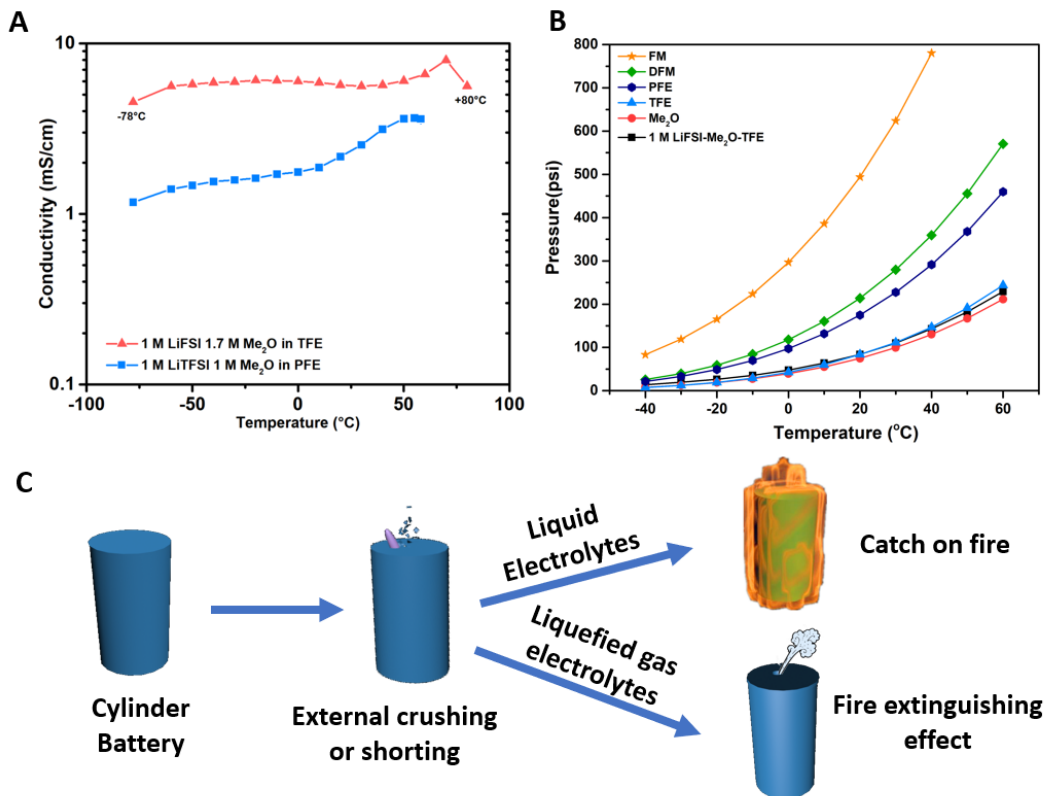
Figure 7.3. Properties of Liquefied Gas Electrolytes (A) Ionic conductivity over temperature of liquefied gas electrolytes. (B) Vapor pressure curves of various liquefied gas solvents and electrolytes. (C) Schematic of fire extinguishing and cooling down mechanism.

7.3.3 Electrochemical performance

Electrochemical tests of Li metal anode and Li metal batteries were performed in 1 M LiFSI-Me$_2$O-TFE liquefied gas electrolyte. 1 M LiFSI in 1,2 dimethoxyethane (DME) and 1.2 M LiPF$_6$ in ethylene carbonate/ethylmethyl carbonate (1.2 M LiPF$_6$ EC/EMC 3:7) were selected as ether and carbonate baseline electrolytes.

Li metal soak tests were first performed to check the compatibility of liquefied gas solvents and electrolytes (Supporting information). After three days of soak, the Li metal in TFE still maintains its shape but turns to black in color, indicating moderate compatibility between Li metal

and TFE. The compatibility for Me_2O is improved in comparison to TFE, as expected. For the 1 M LiFSI-Me_2O-TFE electrolyte, the Li metal retains a clean and shinning appearance. X-ray photoelectron spectroscopy (XPS) shows that a LiF-rich SEI is formed on the soaked Li metal (Supporting information). Due to the low solvating feature of liquefied gas solvents, majority of the LiTFSI salt stays in an aggregated state and will start to reduce at higher potential, leading to salt decomposition dominating the protective inorganic SEI.

For Li metal plating/stripping tests, the ether based liquid electrolyte could cycle relatively good under a mild condition (0.5 $mA \cdot cm^{-2}$, 1 $mAh \cdot cm^{-2}$). However, under an aggressive rate of 3 $mA \cdot cm^{-2}$ with a practical capacity of 3 $mAh \cdot cm^{-2}$, Li metal anode in the ether based liquid electrolyte could only cycle regularly for a few cycles before experiencing a quick drop in the coulombic efficiency (CE), (Figure 7.4A). On the contrary, the liquefied gas electrolyte delivered a first cycle CE of 96.8% and supported a stable long-term Li metal cycling with average CE of 99.1% after formation cycles for 200 cycles (Figure 7.4A), demonstrating excellent compatibility with Li metal anode and verifying the stability of the salt derived interface.

Li-$LiNi_{0.6}Mn_{0.2}Co_{0.2}O_2$ (NMC622) cells with an average loading of ~1.8 $mAh \cdot cm^{-2}$ were used to investigate the anodic stability of the liquefied gas electrolyte. From Li-NMC voltage hold test in the supporting information, 1 M LiFSI-Me_2O-TFE electrolyte exhibits good oxidation stability up to 4.4 V. This suggests that Me_2O has effectively been protected, as illustrated in the proposed solvation structure. At a cutoff voltage of 4.2 V, Li-NMC 622 cell in the liquefied gas electrolyte presented a capacity of 153 $mAh \cdot cm^{-2}$ under C/3 and maintained an 88% capacity retention after 200 cycles with an average efficiency of 99.5% (Figure 7.4B). When the temperature was reduced to -20°C, cells in 1 M LiFSI-Me_2O-TFE could still deliver a capacity of 94 $mAh \cdot cm^{-2}$ at C/3 and the capacity retention after 250 cycles was as high as 97.7% (Figure 7.4C).

However, the cells in the carbonate-based electrolyte showed lower capacity and quick capacity fading under the same conditions. The impressive cycling at low temperature in liquefied gas electrolytes demonstrated their advantages on not only quick transport through the bulk electrolyte but also the formation of stable, low resistance interfaces.
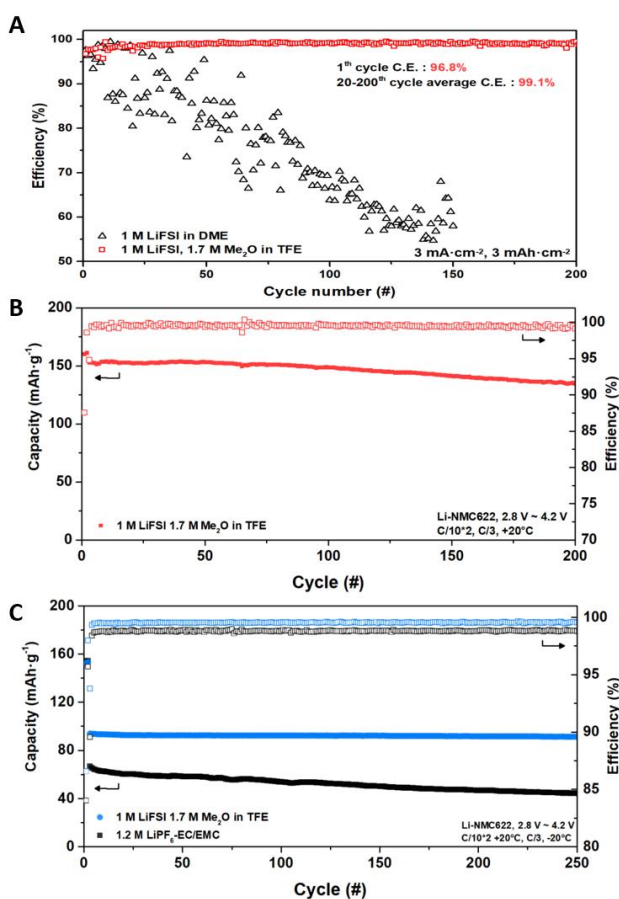
Figure 7.4. Electrochemical performance of lithium metal anode and Li-NMC622 cells in liquefied gas electrolytes (A) The CE of Li metal plating/stripping over 200 cycles in various electrolytes. (B-C) Li-NMC622 long-term cycling at +20°C (B) and -20°C (C).

7.3.4 Recycle of liquefied gas solvent

To better understand the bottleneck of the battery recycling process, a close loop of Li metal batteries recycling is summarized (Figure 7.5A). Even under lean electrolyte condition, the

electrolyte still takes a large ratio in weight (24%)[164] in the Li-NMC pouch cells. The electrolyte ratio would be even higher for more porous electrodes, such as sulfur. The separation of the electrolyte from electrodes is the first challenge due to the porous, high surface area of the electrodes and low viscosity of the liquid electrolyte.

Using the vapor pressure-temperature relationship in liquefied gas solvents, a practical solvent recycle process is proposed (Figure 7.5B). If a temperature difference is generated between two connected containers with liquefied solvent inside, the solvent will transfer and liquefy in the low-temperature container. This solvent transfer is driven by the pressure difference generated by differed temperatures. The proposed method could potentially be a simple approach to collect and reuse the solvent. Tests using window cells were first performed to directly observe the solvent transport (Figure 7.5C). A window cell with 1 M LiFSI-Me$_2$O-TFE was placed in a temperature chamber with a higher temperature (+40°C, P$_{vapor}$ =143 psi), which was connected to a second window cell with the same amount of LiFSI in a chamber with lower temperature (-40°C, P$_{vapor}$ = 13.9 psi). Driven by the large pressure difference, most of the solvents in the high-temperature cell was transferred and liquefied in the lower temperature end. This resulted in a well-mixed, new 1 M LiFSI-Me$_2$O-TFE electrolyte, proving the capability to recycle liquefied gas electrolytes. Using the same process, the solvent of 1 M LiFSI-Me$_2$O-TFE in a cycled Li-NMC coin cell was successfully transfer into a newly assembled Li-NMC cell without adding any extra solvent. Notably, the performance for electrolyte recycled cell showed nearly identical capacity, efficiency, and voltage curve in comparison to the original cell (Figure 7.5D). These results demonstrate the effectiveness of this simple solvent recycle process. With further optimizations, this process is promising for practical liquefied gas electrolytes recycling.
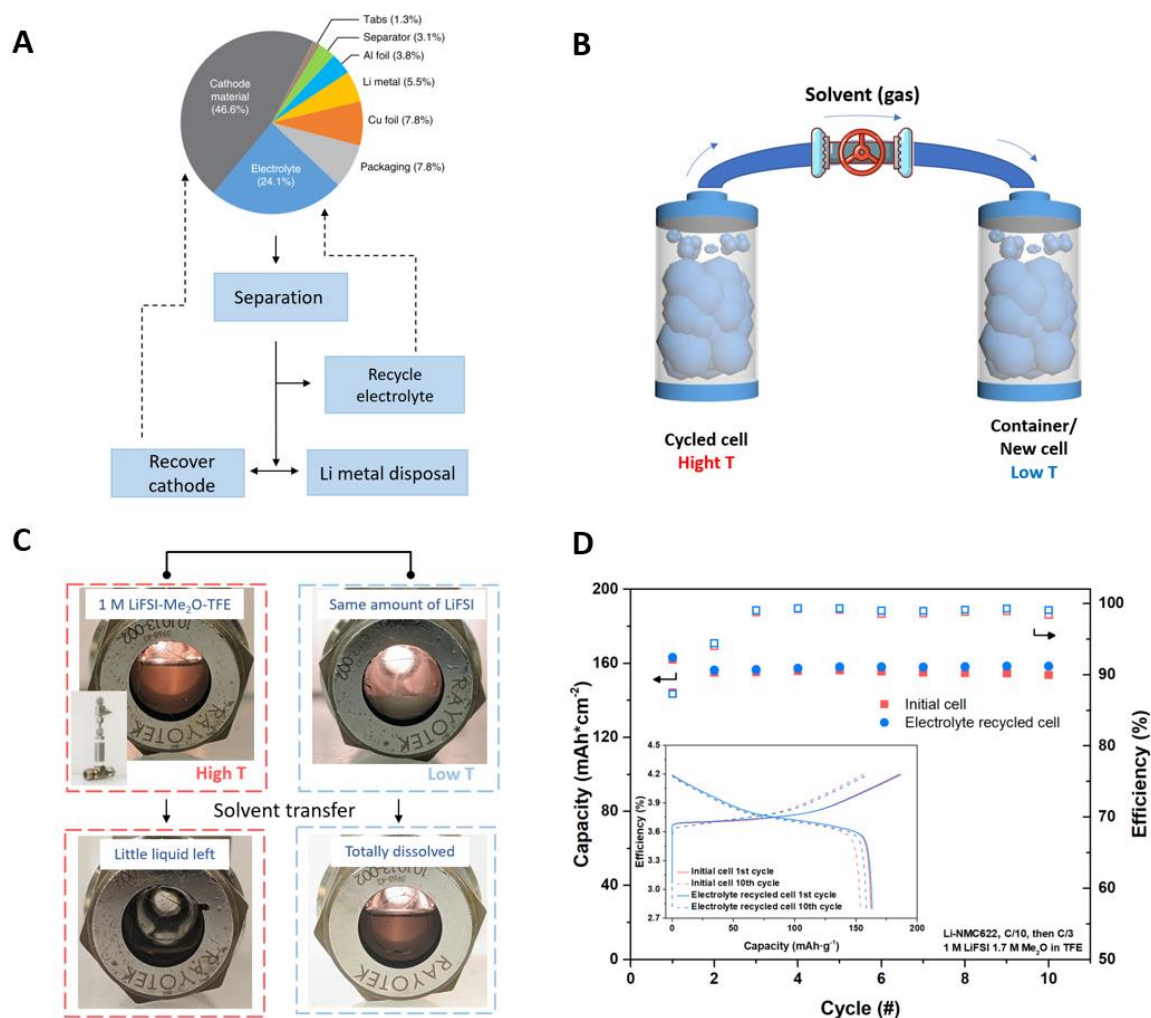
Figure 7.5. Liquefied gas electrolytes recycling concept and demonstration (A) Schematic of potential liquid-based electrolytes recycling process. (B) Practical process of liquefied gas solvent recycle. (C-D) Recycling of liquefied gas solvents in window cell (C) and custom coin cell (D).

7.4 Conclusion

We rationally designed liquefied gas electrolytes by combing liquefied solvents of the simplest ether with high solvating power and non-flammable low solvating hydrofluorocarbons. The liquefied gas electrolytes are not only non-flammable but also have a fire-extinguishing feature under abusive conditions. The formulated liquefied gas electrolyte maintained operations

in a wide temperature range (-78 to +80°C) and enabled stable Li-NMC cycling with high Li metal CE. A practical electrolyte recycling process was demonstrated by using the unique features of liquefied gas solvents. The electrochemical, safety and recycling properties of the liquefied gas electrolytes are derived directly from their physical and chemical properties. This study provides insights on designing all functional electrolytes and presents an encouraging path towards safer batteries with a wide temperature range and a feasible recycling process.

This chapter in full, is currently being prepared for submission for publication "Fire-extinguishing recyclable liquefied gas electrolytes for lithium metal batteries", Yin, Y.; Yang, Y.; Mayer, M.; Chen, Z.; Meng, Y. S. The dissertation author was the co-primary investigator and co-first author of the paper. The author formulated the electrolyte with Yin, Y., conceived the recycling process with Mayer and involved in all the experiment and characterization.

Chapter 8. Summary and Outlook

Lithium (Li) ion batteries have been successfully commercialized for three decades and made essential influence as energy conversion and storage device. As the applications have expanded from portable electronics to electric vehicles and grid storage, current LIBs can not meet the requirement on energy density, cycle life, capital cost, operation temperature range, and safety. With the development on advanced electrode, however, there have been little changes in electrolyte compositions since their commercialization and they have high melting point, high flammability, moderate oxidation stability, and poor compatibility with Li metal anode. The focus of my thesis was to invent and develop a new electrolyte system and improve the overall performance of Li metal batteries by regulating electrolyte and interfaces.

In Chapter 4, a completely new electrolyte system, liquefied gas electrolyte, was invented and demonstrated for energy storage devices. Different from the widely studied liquid electrolyte and solid-state electrolyte, liquefied gas electrolytes use molecules that are under gaseous state under ambient conditions. These molecules could be liquefied under moderate pressure to form a liquefied gas electrolyte for the first time. The selected molecules present superior physical and chemical properties, including low melting points, low viscosity, stable chemical bonding. Electrolytes using DFM and FM demonstrate excellent performance down to -60°C for electrochemical capacitor and 4-volt lithium-ion battery, respectively. This electrolyte also shows potential with Li metal anode. The rational designed new system largely expands the selection of possible solvents and opens a new pathway for overcoming a remaining challenge in the energy storage field.

In Chapter 5 and Chapter 6, comprehensive approaches have been applied to gain a deeper understanding of FM-based liquefied gas electrolytes and further improve the electrochemical performance. To address the issues of limited solubility, the additive amount of liquid cosolvents, THF and AN, have been introduced. Notably, with a high salt-to-cosolvent ratio (close to 1:1), a unique solvation structure is demonstrated by both MD simulation and Raman spectroscopy, in which 1) cosolvent is fully coordinated with Li^+, 2) FM is partially solvating with the Li^+ 3) salt is at aggregated state. With these configurations, a perfect balance has been realized: The limitations of oxidation or reduction stability for liquid cosolvent has been impaired by the full solvation. FM enables rapid transport and fast desolvation with high chemical stability. Aggregated salt, by using a practical concentration of salt, supports salt-derived stable interfaces. The high-temperature operation limitation has also been expanded by increasing the amount of salt and cosolvent. Combining these properties, modified liquefied gas electrolyte presents high ionic conductivity and transference number, leading to excellent performance with Li metal anode and high voltage cathode in a wide temperature range (-78 to 75°C). The solvation structure of electrolyte is the most significant aspect in electrolyte chemistry and the novel understanding of which will provide essential guidance for developing wide temperature, potential window batteries.

In Chapter 7, attentions are distributed to the safety and recycling of the electrolyte. We rationally formulated liquefied gas electrolytes by coupling liquefied solvents of the simplest ether with non-flammable low solvating hydrofluorocarbons. The liquefied gas electrolytes are not only non-flammable but also have a unique fire-extinguishing feature under abusive conditions. Using the vapor pressure-temperature relationship in the liquefied gas solvent, a practical electrolyte recycling process has been demonstrated. The system also maintains operations in a wide temperature range (-78 to +80°C) and enables stable Li-NMC cycling with high Li metal CE. The

electrochemical, safety, and recycling features of designed liquefied gas electrolytes are derived directly from their physical and chemical properties. This study provides clues on formulated all functional electrolytes and presents an encouraging path towards safer batteries with a wide temperature range and feasible recycling process.

Given the abovementioned work, there is definitely room and other possibilities for improvement and exploration. For future work, the first proposition is to further develop liquefied gas electrolyte by using different salt, cosolvent, and main solvent selections for better overall performance or specific applications. The current direction of using a stable low solvating solvent with aggregated salt is promising. Other directions are also worth exploring. The deeper understanding of the solvation structure and the interface formation mechanism is the key. Tests like Raman, transference number test only performed at room temperatures and new insights might be available at low/high temperatures. DFT calculation based on established solvation structure would be important on understand interface formation mechanism.

The second proposition is to enable anode-free Li metal batteries with high voltage cathode (i.e. LNMO). High Li metal CE has been demonstrated in liquefied gas electrolytes with relatively thick Li metal anode. For cells using thin Li metal (<50 µm) or even anode-free conditions, progress could be expected after proper hardware upgrade and chemistry optimization. In order to enable LNMO, oxidation stability of liquefied gas electrolytes needs to be further improved. The Al corrosion from LiTFSI could be one potential bottleneck, which might be solved by salt selection or solvation structure regulation.

The third proposition is to expand the applications beyond Li-ion chemistries. Rechargeable sodium (Na) batteries are considered as ideal alternatives to LIBs due to the high

abundance, low cost, and relatively good energy density. Knowledge and experience from Li batteries using liquefied gas electrolytes should be able to transfer to Na systems, such as solvation structure, SEI, potential window, and wide temperature operations. However, several differences between Na and Li systems should also be noted: 1) Na is more reactive and most inorganic SEI components (i.e. NaF, Na_2CO_3, Na_2O) of Na metal has high solubility and lower stability in solvents. 2) The lower desolvation energy of Na salt does not lead to better salt solubility because the desolvation of Na^+ to solvents is also weaker than Li^+-solvent bindings.

Finally, the commercialization of liquefied gas electrolyte is expected after the continuous improvement on cell device setup and chemistries. The knowledge and insights gained from liquefied gas electrolyte and interfaces should be also able to transfer to other electrolyte systems (i.e. liquid electrolyte, solid-state electrolyte, aqueous electrolyte, gel electrolyte) and promote the development of the battery industry.

References

1.   BPSTATS. BP Statistical Review of World Energy Statistical Review of World, 68th edition. *Ed. BP Stat. Rev. World Energy* 1–69 (2019).

2.   IEA. *Global CO2 emissions in 2019*. (2019).

3.   Albertus, P., Babinec, S., Litzelman, S. & Newman, A. Status and challenges in enabling the lithium metal electrode for high-energy and low-cost rechargeable batteries. *Nat. Energy* **3**, 16–21 (2018).

4.   Lin, D., Liu, Y. & Cui, Y. Reviving the lithium metal anode for high-energy batteries. *Nat. Nanotechnol.* **12**, 194–206 (2017).

5.   Goodenough, J. B. & Kim, Y. Challenges for rechargeable Li batteries. *Chem. Mater.* **22**, 587–603 (2010).

6.   Xu, B., Qian, D., Wang, Z. & Meng, Y. S. Recent progress in cathode materials research for advanced lithium ion batteries. *Mater. Sci. Eng. R Reports* **73**, 51–65 (2012).

7.   Xu, K. Nonaqueous liquid electrolytes for lithium-based rechargeable batteries. *Chem. Rev.* **104**, 4303–4417 (2004).

8.   Ozawa, K. Lithium-ion rechargeable batteries with LiCoO2 and carbon electrodes: the LiCoO2/C system. *Solid State Ionics* **69**, 212–221 (1994).

9.   Nagaura, T. *Proceedings of the 5th International Seminar on Lithium Battery Technology and Applications*. (1990).

10.   R. Fong, U. Von Sacken, J. R. D. Studies of Lithium Intercalation into Carbons Using Nonaqueous Electrochemical Cells. *J. Electrochem. Soc.* **137**, 2009 (1990).

11.   Ming, J. *et al.* New Insights on Graphite Anode Stability in Rechargeable Batteries: Li Ion Coordination Structures Prevail over Solid Electrolyte Interphases. *ACS Energy Lett.* **3**, 335–340 (2018).

12.   Peled, E. The Electrochemical Behavior of Alkali and Alkaline Earth Metals in Nonaqueous Battery Systems—The Solid Electrolyte Interphase Model. *J. Electrochem. Soc.* **126**, 2047 (1979).

13.   Gofer, Y., Ben-Zion, M. & Aurbach, D. Solutions of LiAsF6 in 1,3-dioxolane for secondary lithium batteries. *J. Power Sources* **39**, 163–178 (1992).

14.   Aurbach, D. The Surface Chemistry of Lithium Electrodes in Alkyl Carbonate Solutions. *J. Electrochem. Soc.* **141**, L1 (1994).

15.   Aurbach, D. Review of selected electrode-solution interactions which determine the performance of Li and Li ion batteries. *J. Power Sources* **89**, 206–218 (2000).

16. Cheng, X. B., Zhang, R., Zhao, C. Z. & Zhang, Q. Toward Safe Lithium Metal Anode in Rechargeable Batteries: A Review. *Chem. Rev.* **117**, 10403–10473 (2017).

17. Liu, J. *et al.* Pathways for practical high-energy long-cycling lithium metal batteries. *Nat. Energy* **4**, 180–186 (2019).

18. Choi, J. W. & Aurbach, D. Promise and reality of post-lithium-ion batteries with high energy densities. *Nature Reviews Materials* 1–16 (2016) doi:10.1038/natrevmats.2016.13.

19. Li, T., Zhang, X. Q., Shi, P. & Zhang, Q. Fluorinated Solid-Electrolyte Interphase in High-Voltage Lithium Metal Batteries. *Joule* **3**, 2647–2661 (2019).

20. Li, M., Wang, C., Chen, Z., Xu, K. & Lu, J. New Concepts in Electrolytes. *Chem. Rev.* (2020) doi:10.1021/acs.chemrev.9b00531.

21. Xu, L. *et al.* Interfaces in Solid-State Lithium Batteries. *Joule* **2**, 1991–2015 (2018).

22. Li, Y. *et al.* Atomic structure of sensitive battery materials and interfaces revealed by cryo–electron microscopy. *Science (80-.).* **358**, 506–510 (2017).

23. Niu, C. *et al.* Self-smoothing anode for achieving high-energy lithium metal batteries under realistic conditions. *Nat. Nanotechnol.* **14**, 594–601 (2019).

24. Han, X. *et al.* Negating interfacial impedance in garnet-based solid-state Li metal batteries. *Nat. Mater.* **16**, 572–579 (2017).

25. Lee, Y.-G. *et al.* High-energy long-cycling all-solid-state lithium metal batteries enabled by silver–carbon composite anodes. *Nat. Energy* 1–10 (2020) doi:10.1038/s41560-020-0575-z.

26. Yamada, Y., Wang, J., Ko, S., Watanabe, E. & Yamada, A. Advances and issues in developing salt-concentrated battery electrolytes. *Nat. Energy* **4**, 269–280 (2019).

27. Weber, R. *et al.* Long cycle life and dendrite-free lithium morphology in anode-free lithium pouch cells enabled by a dual-salt liquid electrolyte. *Nat. Energy* **4**, 683–689 (2019).

28. Fang, C. *et al.* Quantifying inactive lithium in lithium metal batteries. *Nature* **572**, 511–515 (2019).

29. Liu, Y. *et al.* An Artificial Solid Electrolyte Interphase with High Li-Ion Conductivity, Mechanical Strength, and Flexibility for Stable Lithium Metal Anodes. *Adv. Mater.* **29**, 1–8 (2017).

30. Miao, R. *et al.* Novel dual-salts electrolyte solution for dendrite-free lithium-metal based rechargeable batteries with high cycle reversibility. *J. Power Sources* **271**, 291–297 (2014).

31. Su, C.-C. *et al.* Solvating power series of electrolyte solvents for lithium batteries. *Energy Environ. Sci.* **12**, 1249–1254 (2019).

32. Ding, F. *et al.* Dendrite-free lithium deposition via self-healing electrostatic shield mechanism. *J. Am. Chem. Soc.* **135**, 4450–4456 (2013).

33. Markevich, E., Salitra, G. & Aurbach, D. Fluoroethylene Carbonate as an Important Component for the Formation of an Effective Solid Electrolyte Interphase on Anodes and Cathodes for Advanced Li-Ion Batteries. *ACS Energy Lett.* **2**, 1337–1345 (2017).

34. Borodin, O., Self, J., Persson, K. A., Wang, C. & Xu, K. Uncharted Waters: Super-Concentrated Electrolytes. *Joule* **4**, 69–100 (2020).

35. Suo, L. *et al.* 'Water-in-salt' electrolyte enables high-voltage aqueous lithium-ion chemistries. *Science (80-.).* **350**, 938–943 (2015).

36. Chen, S. *et al.* High-Efficiency Lithium Metal Batteries with Fire-Retardant Electrolytes. *Joule* **2**, 1548–1558 (2018).

37. Chen, S. *et al.* High-Voltage Lithium-Metal Batteries Enabled by Localized High-Concentration Electrolytes. *Adv. Mater.* **30**, 1–7 (2018).

38. Yang, Y. *et al.* High-Efficiency Lithium-Metal Anode Enabled by Liquefied Gas Electrolytes. *Joule* **3**, 1986–2000 (2019).

39. Rustomji, C. S. *et al.* Liquefied gas electrolytes for electrochemical energy storage devices. *Science (80-.).* **356**, (2017).

40. Louli, A. J., Ellis, L. D. & Dahn, J. R. Operando Pressure Measurements Reveal Solid Electrolyte Interphase Growth to Rank Li-Ion Cell Performance. *Joule* **3**, 745–761 (2019).

41. Wang, M. J., Choudhury, R. & Sakamoto, J. Characterizing the Li-Solid-Electrolyte Interface Dynamics as a Function of Stack Pressure and Current Density. *Joule* **3**, 2165–2178 (2019).

42. Yan, K. *et al.* Temperature-dependent Nucleation and Growth of Dendrite-Free Lithium Metal Anodes. *Angew. Chemie* **94025**, 11486–11490 (2019).

43. Wang, J. *et al.* Improving cyclability of Li metal batteries at elevated temperatures and its origin revealed by cryo-electron microscopy. *Nat. Energy* **4**, 664–670 (2019).

44. Chen, S. *et al.* Critical Parameters for Evaluating Coin Cells and Pouch Cells of Rechargeable Li-Metal Batteries. *Joule* **3**, 1094–1105 (2019).

45. Zachman, M. J., Tu, Z., Choudhury, S., Archer, L. A. & Kourkoutis, L. F. Cryo-STEM mapping of solid–liquid interfaces and dendrites in lithium-metal batteries. *Nature* **560**, 17–19 (2018).

46. Wang, X. *et al.* New Insights on the Structure of Electrochemically Deposited Lithium Metal and Its Solid Electrolyte Interphases via Cryogenic TEM. *Nano Lett.* **17**, 7606–7612 (2017).

47. Lee, J. Z. *et al.* Cryogenic Focused Ion Beam Characterization of Lithium Metal Anodes. *ACS Energy Lett.* **4**, 489–493 (2019).

48. Whittingham, M. S. Electrical energy storage and intercalation chemistry. *Science (80-.).* **192**, 1126–1127 (1976).

49. Mizushima K, Jones PC, Wiseman PJ, G. J. LixCoO2 (0< x<-1): A new cathode material for batteries of high energy density. *Mater. Res. Bull.* **15**, 783–789 (1980).

50. Dahn, J. R., Fuller, E. W., Obrovac, M. & von Sacken, U. Thermal stability of LixCoO2, LixNiO2 and λ-MnO2 and consequences for the safety of Li-ion cells. *Solid State Ionics* **69**, 265–270 (1994).

51. Amatucci, G. G. & Klein, J. M. J. M. T. C. Coo2, the end member of the li x coo2 solid solution. *J. Electrochem. Soc.* **143**, 1114–1123 (1996).

52. Van der Ven A, Aydinol MK, Ceder G, Kresse G, H. J. First-principles investigation of phase stability in Li x CoO. *Phys. Rev. B* **58**, 2975–2987 (1998).

53. Ohzuku, T. & Makimura, Y. Layered lithium insertion material of LiCo1/3Ni1/3Mn1/3O2 for lithium-ion batteries. *Chem. Lett.* 642–643 (2001) doi:10.1246/cl.2001.642.

54. Ohzuku, T. & Makimura, Y. Layered lithium insertion material of LiNi1/2Mn1/2O2 : A possible alternative to LiCoO2 for advanced lithium-ion batteries. *Chem. Lett.* **2**, 744–745 (2001).

55. Fong, R. Studies of Lithium Intercalation into Carbons Using Nonaqueous Electrochemical Cells. *J. Electrochem. Soc.* **137**, 2009 (1990).

56. Ding, F., Xu, W., Chen, X., Zhang, J., Engelhard, M.H., Zhang, Y., Johnson, B.R., Crum, J.V., Blake, T.A., Liu, X. and Zhang, J. G. Effects of carbonate solvents and lithium salts on morphology and coulombic efficiency of lithium electrode. *J. Electrochem. Soc.* **160**, A1894–A1901 (2013).

57. Wang, M. *et al.* Effect of LiFSI Concentrations to Form Thickness- and Modulus-Controlled SEI Layers on Lithium Metal Anodes. *J. Phys. Chem. C* **122**, 9825–9834 (2018).

58. Eshetu, G. G. *et al.* LiFSI vs. LiPF6 electrolytes in contact with lithiated graphite: Comparing thermal stabilities and identification of specific SEI-reinforcing additives. *Electrochim. Acta* **102**, 133–141 (2013).

59. Henderson, W. A. Concentrated electrolytes : decrypting electrolyte properties and reassessing Al corrosion mechanisms. *Energy Environ. Sci.* **7**, 416–426 (2014).

60. Yamada, Y. *et al.* Corrosion Prevention Mechanism of Aluminum Metal in Superconcentrated Electrolytes. *ChemElectroChem* **2**, 1687–1694 (2015).

61. Qian, J. *et al.* High rate and stable cycling of lithium metal anode. *Nat. Commun.* **6**, (2015).

62. Yamada, Y. *et al.* Unusual stability of acetonitrile-based superconcentrated electrolytes for fast-charging lithium-ion batteries. *J. Am. Chem. Soc.* **136**, 5039–5046 (2014).

63. Jiao, S. *et al.* Stable cycling of high-voltage lithium metal batteries in ether electrolytes. *Nat. Energy* **3**, 739–746 (2018).

64. Alvarado, J. *et al.* Bisalt ether electrolytes: A pathway towards lithium metal batteries with Ni-rich cathodes. *Energy Environ. Sci.* **12**, 780–794 (2019).

65. Chen, J. *et al.* Improving Electrochemical Stability and Low-Temperature Performance with Water/Acetonitrile Hybrid Electrolytes. *Adv. Energy Mater.* **10**, 1–10 (2020).

66. Okoshi, M., Chou, C. P. & Nakai, H. Theoretical Analysis of Carrier Ion Diffusion in Superconcentrated Electrolyte Solutions for Sodium-Ion Batteries. *J. Phys. Chem. B* **122**, 2600–2609 (2018).

67. Borodin, O. & Smith, G. D. Li+ transport mechanism in oligo(ethylene oxide)s compared to carbonates. *J. Solution Chem.* **36**, 803–813 (2007).

68. Self, J., Fong, K. D. & Persson, K. A. Transport in Superconcentrated LiPF6 and LiBF4/Propylene Carbonate Electrolytes. *ACS Energy Lett.* **4**, 2843–2849 (2019).

69. Alvarado, J. *et al.* A carbonate-free, sulfone-based electrolyte for high-voltage Li-ion batteries. *Mater. Today* **21**, 341–353 (2018).

70. Fan, X. *et al.* All-temperature batteries enabled by fluorinated electrolytes with non-polar solvents. *Nat. Energy* **4**, 882–890 (2019).

71. Ren, X. *et al.* Localized High-Concentration Sulfone Electrolytes for High-Efficiency Lithium-Metal Batteries. *Chem* **4**, 1877–1892 (2018).

72. Zheng, J. *et al.* Extremely Stable Sodium Metal Batteries Enabled by Localized High-Concentration Electrolytes. *ACS Energy Lett.* **3**, 315–321 (2018).

73. Chen, S. *et al.* High-Efficiency Lithium Metal Batteries with Fire-Retardant Electrolytes. *Joule* **2**, 2–8 (2018).

74. Fan, X. *et al.* Non-flammable electrolyte enables li-metal batteries with aggressive cathode chemistries. *Nat. Nanotechnol.* **13**, (2018).

75. Deng, T. *et al.* Designing In-Situ-Formed Interphases Enables Highly Reversible Cobalt-Free LiNiO2 Cathode for Li-ion and Li-metal Batteries. *Joule* **3**, 2550–2564 (2019).

76. Ueno, K. *et al.* Li+ Solvation and Ionic Transport in Lithium Solvate Ionic Liquids Diluted by Molecular Solvents. *J. Phys. Chem. C* **120**, 15792–15802 (2016).

77. Cao, X. *et al.* Monolithic solid–electrolyte interphases formed in fluorinated orthoformate-based electrolytes minimize Li depletion and pulverization. *Nat. Energy* **4**, 796–805 (2019).

78. Wang, C., Meng, Y. S. & Xu, K. Perspective—Fluorinating Interphases. *J. Electrochem. Soc.* **166**, A5184–A5186 (2019).

79. Zheng, Q. *et al.* A cyclic phosphate-based battery electrolyte for high voltage and safe operation. *Nat. Energy* (2020) doi:10.1038/s41560-020-0567-z.

80. Tan, D. H. S., Banerjee, A., Chen, Z. & Meng, Y. S. From nanoscale interface characterization to sustainable energy storage using all-solid-state batteries. *Nat. Nanotechnol.* **15**, 170–180 (2020).

81. Han, F. *et al.* High electronic conductivity as the origin of lithium dendrite formation within

solid electrolytes. *Nat. Energy* **4**, 187–196 (2019).

82. Yao, P. *et al.* Review on Polymer-Based Composite Electrolytes for Lithium Batteries. *Front. Chem.* **7**, 1–17 (2019).

83. Zhang, H. *et al.* Single lithium-ion conducting solid polymer electrolytes: Advances and perspectives. *Chem. Soc. Rev.* **46**, 797–815 (2017).

84. Mindemark, J., Lacey, M. J., Bowden, T. & Brandell, D. Beyond PEO—Alternative host materials for Li+-conducting solid polymer electrolytes. *Prog. Polym. Sci.* **81**, 114–143 (2018).

85. Tan, D. H. S. *et al.* Enabling Thin and Flexible Solid-State Composite Electrolytes by the Scalable Solution Process. *ACS Appl. Energy Mater.* **2**, 6542–6550 (2019).

86. Randau, S. *et al.* Benchmarking the performance of all-solid-state lithium batteries. *Nat. Energy* **5**, 259–270 (2020).

87. Zhao, Q., Stalin, S., Zhao, C. Z. & Archer, L. A. Designing solid-state electrolytes for safe, energy-dense batteries. *Nat. Rev. Mater.* **5**, 229–252 (2020).

88. Yang, Y. *et al.* Liquefied Gas Electrolytes for Wide-Temperature Lithium Metal Batteries. *Energy Environ. Sci.* **10.1039/D0**, (2020).

89. Linden, D. & McDonald, B. The lithium-sulfur dioxide primary battery - its characteristics, performance and applications. *J. Power Sources* **5**, 35–55 (1980).

90. West, W.C., Shevade, A., Soler, J., Kulleck, J., Smart, M.C., Ratnakumar, B.V., Moran, M., Haiges, R., Christe, K.O. and Prakash, G. S. Sulfuryl and thionyl halide-based ultralow temperature primary batteries. *J. Electrochem. Soc.* **157**, A571–A577 (2010).

91. Uribe, F.A., Semkow, K.W. and Sammells, A. F. Cells containing solvated electron lithium negative electrodes. *J. Electrochem. Soc.* **136**, 3559–3565 (1989).

92. Bernard, L. *et al.* Applications of metal-ammonia solutions to secondary batteries. *J. Phys. Chem.* **88**, 3833–3837 (1984).

93. Zurek, E., Edwards, P. P. & Hoffmann, R. A molecular perspective on lithium-ammonia solutions. *Angew. Chemie - Int. Ed.* **48**, 8198–8232 (2009).

94. Abbott, A. P. & Eardley, C. A. Conductivity of (C4H9)4N BF4 in liquid and supercritical hydrofluorocarbons. *J. Phys. Chem. B* **104**, 9351–9355 (2000).

95. Abbott, A. P., Eardley, C. A., Harper, J. C. & Hope, E. G. Electrochemical investigations in liquid and supercritical 1,1,1,2-tetrafluoroethane (HFC 134a) and difluoromethane (HFC 32). *J. Electroanal. Chem.* **457**, 1–4 (1998).

96. Abbott, A. P. & Eardley, C. A. Electrochemical Reduction of CO2 in a Mixed Supercritical Fluid. *J. Phys. Chem. B* **104**, 775–779 (2000).

97. Olsen, S. A. & Tallman, D. E. Conductivity and voltammetry in liquid and supercritical

halogenated solvents. *Anal. Chem.* **68**, 2054–2061 (1996).

98. Olsen, S. A. & Tallman, D. E. Voltammetry of Ferrocene in Subcritical and Supercritical Chlorodifluoromethane. *Anal. Chem.* **66**, 503–509 (1994).

99. Goldfarb, D. L. & Corti, H. R. Electrical Conductivity of Decamethylferrocenium Hexafluorophosphate and Tetrabutylammonium Hexafluorophosphate in Supercritical Trifluoromethane. *J. Phys. Chem. B* **108**, 3358–3367 (2004).

100. Goldfarb, D. L. & Corti, H. R. Electrochemistry in supercritical trifluoromethane. *Electrochem. commun.* **2**, 663–670 (2000).

101. Ue, M. Electrochemical Properties of Organic Liquid Electrolytes Based on Quaternary Onium Salts for Electrical Double-Layer Capacitors. *J. Electrochem. Soc.* **141**, 2989 (1994).

102. Chmiola, J. *et al.* Anomalous increase in carbon at pore sizes less than 1 nanometer. *Science (80-.).* **313**, 1760–1763 (2006).

103. E. Lemmon, M. McLinden, D. F. Thermophysical properties of fluid systems. *NIST Chem. Webb.* **NIST Stand**, (2005).

104. Mathias, J. R., Martin, J. L. & Burns, T. W. The electrical conductivity of solutions in methyl alcohol in the neighborhood of their critical points. II. *Phys. Rev. Ser.* **18**, 89–103 (1904).

105. Barão, M. T., Nieto De Castro, C. A. & Mardolcar, U. V. Molecular properties of alternative refrigerants derived from dielectric-constant measurements. *Int. J. Thermophys.* **18**, 419–438 (1997).

106. A. Clifford, T. C. *Fundamentals of Supercritical Fluids*. (1999).

107. Abbott, A. P., Eardley, C. A. & Tooth, R. Relative permittivity measurements of 1,1,1,2-tetrafluoroethane (HFC 134a), pentafluoroethane (HFC 125), and difluoromethane (HFC 32). *J. Chem. Eng. Data* **44**, 112–115 (1999).

108. Brandon, E. J., West, W. C., Smart, M. C., Whitcanack, L. D. & Plett, G. A. Extending the low temperature operational limit of double-layer capacitors. *J. Power Sources* **170**, 225–232 (2007).

109. Staley, R. H. & Beauchamp, J. L. Intrinsic Acid-Base Properties of Molecules. Binding Energies of Li+ to π- and n-Donor Bases. *J. Am. Chem. Soc.* **97**, 5920–5921 (1975).

110. Smart, M. C., Ratnakumar, B. V. & Surampudi, S. Use of Organic Esters as Cosolvents in Electrolytes for Lithium-Ion Batteries with Improved Low Temperature Performance. *J. Electrochem. Soc.* **149**, A361 (2002).

111. Jänes, A. & Lust, E. Use of organic esters as co-solvents for electrical double layer capacitors with low temperature performance. *J. Electroanal. Chem.* **588**, 285–295 (2006).

112. Kötz, R., Ruch, P. W. & Cericola, D. Aging and failure mode of electrochemical double layer capacitors during accelerated constant load tests. *J. Power Sources* **195**, 923–928

(2010).

113. Al., D. A. et. The Correlation Between the Surface Chemistry and the Performance of Li-Carbon Intercalation Anodes for Rechargeable 'Rocking-Chair'Type Batteries. *J. Electrochem. Soc.* **141**, 603–611 (1994).

114. Anouti, M., Dougassa, Y. R., Tessier, C., El Ouatani, L. & Jacquemin, J. Low pressure carbon dioxide solubility in pure electrolyte solvents for lithium-ion batteries as a function of temperature. Measurement and prediction. *J. Chem. Thermodyn.* **50**, 71–79 (2012).

115. Di Nicola, G., Polonara, F., Ricci, R. & Stryjek, R. PVTx measurements for the R116 + CO2 and R41 + CO2 systems. New isochoric apparatus. *J. Chem. Eng. Data* **50**, 312–318 (2005).

116. Desilvestro, J. & Pons, S. The cathodic reduction of carbon dioxide in acetonitrile. An electrochemical and infrared spectroelectrochemical study. *J. Electroanal. Chem.* **267**, 207–220 (1989).

117. D. Aurbach, E. Zinigrad, Y. Cohen, H. T. A short review of failure mechanisms of lithium metal and lithiated graphite anodes in liquid electrolyte solutions. *Solid state ionics* **148**, 405–416 (2002).

118. Park, M. S. *et al.* A highly reversible lithium metal anode. *Sci. Rep.* **4**, 1–8 (2014).

119. Hirai, T. Influence of Electrolyte on Lithium Cycling Efficiency with Pressurized Electrode Stack. *J. Electrochem. Soc.* **141**, 611 (1994).

120. Lu, Y., Tu, Z. & Archer, L. A. Stable lithium electrodeposition in liquid and nanoporous solid electrolytes. *Nat. Mater.* **13**, 961–969 (2014).

121. V. R. Koch, J. L. Goldman, C. J. Mattos, M. M. Specular lithium deposits from lithium hexafluoroarsenate/diethyl ether electrolytes. *J. Electrochem. Soc.* **129**, 1–4 (1982).

122. C. Desjardins, T. Cadger, R. Salter, G. Donaldson, E. C. Lithium cycling performance in improved lithium hexafluoroarsenate/2-methyl tetrahydrofuran electrolytes. *J. Electrochem. Soc.* **132**, 529–533 (1985).

123. Osaka, T. Enhancement of Lithium Anode Cyclability in Propylene Carbonate Electrolyte by CO[sub 2] Addition and Its Protective Effect Against H[sub 2]O Impurity. *J. Electrochem. Soc.* **142**, 1057 (1995).

124. Qian, J. *et al.* Anode-Free Rechargeable Lithium Metal Batteries. *Adv. Funct. Mater.* **26**, 7094–7102 (2016).

125. M. Smart, B. Ratnakumar, K. Chin, L. W. Lithium-ion electrolytes containing ester cosolvents for improved low temperature performance. *J. Electrochem. Soc.* **157**, A1361–A1374 (2010).

126. Zhang, S. S., Xu, K. & Jow, T. R. Low-temperature performance of Li-ion cells with a LiBF4-based electrolyte. *J. Solid State Electrochem.* **7**, 147–151 (2003).

127. Ratnakumar, B. V., Smart, M. C. & Surampudi, S. Effects of SEI on the kinetics of lithium intercalation. *J. Power Sources* **97**–**98**, 137–139 (2001).

128. Zhang, S. S., Xu, K. & Jow, T. R. Electrochemical impedance study on the low temperature of Li-ion batteries. *Electrochim. Acta* **49**, 1057–1061 (2004).

129. K. Kanamura, S. Shiraishi, Z. i. T. Electrochemical deposition of very smooth lithium using nonaqueous electrolytes containing HF. *J. Electrochem. Soc.* **143**, 2187–2197 (1996).

130. Al., M. C. S. et. Wide operating temperature range electrolytes for high voltage and high specific energy Li-ion cells. *ECS Trans* **50**, 355–364 (2013).

131. Edström, K., Gustafsson, T. & Thomas, J. O. The cathode-electrolyte interface in the Li-ion battery. *Electrochim. Acta* **50**, 397–403 (2004).

132. Dahéron, L. *et al.* Electron transfer mechanisms upon lithium deintercalation from LiCoO 2 to CoO2 investigated by XPS. *Chem. Mater.* **20**, 583–590 (2008).

133. Whittingham, M. S. Chemistry, Electrical energy storage and intercalation. *Science (80-.).* **192**, 1126–1127 (1976).

134. PbSO, P., Koh, N., -, -e, Li Si, V. & LiX, S. Building better batteries. *Nature* **451**, 652–657 (2008).

135. Chu, S. & Majumdar, A. Opportunities and challenges for a sustainable energy future. *Nature* **488**, 294–303 (2012).

136. Xu, W. *et al.* Lithium metal anodes for rechargeable batteries. *Energy Environ. Sci.* **7**, 513–537 (2014).

137. Fan, X. *et al.* Highly Fluorinated Interphases Enable High-Voltage Li-Metal Batteries. *Chem* **4**, 174–185 (2018).

138. Borodin, O. Polarizable force field development and molecular dynamics simulations of ionic liquids. *J. Phys. Chem. B* **113**, 11463–11478 (2009).

139. Borodin, O. *et al.* Insights into the Structure and Transport of the Lithium, Sodium, Magnesium, and Zinc Bis(trifluoromethansulfonyl)imide Salts in Ionic Liquids. *J. Phys. Chem. C* **122**, 20108–20121 (2018).

140. Wang, J. *et al.* Superconcentrated electrolytes for a high-voltage lithium-ion battery. *Nat. Commun.* **7**, 1–9 (2016).

141. Dong, X., Guo, Z., Guo, Z., Wang, Y. & Xia, Y. Organic Batteries Operated at −70°C. *Joule* **2**, 902–913 (2018).

142. Zhang, S. S., Xu, K. & Jow, T. R. Low temperature performance of graphite electrode in Li-ion cells. *Electrochim. Acta* **48**, 241–246 (2002).

143. Aurbach, D. *et al.* On the Surface Chemical Aspects of Very High Energy Density, Rechargeable Li–Sulfur Batteries. *J. Electrochem. Soc.* **156**, A694 (2009).

144. Zhang, Q. *et al.* Synergetic Effects of Inorganic Components in Solid Electrolyte Interphase on High Cycle Efficiency of Lithium Ion Batteries. *Nano Lett.* **16**, 2011–2016 (2016).

145. Gunceler, D., Letchworth-Weaver, K., Sundararaman, R., Schwarz, K. A. & Arias, T. A. The importance of nonlinear fluid response in joint density-functional theory studies of battery systems. *Model. Simul. Mater. Sci. Eng.* **21**, (2013).

146. Xu, K. Electrolytes and Interphases in Li-Ion Batteries and Beyond. *Chem. Rev.* **114**, 11503–11618 (2014).

147. Hu, Z. *et al.* Nonflammable Nitrile Deep Eutectic Electrolyte Enables High-Voltage Lithium Metal Batteries. *ACS Appl. Mater. Interfaces* (2020) doi:10.1021/acs.chemmater.9b05003.

148. Cho, Y. G., Kim, Y. S., Sung, D. G., Seo, M. S. & Song, H. K. Nitrile-assistant eutectic electrolytes for cryogenic operation of lithium ion batteries at fast charges and discharges. *Energy Environ. Sci.* **7**, 1737–1743 (2014).

149. Zhang, X. Q. *et al.* Regulating Anions in the Solvation Sheath of Lithium Ions for Stable Lithium Metal Batteries. *ACS Energy Lett.* **4**, 411–416 (2019).

150. Zheng, Y. *et al.* Localized high concentration electrolyte behavior near a lithium-metal anode surface. *J. Mater. Chem. A* **7**, 25047–25055 (2019).

151. Wang, Z. *et al.* An Anion-Tuned Solid Electrolyte Interphase with Fast Ion Transfer Kinetics for Stable Lithium Anodes. *Adv. Energy Mater.* **10**, 1–9 (2020).

152. Wohde, F., Balabajew, M. & Roling, B. Li + Transference Numbers in Liquid Electrolytes Obtained by Very-Low-Frequency Impedance Spectroscopy at Variable Electrode Distances. *J. Electrochem. Soc.* **163**, A714–A721 (2016).

153. Dong, X. *et al.* High-Energy Rechargeable Metallic Lithium Battery at −70 °C Enabled by a Cosolvent Electrolyte. *Angew. Chemie* **131**, 5679–5683 (2019).

154. Seo, D. M. *et al.* Solvate structures and spectroscopic characterization of litfsi electrolytes. *J. Phys. Chem. B* **118**, 13601–13608 (2014).

155. Zugmann, S. *et al.* Electrochimica Acta Measurement of transference numbers for lithium ion electrolytes via four different methods , a comparative study. *Electrochim. Acta* **56**, 3926–3933 (2011).

156. Borodin, O. *et al.* Modeling Insight into Battery Electrolyte Electrochemical Stability and Interfacial Structure. *Acc. Chem. Res.* **50**, 2886–2894 (2017).

157. Chen, J. *et al.* Electrolyte design for Li metal-free Li batteries. *Mater. Today* (2020) doi:10.1016/j.mattod.2020.04.004.

158. Effat, M. B. *et al.* Towards succinonitrile-based lithium metal batteries with long cycle life: The influence of fluoroethylene carbonate loading and the separator. *J. Power Sources* **436**, 226802 (2019).

159.   Zeng, Z. *et al.* Safer lithium ion batteries based on nonflammable electrolyte. *J. Power Sources* **279**, 6–12 (2015).

160.   Wu, L. *et al.* A new phosphate-based nonflammable electrolyte solvent for Li-ion batteries. *J. Power Sources* **188**, 570–573 (2009).

161.   Shiga, T., Kato, Y., Kondo, H. & Okuda, C. A. Self-extinguishing electrolytes using fluorinated alkyl phosphates for lithium batteries. *J. Mater. Chem. A* **5**, 5156–5162 (2017).

162.   Wang, J. *et al.* Fire-extinguishing organic electrolytes for safe batteries. *Nat. Energy* **3**, 22–29 (2018).

163.   Cao, X. *et al.* Nonflammable Electrolytes for Lithium Ion Batteries Enabled by Ultraconformal Passivation Interphases. *ACS Energy Lett.* **4**, 2529–2534 (2019).

164.   Niu, C. *et al.* High-energy lithium metal pouch cells with limited anode swelling and long stable cycles. *Nat. Energy* (2019) doi:10.1038/s41560-019-0390-6.